UNCLASSIFIED

AD NUMBER

ADB247757

NEW LIMITATION CHANGE

TO

Approved for public release, distribution unlimited

FROM

Distribution authorized to U.S. Gov't. agencies only; Proprietary Info; Sep 98 Other requests shall be referred to U.S. Army Medical Research and Materiel Command, 504 Scott Street, Ft Detrick, MD 21702-5012

AUTHORITY

U.S. Army Medical Research and Materiel Command and Fort Detrick ltr., dtd October 17, 2001.

THIS PAGE IS UNCLASSIFIED

AD_____

CONTRACT NUMBER DAMD17-96-C-6061

TITLE: 3-D Ultrasound Vascularity Assessment for Breast Cancer Diagnosis

PRINCIPAL INVESTIGATOR: Paul L. Carson, Ph.D.

CONTRACTING ORGANIZATION: University of Michigan
Ann Arbor, Michigan 48109-1274

REPORT DATE: September 1998

TYPE OF REPORT: Annual

PREPARED FOR: Commander
U.S. Army Medical Research and Materiel Command
Fort Detrick, Frederick, Maryland 21702-5012

DISTRIBUTION STATEMENT: Distribution authorized to U.S. Government agencies only (proprietary information, Sep 98). Other requests for this document shall be referred to U.S. Army Medical Research and Materiel Command, 504 Scott Street, Fort Detrick, Maryland 21702-5012.

The views, opinions and/or findings contained in this report are those of the author(s) and should not be construed as an official Department of the Army position, policy or decision unless so designated by other documentation.

19990929 050

DTIC QUALITY INSPECTED 4

NOTICE

USING GOVERNMENT DRAWINGS, SPECIFICATIONS, OR OTHER DATA INCLUDED IN THIS DOCUMENT FOR ANY PURPOSE OTHER THAN GOVERNMENT PROCUREMENT DOES NOT IN ANY WAY OBLIGATE THE U.S. GOVERNMENT. THE FACT THAT THE GOVERNMENT FORMULATED OR SUPPLIED THE DRAWINGS, SPECIFICATIONS, OR OTHER DATA DOES NOT LICENSE THE HOLDER OR ANY OTHER PERSON OR CORPORATION; OR CONVEY ANY RIGHTS OR PERMISSION TO MANUFACTURE, USE, OR SELL ANY PATENTED INVENTION THAT MAY RELATE TO THEM.

LIMITED RIGHTS LEGEND

Award Number: DAMD17-96-C-6061
Organization: University of Michigan
Location of Limited Rights Data (Pages):

Those portions of the technical data contained in this report marked as limited rights data shall not, without the written permission of the above contractor, be (a) released or disclosed outside the government, (b) used by the Government for manufacture or, in the case of computer software documentation, for preparing the same or similar computer software, or (c) used by a party other than the Government, except that the Government may release or disclose technical data to persons outside the Government, or permit the use of technical data by such persons, if (i) such release, disclosure, or use is necessary for emergency repair or overhaul or (ii) is a release or disclosure of technical data (other than detailed manufacturing or process data) to, or use of such data by, a foreign government that is in the interest of the Government and is required for evaluational or informational purposes, provided in either case that such release, disclosure or use is made subject to a prohibition that the person to whom the data is released or disclosed may not further use, release or disclose such data, and the contractor or subcontractor or subcontractor asserting the restriction is notified of such release, disclosure or use. This legend, together with the indications of the portions of this data which are subject to such limitations, shall be included on any reproduction hereof which includes any part of the portions subject to such limitations.

THIS TECHNICAL REPORT HAS BEEN REVIEWED AND IS APPROVED FOR PUBLICATION.

_____ Krishna Claron Mihra
9/10/99

_____ _____

REPORT DOCUMENTATION PAGE

Form Approved
OMB No. 0704-0188

Public reporting burden for this collection of information is estimated to average 1 hour per response, including the time for reviewing instructions, searching existing data sources, gathering and maintaining the data needed, and completing and reviewing the collection of information. Send comments regarding this burden estimate or any other aspect of this collection of information, including suggestions for reducing this burden, to Washington Headquarters Services, Directorate for Information Operations and Reports, 1215 Jefferson Davis Highway, Suite 1204, Arlington, VA 22202-4302, and to the Office of Management and Budget, Paperwork Reduction Project (0704-0188), Washington, DC 20503.

1. AGENCY USE ONLY *(Leave blank)*	2. REPORT DATE	3. REPORT TYPE AND DATES COVERED
	September 1998	Annual (1 Sep 97 - 31 Aug 98)

4. TITLE AND SUBTITLE
3-D Ultrasound Vascularity Assessment for Breast Cancer Diagnosis

5. FUNDING NUMBERS
DAMD17-96-C-6061

6. AUTHOR(S)
Paul L. Carson, Ph.D.

7. PERFORMING ORGANIZATION NAME(S) AND ADDRESS(ES)
University of Michigan
Ann Arbor, Michigan 48109-1274

8. PERFORMING ORGANIZATION REPORT NUMBER

9. SPONSORING/MONITORING AGENCY NAME(S) AND ADDRESS(ES)
Commander
U.S. Army Medical Research and Materiel Command
Fort Detrick, Frederick, Maryland 21702-5012

10. SPONSORING/MONITORING AGENCY REPORT NUMBER

11. SUPPLEMENTARY NOTES

12a. DISTRIBUTION / AVAILABILITY STATEMENT
Distribution authorized to U.S. Government agencies only (proprietary information, Sep 98). Other requests for this document shall be referred to U.S. Army Medical Research and Materiel Command, 504 Scott Street, Fort Detrick, Maryland 21702-5012.

12b. DISTRIBUTION CODE

13. ABSTRACT *(Maximum 200*

This project is to improve the diagnosis and management of patients with breast cancer through development and evaluation of 3D ultrasound imaging and quantification techniques emphasizing vascularity. Progress this second year included advances which should increase the sensitivity and specificity of ultrasound imaging in discriminating benign from malignant known masses. Preliminary data analyses were completed on new trials and contributions were made to advance 3D image acquisition, display and quantification. The registration achieved so far in compound and sequential imaging is unexpectedly good and robust. It has promise for an increasing number of applications that could revolutionize the use of ultrasound in medicine, particularly for serial studies. Our new extended 3D field of view imaging appears to greatly increase the changes of achieving these goals. The results to date in image-based slice positioning continue to be impressive, and at least two companies have implemented aspects of the technique, one with clear acknowledgement of our developments. 3D detection and display of lactic ducts has been illustrated in concept, but much more work will be required to show practical, routine utility.

14. SUBJECT TERMS	15. NUMBER OF PAGES
Breast Cancer	80
	16. PRICE CODE

17. SECURITY CLASSIFICATION OF REPORT	18. SECURITY CLASSIFICATION OF THIS PAGE	19. SECURITY CLASSIFICATION OF ABSTRACT	20. LIMITATION OF ABSTRACT
Unclassified	Unclassified	Unclassified	Limited

FOREWORD

Opinions, interpretations, conclusions and recommendations are those of the author and are not necessarily endorsed by the U.S. Army.

\ Where copyrighted material is quoted, permission has been obtained to use such material.

\ Where material from documents designated for limited distribution is quoted, permission has been obtained to use the material.

\ Citations of commercial organizations and trade names in this report do not constitute an official Department of Army endorsement or approval of the products or services of these organizations.

____ In conducting research using animals, the investigator(s) adhered to the "Guide for the Care and Use of Laboratory Animals," prepared by the Committee on Care and use of Laboratory Animals of the Institute of Laboratory Resources, national Research Council (NIH Publication No. 86-23, Revised 1985).

\ For the protection of human subjects, the investigator(s) adhered to policies of applicable Federal Law 45 CFR 46.

____ In conducting research utilizing recombinant DNA technology, the investigator(s) adhered to current guidelines promulgated by the National Institutes of Health.

____ In the conduct of research utilizing recombinant DNA, the investigator(s) adhered to the NIH Guidelines for Research Involving Recombinant DNA Molecules.

____ In the conduct of research involving hazardous organisms, the investigator(s) adhered to the CDC-NIH Guide for Biosafety in Microbiological and Biomedical Laboratories.

Paul L. Sarran 9/8/99

PI - Signature Date

I. TABLE OF CONTENTS

I. TABLE OF CONTENTS....4

II. INTRODUCTION....4

III. BODY....5

A. Clinical Trials and Vascularity Measures....5
1. Report on Validation/improvement of vascularity measures (Deliverable Item 3.)....5
2. Summary Report on Clinical Trials (Deliverable Item 1.)....5
3. Trials data analysis and write-up....5

B. Interim Report on Image Processing for Auto-registration in Compound and Sequential Imaging....5
1. Develop automated image registration by mutual information....5
2. Process ultrasound images to evaluate/demonstrate compound and sequential imaging therewith....5

C. Real Time Image-based Registration of Slice Position [IBaR]....6
1. Real time speckle decorrelation for image plane positioning....6

D. Digital ductography development....6
1. Ductographic analysis of selected clinical trial cases....6

E. Figures....6

IV. CONCLUSIONS....7

Clinical Trials....7

Compound and Sequential Imaging....7

Image-based Slice Positioning [IBaR]....7

Digital ductography development....7

V. REFERENCES....7

VI. APPENDICES....8

1. Automated 3-D US Frame Positioning Computed from Elevational Speckle Decorrelation, Radiology, 209, 575-582, 1998.
2. Extended Field of View, and Sequential Ultrasound Imaging, submitted to RSNA EJ.
3. Semiautomatic Registration of Volumetric Ultrasound Scans, Ultras. In Med. & Biol., in press.
4. Normalizing Fractional Moving Blood Volume Estimates with Power Doppler US: Defining a Stable Intravascular Point with the Cumulative Power Distribution Function, Radiology, 205, 757-765, 1997.

5. 3D Doppler Image Signal Quantification of Breast Masses, Ultrasound Med. Biol., 24:6, 945-952, 1998.

6. Future Directions in Diagnostic Ultrasound, Radiology, 209, 305-311, 1997 (review only, no acknowledgement).

7. A hand-controlled, 3-D ultrasound guide and measurement system, in Acoustical Imaging, S. Lees, ed., Plenum Press, N.Y., 1997, ISBN 0306457687 TC, v. 23, 237-242.

8. Utility of 3D ultrasound in the discrimination and detection of breast cancer , submitted to RSNA EJ.

II. INTRODUCTION

The research to be conducted over the four year period of this contract centers around three areas 1) expansion of clinical trials capabilities performed under an ongoing NIH grant and their continuation after those trials are completed; 2) image registration using the mutual information cost function for evaluation/demonstration of image compounding and sequential examinations; 3) approaches to real time image-based slice positioning; 4) the, as yet, unique effort to image lactic ducts in 3D and perform preliminary evaluation of their diagnostic potential. Most of the research will be performed in parallel by various investigators. The following time line for the second and third years was given in the funded scope of work.

Table 1. Time Line for Present and Next Project Periods	Year 2	Year 3
Clinical Trials		
Validation/improvement of vascularity measures	+ +	
Clinical Trials of ~30 subjects	+ +	- + - +
Trials data analysis and write-up		
Compound and Sequential Imaging		
Develop automated image registration by mutual information	+ - + -	+ - + -
Process ultrasound images to evaluate/demonstrate compound and sequential* imaging therewith	+	
Image-based Slice Positioning [IBaR]		
Real time speckle decorrelation for image plane positioning	- - - -	- +
Digital ductography development	+ +	+ +
Ductographic analysis of selected clinical trial cases		+ +

*Auto registration of breast images from multiple exams + = concentrated effort - = modest effort

The following series of deliverables and associated materials are included in this annual progress report. Included are a listing of papers, abstracts and manuscripts, published and submitted.

Year 02

Item 1: Summary report of clinical trials conducted in the second year.
Item 2: Interim report on image processing for auto-registration in compound imaging.
Item 3: Report on improvement and validation of vascularity measures.

III. BODY

Progress has been made in the four areas of emphasis of this grant as listed below.

A. Clinical Trials and Vascularity Measures

1. Report on Validation/improvement of vascularity measures (Deliverable Item 3.)

Several advances have been made in validation/improvement of vascularity measures. We implemented the automated measurement technique for normalizing power mode blood signal measures in 3D data sets (Reference/Appendix ##3) and have applied it to available patient data with promising results. (Deliverable Item 3.)

2. Summary Report on Clinical Trials (Deliverable Item 1.)

Because of demands for the patients by other grants and technique startup, we have done only six patients using the latest apparatus including the 1.5 D matrix array scanhead. However some of the competing grants are winding down and the rate will accelerate dramatically in the second half of year 3 and be continued into year 4. This delay is more than offset by accomplishments ahead of schedule in sequential imaging and image-based slice positioning.

3. Trials data analysis and write-up

Analysis of quantitative vascularity results from previous trials was conducted in part under this grant, resulting in a second publication, Reference/Appendix 5. This contract also contributed modestly to a submission on clinical trials methods and preliminary results, Reference/Appendix 8.

B. Interim Report on Image Processing for Auto-registration in Compound and Sequential Imaging

The most exciting advances with the greatest long term significance again involve the automatic registration of two or more 3D image sets to add to the information and quality of the resulting set or to demonstrate changes between two sets. (Deliverable Item 2.)

1. Develop automated image registration by mutual information

The software developed here, MIAMI Fuse, has been further refined and employed now by a variety of users. The first demonstrated 3D coregistrations of ultrasound image sets are reported in Reference/Appendix 3.

2. Process ultrasound images to evaluate/demonstrate compound and sequential imaging therewith

The software has been modified and the registration is now being applied routinely on patient examples for demonstration of each of several uses, including: 1) tracking changes for patients undergoing chemotherapy and antiangiogenesis therapy; 2) highlighting and quantifying changes in normal or suspicious breasts as a prelude to improved detection of preclinical disease; 3) combining 3D data sets from various ultrasound imaging modes to properly register the unique information provided by each; 4) demonstrating tissue mechanical properties by their motion during manipulation; 5) expanding the field of view by combining several partially-overlapping 3D scans to see the full volume of medium to large lesions and reasonable amounts of surrounding vascular morphology and to show a reasonable volume of the breast for tracking difficult areas of the breast in follow-up studies; 6) combining views from multiple angles (compounding). Use types 1) and 3) are illustrated in Fig. 1 and use 5) is illustrated in Fig. 2. All but the compounding examples are outstanding, leading to a new approach to following the high risk or difficult cases. Compounding examples are promising, but considerably more work is needed. Compounding is the subject of our longer term efforts through the planned thesis of one of our promising Ph.D. candidates. Several examples illustrating these concepts are in a submitted electronic journal manuscript (Reference/Appendix 2) available confidentially for reviewers of this report on the web at http://deepred.rad.med.umich.edu/previews/index.html. Use as an ID – "Reviewer" and the password – "3DBreast". This was part of a manuscript submitted in year 02 and now split into two parts in year 03.

C. Real Time Image-based Registration of Slice Position [IBaR]

1. Real time speckle decorrelation for image plane positioning

Considerable progress has been made in IBaR and real time implementation thereof. See, for example Fig. 8 in Reference/Appendix 1 for evidence of successful image-based scan separation registration in actual breast images. With our direct help, one company has implemented portions of this technique in real time. This progress will be reported more fully in the year 03 summary report.

D. Digital ductography development

1. Ductographic analysis of selected clinical trial cases

Results of part of this work were reported at two meetings in late 1997 (9,10). The many other abstracts of presentations related to this grant are not listed, as they are generally covered by the manuscripts included.

E. Figures

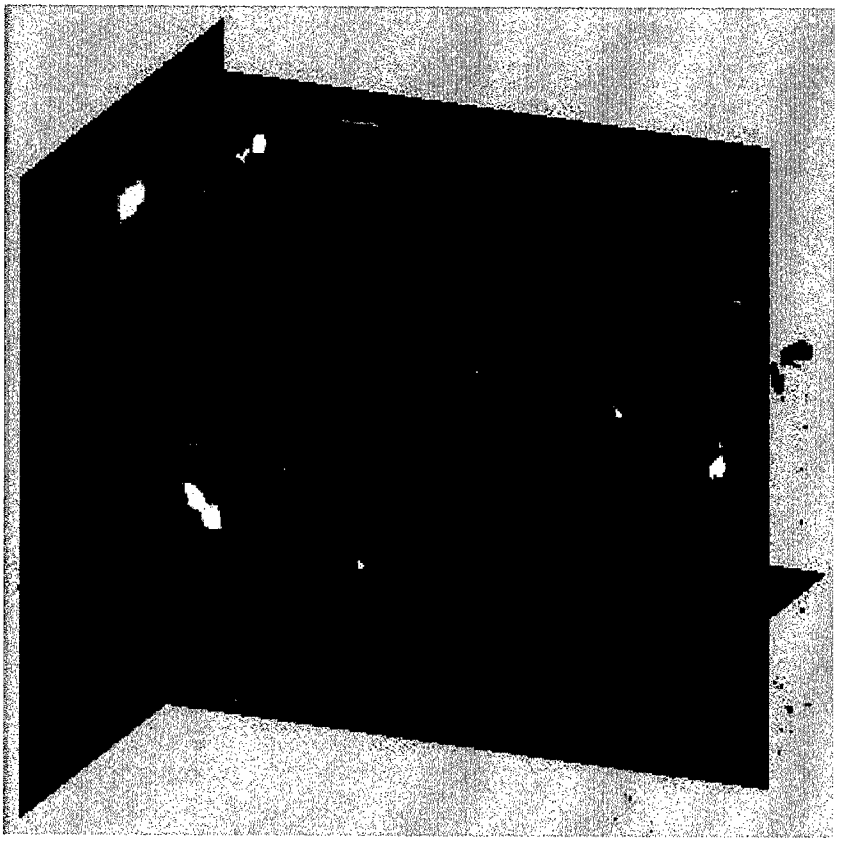

Fig. 1 Coregistered and superimposed power mode images of two sequential scans, obtained 4 weeks apart in a patient undergoing chemotherapy. The left half of the gray scale background is taken from the first scan, the right half from the second scan. The surface-rendered vascularity in the first and second scans are displayed throughout the volume in medium gray and white, respectively. Note the strong reduction in vascularity (gray to white), along with a less pronounced reduction in the lesion volume (left to right).

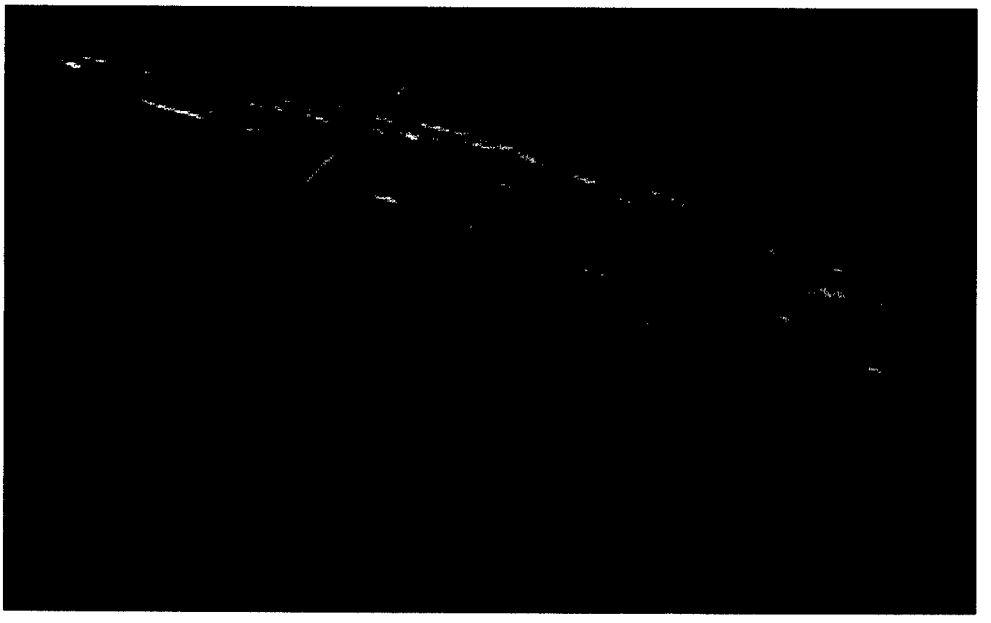

Fig. 2 3D view of a volume combined from three parallel, partly overlapping scans in a 65 year old female with invasive ductal carcinoma.
The total width of this extended view is 7.9 cm. The boundaries between the original scans at about one third and two thirds of the width of the composite image (black arrows) are hardly noticeable.

IV. CONCLUSIONS

The advances described above should increase the sensitivity and specificity of ultrasound imaging in discriminating benign from malignant known masses. Increasingly we and others will look toward expanded roles in the young and mammographically dense breast and in detection of cancers on follow-up studies and in high risk, preclinical disease.

Clinical Trials

Preliminary data analysis and write-up has been completed on new trials and contributions were made to advance 3D image acquisition, display and quantification.

Compound and Sequential Imaging

The registration achieved so far is unexpectedly good and robust. It has promise for an increasing number of applications that could revolutionize the use of ultrasound in medicine, particularly for serial studies. The types of serial exams that might be followed include tracking of tumor size and vascularity for early indications of response to treatment, as well as serial follow-up or even screening exams to reveal abnormal growth. Our new extended 3D field of view imaging appears to greatly increase the changes of achieving these goals.

Image-based Slice Positioning [IBaR]

The results to date continue to be impressive, and at least two companies have implemented aspects of the technique, one with clear acknowledgement of our developments.

Digital ductography development

The technique has been illustrated in concept, but much more work will be required to show practical, routine utility.

V. REFERENCES

1. Tuthill TA, Krücker JF, Fowlkes JB, Carson PL (1998) Automated 3-D US Frame Positioning Computed from Elevational Speckle Decorrelation, Radiology, 209, 575-582.
2. Krüker JF, LeCarpentier GL, Meyer CR, Fowlkes JB, Roubidoux MA, Carson PL, 3D Image Registration for Multimode, Extended Field of View, and Sequential Ultrasound Imaging, submitted to RSNA EJ, available for confidential review at http://deepred.rad.med.umich.edu/previews/index.html , Confidential ID - Reviewer, Password - 3DBreast.
3. Meyer CR, Boes JL, Kim B, Bland PH, LeCarpentier GL, Fowlkes JB, Roubidoux MA, Carson PL (1998a), Semiautomatic Registration of Volumetric Ultrasound Scans, Ultras. In Med. & Biol., in press.
4. Rubin JM, Bude RO, Fowlkes JB, Spratt RS, Carson PL, Adler RS (1997), Normalizing Fractional Moving Blood Volume Estimates with Power Doppler US: Defining a Stable Intravascular Point with the Cumulative Power Distribution Function, Radiology, 205, 757-765.
5. Carson PL, Fowlkes JB, Roubidoux MA, Moskalik AP, Govil A, Normolle D, LeCarpentier G, Nattakom S, Rubin JM (1998), 3D Doppler Image Signal Quantification of Breast Masses, Ultrasound Med. Biol., 24:6, 945-952, 1998.

6. Kremkau FW, Merritt CRB, Carson PL, Needleman L, Nelson TR, Pretorius DH, Rubin JM (1997), Future Directions in Diagnostic Ultrasound, Radiology, 209, 305-311 (review only, no acknowledgement).

7. Fenn RC, Fowlkes JB, Moskalik A, Zhang Y., Roubidoux MA, Carson PL (1997) A hand-controlled, 3-D ultrasound guide and measurement system, in Acoustical Imaging, S. Lees, ed., Plenum Press, N.Y. ISBN 0306457687 TC, v. 23, 237-242.

8. *LeCarpentier, G. L., Meyer, C. R., A., M., Tridandapani, P., Fowlkes, J. B., Roubidoux, M. A., Helvie, M. and Carson, P. L. (1998). " Utility of 3D ultrasound in the discrimination and detection of breast cancer , submitted to RSNA EJ, available for confidential review at: (http://deepred.rad.med.umich.edu/previews/ as user: Reviewer, password: 3DBreast.

9. Carson PL, Fowlkes JB, Roubidoux MA, Moskalik AP, LeCarpentier GL, Helvie M (1997) Basic Advances in 3D Ultrasound Imaging of the Breast Including Vascularity Analysis and Ductography, U.S. Army Breast Cancer Research Program., Oct. 31-Nov 4. Chicago, Poster and Platform Presentation, Proceedings, I, 221-222.

10. LeCarpentier GL, Moskalik AP, Roubidoux MA, Carson PL (1997) 3D Tracking and Display of Mammary Ducts. RSNA, Nov 26-Dec. 1, Chicago, Radiology, 205 (P), 491.

VI. APPENDICES

* = supported primarily by another grant ** = supported primarily by this contract

1. **Tuthill TA, Krücker JF, Fowlkes JB, Carson PL (1998) Automated 3-D US Frame Positioning Computed from Elevational Speckle Decorrelation, Radiology, 209, 575-582.

2. **Krüker JF, LeCarpentier GL, Meyer CR, Fowlkes JB, Roubidoux MA, Carson PL, 3D Image Registration for Multimode, Extended Field of View, and Sequential Ultrasound Imaging, submitted to RSNA EJ, available for confidential review at http://deepred.rad.med.umich.edu/previews/index.html , Confidential ID - Reviewer, Password - 3DBreast.

3. *Meyer CR, Boes JL, Kim B, Bland PH, LeCarpentier GL, Fowlkes JB, Roubidoux MA, Carson PL (1998a), Semiautomatic Registration of Volumetric Ultrasound Scans, Ultras. In Med. & Biol., in press.

4. *Rubin JM, Bude RO, Fowlkes JB, Spratt RS, Carson PL, Adler RS (1997), Normalizing Fractional Moving Blood Volume Estimates with Power Doppler US: Defining a Stable Intravascular Point with the Cumulative Power Distribution Function, Radiology, 205, 757-765.

5. *Carson PL, Fowlkes JB, Roubidoux MA, Moskalik AP, Govil A, Normolle D, LeCarpentier G, Nattakom S, Rubin JM (1998), 3D Doppler Image Signal Quantification of Breast Masses, Ultrasound Med. Biol., 24:6, 945-952, 1998.

6. Kremkau FW, Merritt CRB, Carson PL, Needleman L, Nelson TR, Pretorius DH, Rubin JM (1997), Future Directions in Diagnostic Ultrasound, Radiology, 209, 305-311 (review only, no acknowledgement).

7. *Fenn RC, Fowlkes JB, Moskalik A, Zhang Y., Roubidoux MA, Carson PL (1997) A hand-controlled, 3-D ultrasound guide and measurement system, in Acoustical Imaging, S. Lees, ed., Plenum Press, N.Y. ISBN 0306457687 TC, v. 23, 237-242.

8. *LeCarpentier, G. L., Meyer, C. R., A., M., Tridandapani, P., Fowlkes, J. B., Roubidoux, M. A., Helvie, M. and Carson, P. L. (1998). " Utility of 3D ultrasound in the discrimination and detection of breast cancer , submitted to RSNA EJ, available for confidential review at: (http://deepred.rad.med.umich.edu/previews/ as user: Reviewer, password: 3DBreast.

Theresa A. Tuthill, PhD
Jochen F. Krücker, Dipl Phys
J. Brian Fowlkes, PhD
Paul L. Carson, PhD

Index terms:
Breast, US, 00.12989
Ultrasound (US), experimental
Ultrasound (US), technology
Ultrasound (US), three-dimensional

Radiology 1998; 209:575–582

[1] From the Department of Radiology, University of Michigan Medical Center, 200 Zina Pitcher Pl, Ann Arbor, MI 48109-0553. Received December 23, 1997; revision requested March 23, 1998; revision received April 21; accepted June 9. Supported in part by the U.S. Army Medical Research and Materiel Command under contract no. DAMD17-96-C-6061 and by U.S. Public Health Service grant 1RO1CA55076 from the National Cancer Institute. **Address reprint requests to** P.L.C.

The views, opinions, and/or findings contained herein are those of the authors and should not be construed as an official Department of the Army position, policy or decision.

© RSNA, 1998

Author contributions:
Guarantor of integrity of entire study, J.B.F.; study concepts, J.B.F., P.L.C.; study design, J.B.F., T.A.T.; definition of intellectual content, J.B.F., P.L.C.; literature research, T.A.T.; clinical studies, J.B.F., P.L.C.; experimental studies, T.A.T., J.F.K.; data acquisition and analysis, T.A.T., J.F.K.; statistical analysis, T.A.T., J.F.K.; manuscript preparation, T.A.T., J.F.K.; manuscript editing, T.A.T.; manuscript review, J.B.F., P.L.C.

Automated Three-dimensional US Frame Positioning Computed from Elevational Speckle Decorrelation[1]

For ultrasonographic B-scan images collected by means of a handheld transducer moving in the elevational direction, frame spacings are computed with a speckle-decorrelation algorithm, without additional positioning hardware. Fully developed speckle volumes are automatically segmented and spacing computed from the decorrelation curves. Position accuracy is within 10% for phantoms and 15% for breast studies. The algorithm provides image-based registration, which allows accurate three-dimensional volume rendering.

In three-dimensional ultrasonography (US), the position accuracy of each B-scan frame is essential for accurate volume reconstruction. Even for qualitative reconstruction without position measurement, the image spacing must be adequately fine and uniform to avoid streak artifacts. Current position measurement techniques require use of a supplementary mechanical device to record the location of the transducer head during scanning. We propose an alternative scheme that makes use of the residual correlation between frames to estimate the separation distance. Since the observed speckle patterns are wholly determined by the physical properties of the transducer-given scattering dominated by a large number of random scatterers in the insonified volume, the frame separation can be computed from the degree of speckle decorrelation as calibrated for a specific transducer.

In recent years, reconstruction of three-dimensional US scans for potential clinical use has demonstrated moderate success in areas such as breast cancer diagnosis (1), angiography (2), fetal anomalies (3), and prosthesis modeling (4). Traditionally, for accurate three-dimensional rendering (5), the transducer orientation had to be determined with use of an articulated arm, microcontrolled motor-driven translator, or electromagnetic positioner or by means of optical imaging. By computing frame spacing directly from the image series, the hardware necessary for the scanning process is greatly reduced. The ultimate result of techniques that examine image correlation would, then, be image-based registration of B scans obtained with a freely moving, handheld transducer.

In previous work, Chen et al (6,7) introduced the concept of monitoring of scanning plane motion by means of changes in speckle correlation in the elevational direction. Their decorrelation curves were computed from a small set of training images and were valid only within the focal zone. In this study, the transducer was calibrated to determine a depth-dependent beam correlation width to allow analysis over a larger scanning region. An automated adaptive speckle detector was also employed to ensure only true speckle areas were included in the estimate. The current technology (8,9) could then provide three-dimensional reconstruction with use of real-time imaging and freehand scanning.

Materials and Methods

The rate of speckle decorrelation can be derived by means of statistical analysis of speckle formation. A more detailed derivation is given in the Appendix, but the main points and assumptions are presented here. For fully developed speckle, the intensity image should have an exponential distribution and a constant ratio of mean to standard deviation of 1.0. The amount of speckle change from frame to frame is directly related to the second-

order statistics as determined by the frame separation. Note that in this analysis, the normalized autocovariance is referred to as the correlation function.

The algorithm derivation shows that the intensity correlation function is directly related to the amplitude correlation function, which in turn is proportional to the point-spread-function autocorrelation. Assuming a focused transducer, the beam pattern can then be approximated by means of a Gaussian curve that has a depth-dependent width as the beam goes in and out of the focal region. Consequently, the intensity autocorrelation can also be written as a Gaussian function with respect to the frame spacing and will have a SD of $\sigma_v(z)$, the depth-dependent beam correlation width. This correlation width in the focus can be calculated on the basis of the transducer's physical properties, or the correlation width for a longer range can be calibrated by using a speckle phantom. The final result is that by means of Gaussian curve fitting of the correlation function for speckle regions in a set of B-scan frames, the average frame spacing for that set can be back calculated.

In this study, a commercially available US scanner (LOGIQ 700; GE Medical Systems, Milwaukee, Wis) was used, with a 13-MHz, 1.5-dimensional matrix linear array probe. The transducer had a 6-dB lateral beam width of 1.9 mm and an elevational beam width of 2.0 mm at the focus. B-scan images were obtained with both uniformly and nonuniformly spaced elevational sweeps. The scans were digitized to 8 bits and stored as 379 × 380-pixel images, corresponding to 4-cm² regions. The recorded gray-scale images were then log decompressed to obtain an intensity image series.

Since the decorrelation algorithm holds true for only speckle regions, a speckle "detector" based on first-order statistics was developed. The ratio of mean intensity to SD was computed for a region with a moving three-dimensional volume (21 × 21 pixels × 10 frames). A binary mask was formed that displayed regions in which the ratio of mean intensity to SD was between 0.9 and 1.1, and the two-dimensional mask was assigned to the center frame. Pixels in only the mask region were then used to form the average covariance function.

The depth-dependent beam correlation width of the transducer was determined by using a focal lesion phantom (CIRS; Computerized Imaging Reference Systems, Norfolk, Va). The phantom, which has a densely packed, random distribution of fine particles, provided the minimum number of scatterers in the resolution cell necessary to create fully developed speckle. The transducer was affixed to a linear micropositioner, and 120 B-scan images were obtained in an elevational sweep, with a uniform step size of 50.8 μm. With a moving volume of 10 frames, a mask was determined for the central portion of the scans, a region of 300 × 100 pixels. The average autocovariance was computed for each row in the mask, normalized, and then Gaussian curve fitted. The estimated Gaussian standard deviation at each depth was scaled by the step size to determine the depth-dependent beam correlation width, or $\sigma_v(z)$. The depth dependency was then approximated with a polynomial, resulting in a beam correlation width for the given transducer and scanning settings.

The calibration was first verified on other B-scan series in regions of apparently pure speckle in the phantom, with use of uniform frame spacing from 25.4 to 279.4 μm. The same pixel region, range of ratio of mean intensity to SD,

Figure 1. Representative B-scan breast image demonstrates the variety of complex structures present when the position of the scanning head is calculated. Accurate three-dimensional spatial registration would be necessary to determine the size of the fibroadenoma (arrows) in any selected plane.

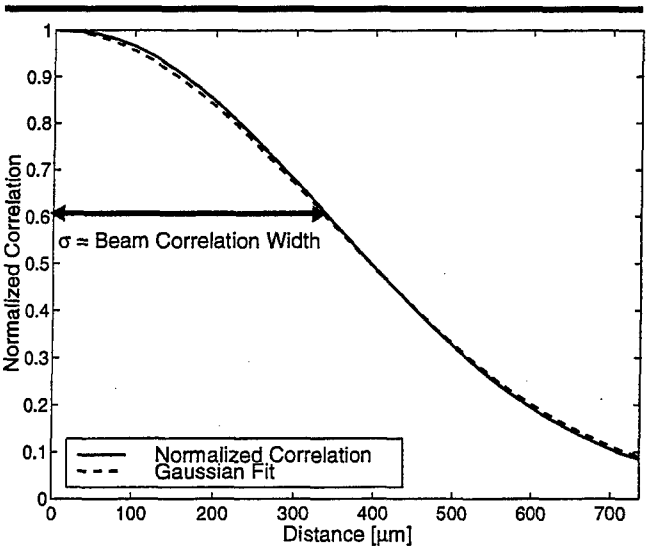

Figure 2. Normalized averaged autocovariance function in the elevational direction for a series of uniformly spaced B scans obtained in a tissue-mimicking phantom. The average was computed over a 30 × 10-mm (300 × 100-pixel) area, and the frame separation was 25.4 μm.

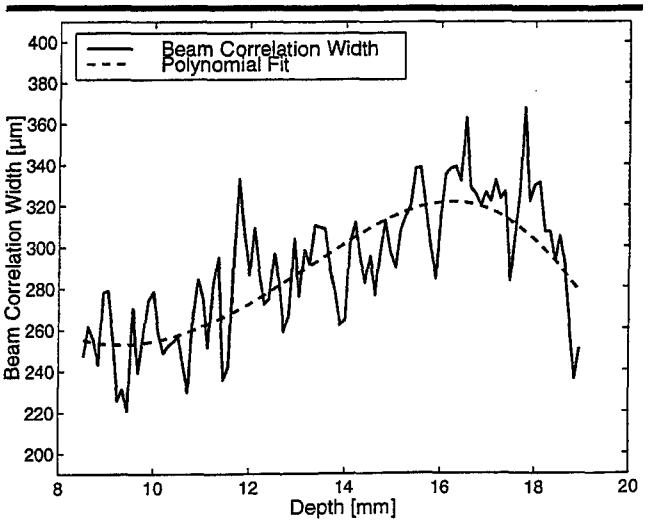

Figure 3. Beam correlation width based on regional covariance curves plotted as a function of depth, for a 13-MHz linear array transducer focused at 1.5 cm.

and number of frames per volume were chosen as were used for the calibration. The speckle-selection and frame-spacing computations were then verified on uniformly spaced scans obtained in a portion of the phantom that contained regions with 3-mm-diameter "voids," spherical regions of weak scatterers.

The algorithm was also tested on a scan series with nonuniform spacing obtained with a freehand scan system (10,11) that allows the user to slide a transducer along a framework at a variable rate. The transducer is affixed perpendicular to the scanning direction to prevent any lateral, range, or rotational movement. Position information to within ±10 μm is stored by means of an encoder connected to a computer. Depending on the frame rate, the transducer must be moved slowly enough to ensure that consecutive frames are not completely decorrelated.

Freehand scans were first obtained in the phantom at "pure" speckle regions and regions containing 3-mm-diameter voids. Finally, clinical images were obtained in a study approved by our institutional review board, with signed informed consent from the subjects. A series of breast scans were obtained in vivo by using the position-encoder apparatus. Figure 1 shows a representative B-scan image obtained with the same settings used for the phantom scans. The frame spacings of these freehand scans were computed by using the calibration data and compared with the spacing given by using the position encoder.

Results

The initial phantom scans were obtained with uniform spacing measured with the micropositioner. Figure 2 shows the average frame-to-frame decorrelation in a pure speckle region, with 25.4-μm spacing, and the Gaussian fit.

For the calibration, a 300 × 100-pixel region (corresponding to 3 × 1-cm² area) was chosen. The resultant depth-dependent beam correlation width of the transducer is shown in Figure 3. Even in regions of apparently "pure" speckle, the distribution of the ratio of mean intensity to SD around its average value of 1.0 broadens as a result of statistical fluctuations when the area in which it is calculated decreases. With a range of ratio of mean intensity to SD of 0.9–1.1 and a window size of 21 × 21 pixels, the area marked as speckle with the speckle selector was roughly 40% of the total region. This low acceptance rate is a trade-off between the high spatial resolution of the mask and the rigorous rejection of nonspeckle regions.

To test the scaling of the calibration set to other frame spacings and to find the maximum image spacing to which accurate separation calculations are possible, the algorithm was applied to subsets of a scan with 25.4-μm frame spacing. A subsample of the frames was obtained to create sets with spacings from 25.4 to 279.4 μm. The result, based on a 300 × 100-pixel region (Fig 4a), shows excellent agreement between calculated and nominal spacings, with less than 3% error up to 125 μm. For larger spacings that approach the correlation half width of the beam, the error increased steadily to −4.9% at 225 μm and −6.1% at 279.4 μm. For smaller regions, the SD of the estimated spacing increased due to the reduced number of pixels. Above 200 μm, the speckle images are fully decorrelated after only two to three frames, which

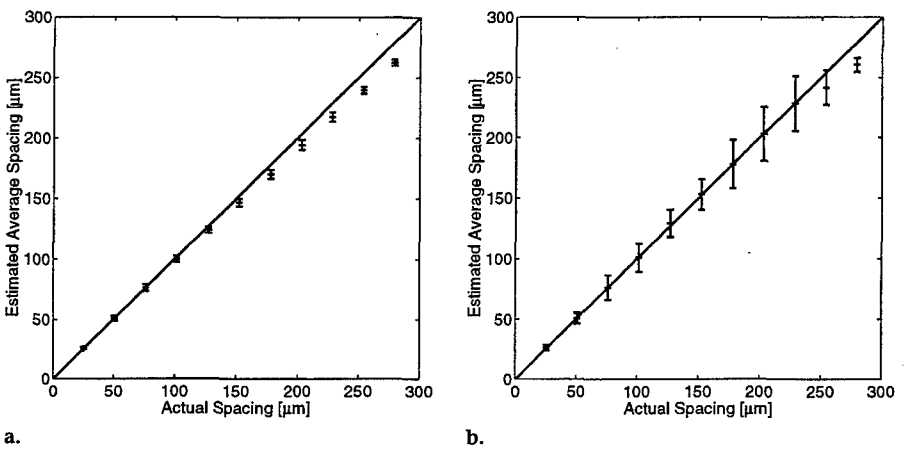

a. b.

Figure 4. Estimated spacing for a series of uniformly spaced scans, computed over 10 frames, with (a) 300 × 100- and (b) 300 × 10-pixel regions. Error bars indicate ±1 SD of average estimation.

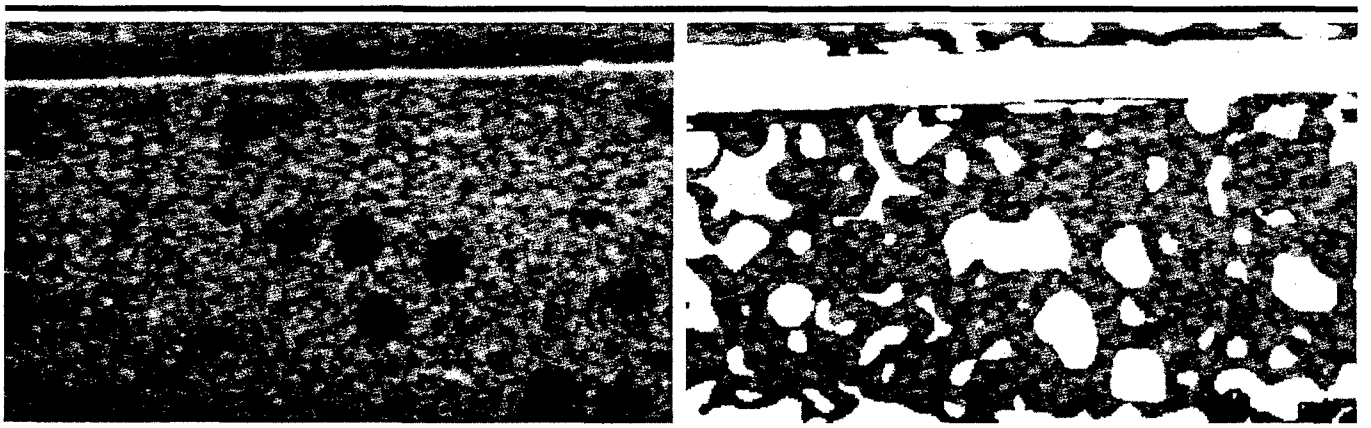

a. b.

Figure 5. (a) B scan was obtained in a tissue-mimicking phantom that contained 3-mm-diameter voids. (b) Corresponding binary speckle-detector mask was determined on the basis of the ratio of mean intensity to SD for a moving volume (21 × 21 pixels × 10 frames). The white regions denote areas where the ratio of mean intensity to SD decreased to between 0.8 and 1.2.

increases the error considerably in the Gaussian fit. However, the average spacing was reproduced well up to 225 μm for a 300 × 10-pixel region in the center of the focal zone (Fig 4b). The improvement in the mean estimate of the section spacing results from the exclusion of pixels outside the elevational focal zone, which in this case was only approximately 30 pixels deep. The theory (Appendix) assumes the pixels are being taken from the focal zones so some systematic error might be anticipated if pixels from outside this region are included. This argues strongly for the use of multiple elevational electronic focusing.

The efficacy of the speckle detector was demonstrated in regions of the phantom that contain speckle and voids (Fig 5a). The boundaries between the small, weakly scattering voids and the background constitute structure that cannot be used for the section spacing computation. With use of a range for ratio of mean intensity to SD of 0.8–1.2, the selector successfully masked out the voids, leaving the "pure" speckle regions for calculation (Fig 5b).

For the freehand scanning experiments, the frame rate was set to the video rate of 30 Hz. Assuming the largest discernible frame separation is 250 μm, the maximum allowable transducer speed for this frame rate was 7.5 mm/sec. Scan sets of the phantom were recorded as the sonographer attempted to move the transducer at either uniform or variable speeds. Figure 6a displays the estimated and actual frame spacing in roughly uniform scanning, and Figure 6b shows the results in a scan set for which the sonographer increased the transducer speed midway through scanning, over a region of homogenous speckle. The speckle-decorrelation estimator tracked the actual position well, with a mean error of 7% root-mean-square for the frame spacing and of 3% root-mean-square for the total distance traveled. Scanning sweeps performed over the void-filled portion of the phantom showed similar results (Fig 6c, 6d). The total distance traveled in the two-speed scan in Figure 6c is shown in Figure 7a, as is the corresponding percentage of actual pixels used (Fig 7b) as determined with the adaptive mask for ratio of mean intensity to SD. The square of the correlation, R^2, defined as 1 minus the ratio of the variation of the residuals over the variation in position, demonstrates the accuracy of the estimate.

In the clinical study, one image series was obtained from a set of breast scans that depicted a fibroadenoma (Fig 1). The same transducer and scanner settings were

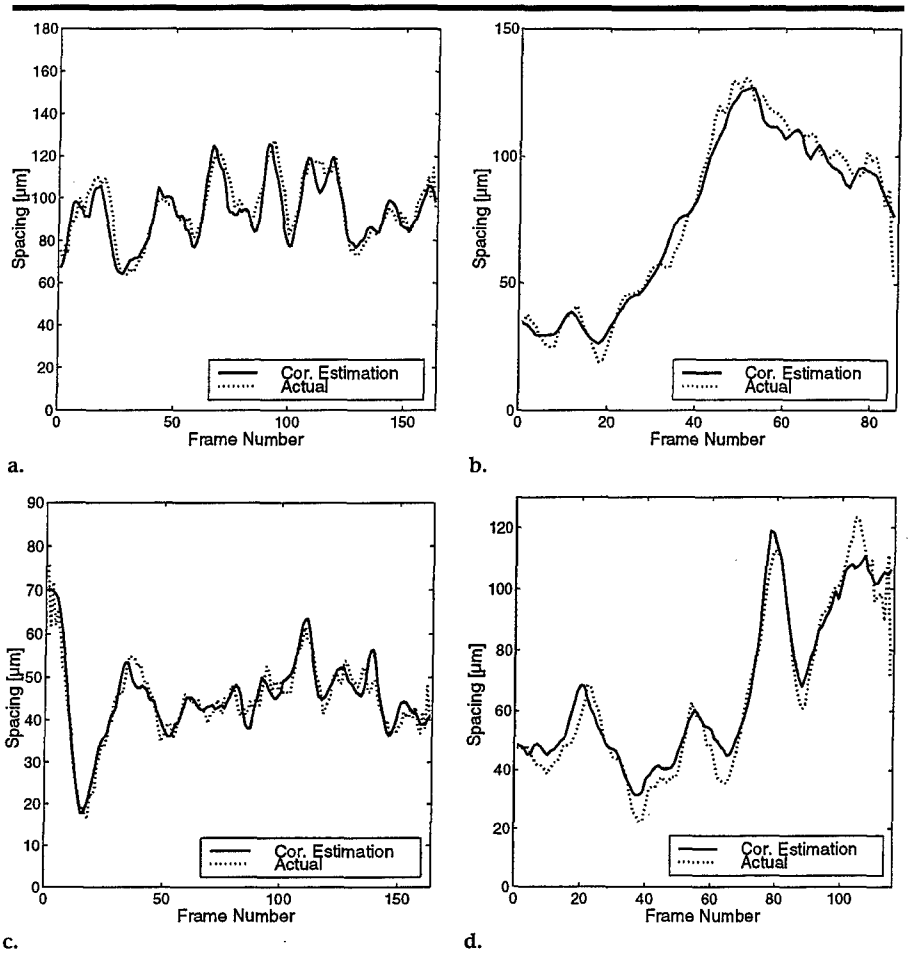

Figure 6. Graphs demonstrate comparison of decorrelation-estimated image separation with spacing computed from position-encoder information for freehand scan sets. (**a**) Scans obtained with approximately uniform speed over the speckle region in the phantom. (**b**) Scans obtained with two speeds over the same region as in **a**. (**c**) Scans obtained with approximately uniform speed over the void region in the phantom. (**d**) Scans obtained with two speeds over the same region as in **c**. In **a–d**, *Cor. Estimation* = correlation estimation.

used as were used for the phantom scans. Given only one focus, the B-scan image is not ideal and the tumor outline is unclear. However, the speckle correlation estimate for the frame spacing tracked the position data with an accuracy of 87% (Fig 8). The region within and surrounding the tumor deviated from true speckle, and the number of pixels used in the mask for ratio of mean intensity to SD decreased to 1,350. A transverse scan (with the axial and elevational resolution) through the tumor was reconstructed by using the position information (Fig 9a). The resolution of this out-of-plane scan is comparable to that of the original B scan. Finally, Figure 9b shows a reconstructed C-scan section (with the lateral and elevational resolution) obtained midway through the lesion.

In another clinical patient, the sonographer obtained a breast scan while varying the scanning speed. A transverse image was then reconstructed with the assumption of a uniform scanning speed (Fig 10a). The arrow denotes the area where the sonographer slowed down, and the actual frame spacing is decreased. Figure 10b shows the reconstruction obtained with the estimated frame spacing and interpolation. Incorporation of the spacing information subjectively reduced blurring and increased image quality, with better definition of connective tissue structures. For this scan, the maximum position error was 1.49 mm (mean error, 13.9%).

As a final test, a freehand scan that allowed tilting was obtained in the phantom. The transducer was swept smoothly through 30° with the transducer-phantom interface as the axis of rotation. The estimated row spacing was averaged over 250 frames. Whereas exact positioning could not be recorded, the estimated frame spacing increased linearly with depth (Fig

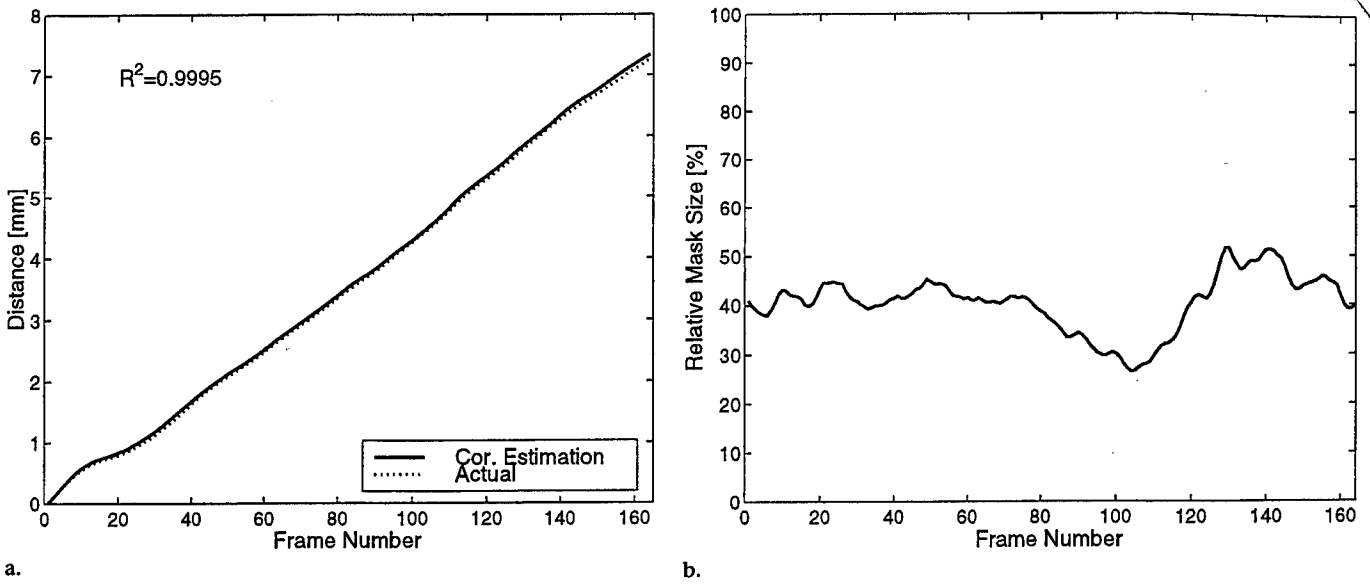

Figure 7. (a) Estimated values for the total distance traveled by the transducer, corresponding to the accumulation of the frame spacings shown in Figure 6c. *Cor. Estimation* = correlation estimation. (b) Corresponding percentage of pixels masked by the speckle selector and used in the section spacing estimation.

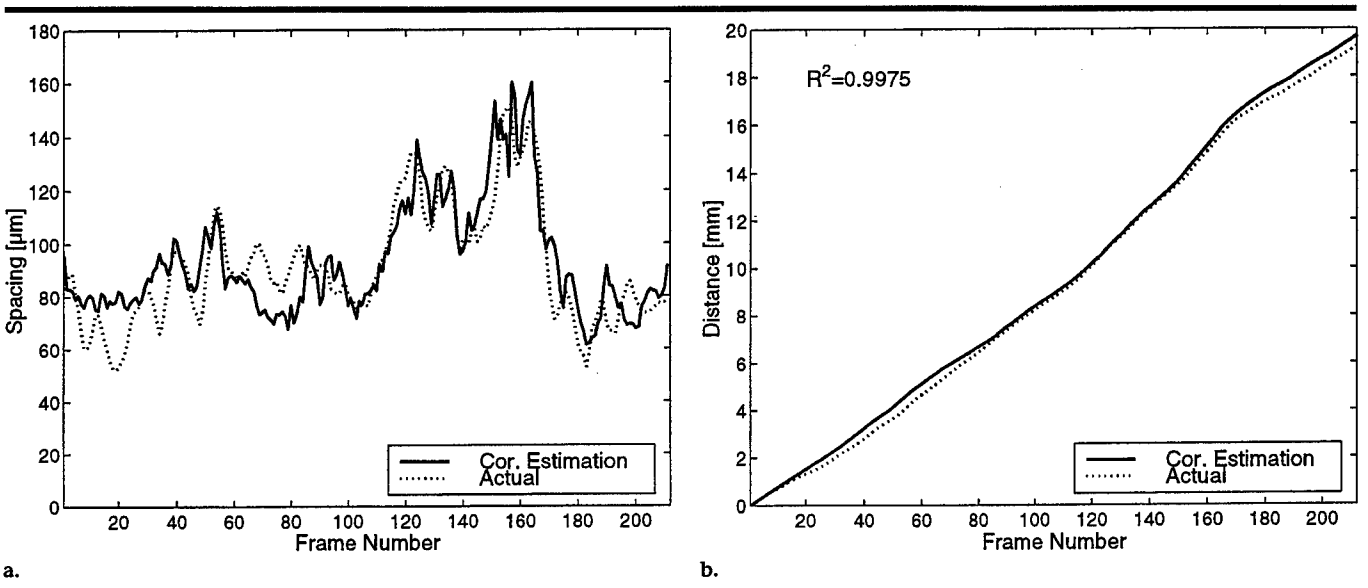

Figure 8. (a) Estimated frame spacing for breast images obtained in a freehand scanning study. (b) Corresponding total lateral distance scanned by the transducer. In a and b, *Cor. Estimation* = correlation estimation.

11), indicating the feasibility of tracking transducer tilt and possibly other motions in addition to linear translations.

Discussion

The elevational decorrelation curves matched well with the Gaussian function as predicted by the theory. It should be noted that the error in the autocovariance estimate increased with lag number or the total distance between frames. As the decorrelation curve decreased, the estimate became unreliable, and thus only point values greater than 0.3 were used in the Gaussian curve fit. For large frame spacings, the speckle decorrelated in just a few frames, which reduced the number of points used in the curve fit and thus increased the error for the section spacing approximation.

The beam correlation width for the focused transducer showed interesting results as a function of depth. The curve peaked just above the focal region. Close to the transducer, a fast decorrelation was expected due to the incoherent nature of the beam in the near zone. At large depths, a fast decorrelation rate was also expected due to the dominance of noise in the signal and the incoherence of the beam.

For linear scans, the speckle-decorrelation technique showed excellent results in estimating frame separation and tracking the overall distance traveled. As long as the sonographer did not exceed motion of 200 μm per frame and sufficient areas of speckle were present in the scans, the frame spacing was accurately estimated.

The increased error in the clinical scans

was expected. When the translator framework was placed on the breast, pressure was applied to maintain good contact between the skin and transducer. As the transducer was moved along the surface, there was a slight repositioning of the underlying tissue, which was undetected by the position encoder. Also, breast contains large amounts of phase-aberrating tissue that would degrade the beamforming process and increase the beam correlation width of the transducer. The result is a bias in the estimated frame separation below its actual value. However, it should also be noted that the "actual" separation based on the encoding system may also not be correct due to relative motion between the frame and the tissue. This motion would actually be accounted for by the image-based registration technique, and as such, the result may actually be more accurate than the "actual" result used for comparison. In the same sense, the image-based registration technique would give more accurate spatial measurement in tissues moving rapidly (eg, with respiration) than would measurements based on an external frame of reference. This would be particularly helpful in compounding of pulsed Doppler images (12).

The current setup has some limitations critical to its use in a clinical setting. The scanning speeds for this study were quite slow (maximum velocity, 7.5 mm/sec at 30 Hz). Use of higher frame rates would alleviate this problem, though there is a trade-off with reduced number of focal zones and smaller field of view. In theory, only limited amounts of information, obtainable in real time, would be required, and thus limitations of scanning speed would be reduced.

As previously noted (7), this technique could be implemented in real time since only a portion of the image is needed to determine transducer motion. Similar to or in conjunction with power Doppler estimations, a few pulses at high pulse repetition frequency could be transmitted between acquisition of data from two consecutive images. The correlations could be computed at high speeds with a programmable image processor board as is used with other US imaging technology (13,14).

For the clinical study, the transducer was limited to translational movement. The framework, which also permits rotation around a fixed axis, was designed for scanning of large body parts such as breast, liver, or Achilles tendon. These two encoded motions were chosen as the most useful in circumstances such as scanning up to and under the ribs. Our future work will emphasize regional speckle analysis to calculate motion and thus allow rotation of the transducer. A preliminary frame-to-frame correlation can also be used to account for lateral and axial motion. This would permit scanning with a freely held transducer without use of any position framework.

The speckle-decorrelation algorithm provides image-based registration of US frame sections obtained with a freely moving handheld transducer. Findings in this study have shown that for three-dimensional B-scan sets, the section spacing can be determined effectively on the basis of the speckle decorrelation from frame to frame. By moving a transducer slowly over the region of interest and restricting additional degrees of freedom, the frame spacing is calculated without use of any additional position-encoding hardware. While the errors for the absolute frame distance vary near 10%, the accumulative error, which is critical for tumor or other volume estimation, is much smaller. The efficacy of the technique was further demonstrated (or suggested) in clinical breast scans, and additional work should enhance image-based reconstruction of three-dimensional images.

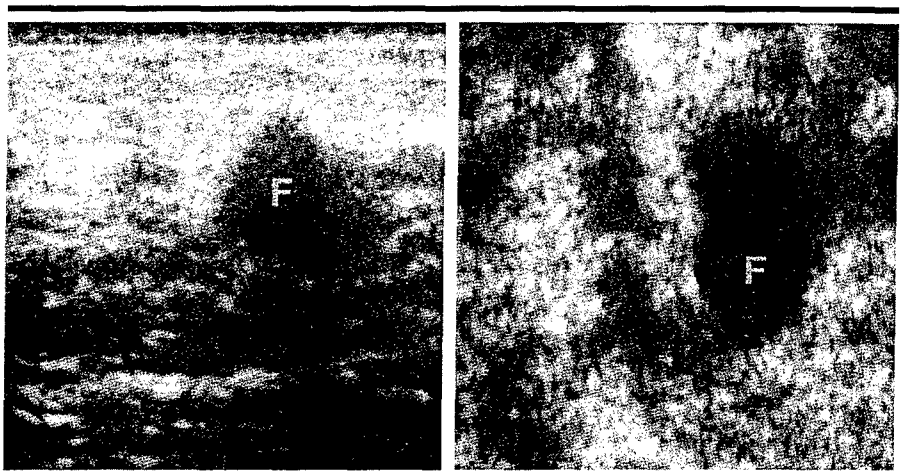

a. b.

Figure 9. (a) Transverse image of a breast fibroadenoma (*F*) formed by selecting a vertical section through a set of B-scan images and correcting for transsducer position. (b) C-scan image obtained from the same B-scan set.

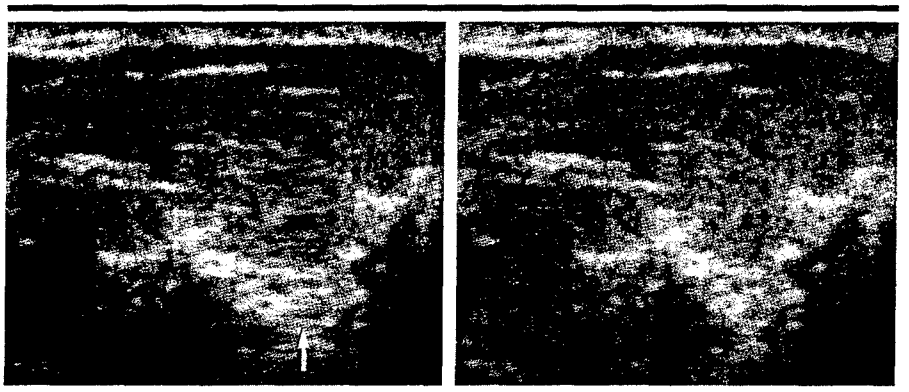

a. b.

Figure 10. Reconstruction images of a transverse image that was obtained from a set of breast scans. (a) Reconstruction image with uniform spacing between frames. Arrow indicates a region where the sonographer slowed down during scanning. (b) Reconstruction image with variable frame spacing determined with the speckle-decorrelation algorithm.

Appendix

Speckle is formed by the coherent scattering from subresolvable particles. The derivation for this algorithm starts with a stochastic analysis of the received amplitude signal (15,16). If the number of

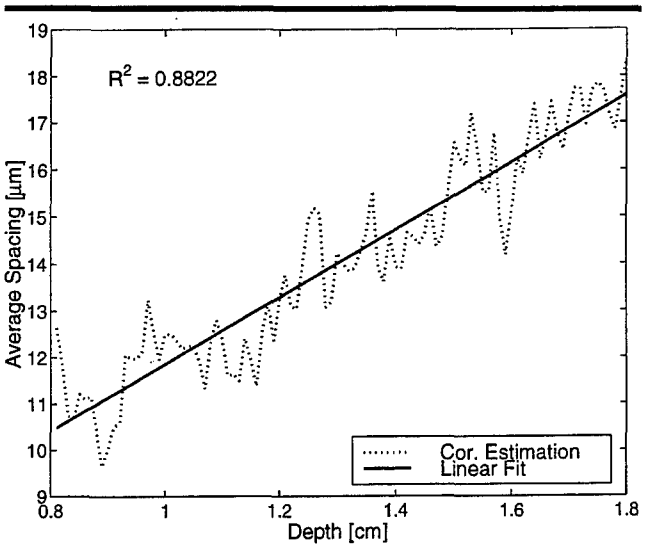

Figure 11. Estimated depth-varying frame spacing for phantom scan series obtained by hand tilting a transducer through an approximately 30° arc, with the face of the scanning head as the axis of rotation. The spacing at each depth was averaged over 250 frames. *Cor. Estimation* = correlation estimation.

independent scatterers in the scanning volume is large, then on the basis of the central limit theorem, the sum of the complex signals will have a Gaussian distribution with mean of zero and variance of σ^2. With use of a transformation of variables, the amplitude, A, is shown to have a Rayleigh distribution, p,

$$p_A(A) = A/\sigma^2 \exp(-A^2/2\sigma^2).$$

Analysis of the first-order statistics provides an interesting result: The ratio of the mean intensity to SD is a constant 1.91.

For this analysis, the statistics for the intensity (I) or squared amplitude are required. By again applying a variable transformation, the intensity is shown to have a negative exponential distribution,

$$p_I(I) = 1/2\sigma^2 \exp(-I/2\sigma^2),$$

which has a mean of $2\sigma^2$ and a variance of $4\sigma^4$. Thus for fully developed speckle, the intensity image should have a constant ratio of mean intensity to SD of 1.0.

Second-Order Statistics

To relate the fluctuations in image intensity from frame to frame, the second-order statistics of the speckle are used (17). The amplitude autocorrelation (R_A) for positions r_1 and r_2 is defined as

$$R_A(r_1, r_2) = \langle A(r_1)A(r_2)\rangle,$$

and the autocovariance (C_A) is

$$C_A(r_1, r_2) = R_A(r_1, r_2) - \langle A(r_1)\rangle\langle A^*(r_2)\rangle,$$

where $\langle\ \rangle$ denotes the expected value. The normalized autocovariance, ρ, is referred to as the correlation function.

The amplitude signal is formed from the convolution of the transducer point-spread function with the insonified scattering train. The autocorrelation function of the amplitude is the convolution of the autocorrelation functions for the point-spread function and the scatterers. For pure speckle, the scatters are independent and the autocorrelation can be approximated as a δ function. Consequently, the amplitude autocorrelation is directly proportional to the point-spread-function autocorrelation.

For a focused transducer, the point-spread function near the focal zone is proportional to the square of the Fourier transform of the transducer aperture (18). With the rectangular linear array, focusing of the electronic beam apodizes side lobes. The beam pattern can then be approximated with a Gaussian curve, and the point-spread-function autocorrelation will also be Gaussian (19),

$$\rho(r_1, r_2) = \exp[-(r_1 - r_2)^2/2\gamma_z^2],$$

where γ_z is related to the beam width.

After a similar derivation (17), the intensity autocorrelation is shown to have the form

$$R_I(r_1, r_2) = \langle I(r_1)I(r_2)\rangle = \langle I_o\rangle^2 [1 + |\rho(r_1, r_2)|^2]$$

and the autocovariance is

$$C_I(r_1, r_2) = \langle I_o\rangle^2 |\rho(r_1, r_2)|^2,$$

where $\langle I_o\rangle$ is the average image intensity. The intensity correlation function is thus directly related to the amplitude correlation function.

This one-dimensional analysis can also be expanded to include temporal correlation properties for relative motion between the transducer and the insonified tissue (20). For a transducer velocity of v_x (in distance per frame) and B-scan frame number n, the normalized intensity elevational covariance for a single pixel location then has a Gaussian shape (19),

$$C(n, z) \propto \exp[-(v_x n)^2/2\sigma_v^2(z)],$$

where $\sigma_v(z)$ is the depth-dependent beam correlation width and is determined by the transducer properties. By fitting the correlation function for a set of N frames to a Gaussian curve, the average frame spacing for that set can be back calculated.

Acknowledgments: The authors are indebted to Gerald LeCarpentier, MD, for his work with the position encoder. Thanks also to GE Medical Systems and Diasonics Vingmed Ultrasound, Santa Clara, Calif, for supplying the US equipment.

References

1. Carson PL, Moskalik A, Govil A, et al. The 3D and 2D color flow display of breast masses. Ultrasound Med Biol 1997; 23: 837–849.
2. Ritchie CJ, Edwards WS, Mack LA, Cyr DR, Kim Y. Three-dimensional ultrasonic angiography using power-mode Doppler. Ultrasound Med Biol 1996; 22:277–286.
3. Nelson TR, Pretorius DH, Sklansky M, Hagen-Ansert S. Three-dimensional echocardiographic evaluation of fetal heart anatomy and function: acquisition, analysis, and display. J Ultrasound Med 1996; 15:1–9.
4. He P, Xue K, Murka P. 3-D imaging of residual limbs using ultrasound. J Rehabil Res Dev 1997; 34:269–278.
5. Fenster A, Downey DB. 3-D ultrasound imaging: a review. IEEE Eng Med Biol 1996; 15:41–51.
6. Chen JF, Fowlkes JB, Carson PL, Moskalik A. Determination of scan-head motion using decorrelation of speckle (abstr). Med Phys 1995; 22:974.
7. Chen JF, Fowlkes JB, Carson PL, Rubin JM. Determination of scan-plane motion using speckle decorrelation: theoretical considerations and initial test. Int J Imaging Syst Technol 1997; 8:38–44.
8. Fowlkes JB, Carson PL, Moskalik A, Chen JF, Rubin JM. Method and apparatus for composition and display of three-dimensional image from two-dimensional ultrasound. International patent pending PCT/US96/10189. 1996.
9. Li M. System and method for 3-D medical imaging using 2-D scan data. US patent 5,582,173. Dec 10, 1996.
10. Fenn RC, Fowlkes JB, Roubidoux MA, Moskalik A, Carson PL. A miniature position-encoding system for flexible, hand-controlled, 3D ultrasound (abstr). J Ultrasound Med 1997; 16(suppl):11.

11. Fenn RC, Fowlkes JB, Moskalik A, et al. A hand-controlled, 3-D ultrasound guide and measurement system. In: Lees S, Ferrari LA, eds. Acoustical imaging. New York, NY: Plenum, 1997; 237–242.
12. Moskalik A, Carson PL, Meyer CR, Fowlkes JB, Rubin JM, Roubidoux M. Registration of three-dimensional compound ultrasound scans of the breast for refraction and motion correction. Ultrasound Med Biol 1995; 21:769–778.
13. Basoglu C, Reeve J, Kim Y, Marquis S. UWGSP8: a programmable ultrasound subsystem for native image processing. SPIE Med Imaging 1996; 2707:378–388.
14. Weng L, Tirumalai AP, Lowery CM, et al. US extended field-of-view imaging technology. Radiology 1997; 203:877–880.
15. Abbot JG, Thurstone FL. Acoustic speckle: theory and experimental analysis. Ultrason Imaging 1979; 1:303–324.
16. Tuthill TA, Sperry RH, Parker KJ. Deviations from Rayleigh statistics in ultrasonic speckle. Ultrason Imaging 1988; 10:81–89.
17. Wagner RF, Smith SW, Sandrik JM, Lopez H. Statistics of speckle in ultrasound B-scans. IEEE Trans Sonics Ultrason 1983; SU-30:156–163.
18. Macovski A. Medical imaging systems. Engle Cliffs, NJ: Prentice Hall, 1983; chap 9.
19. Wear KA, Popp RL. Methods for estimation of statistical properties of envelopes of ultrasonic echoes from myocardium. IEEE Trans Med Imaging 1987; MI-6:281–291.
20. Adler RS, Rubin JM, Fowlkes JB, Carson PL, Pallister JE. Ultrasonic estimation of tissue perfusion: a stochastic approach. Ultrasound Med Biol 1995; 21:493–500.

3-D Image Registration for Multimode, Extended Field of View, and Sequential Ultrasound Imaging

Jochen F. Krücker, Dipl.-Phys., Gerald L. LeCarpentier, Ph.D., Charles R. Meyer, Ph.D.,
Marilyn A. Roubidoux, M.D., J. Brian Fowlkes, Ph.D., Paul L. Carson, Ph.D.

Department of Radiology
University of Michigan Medical Center
Ann Arbor, MI, USA

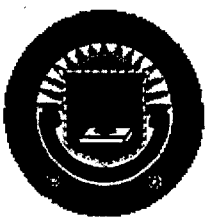

Correspondence:
Paul L. Carson, Ph.D.
University of Michigan Medical Center
Department of Radiology
Kresge III, R3315
200 Zina Pitcher Place
Ann Arbor, MI 48109-0553
Vox: (734) 763-5884
Fax: (734) 764-8541

Acknowledgment: This work was supported in part by the U.S. Army Medical and Material Command under DAMD17-96-C-6061 and, to a lesser extent, by PHS Grant # R01CA55076 from the National Cancer Institute.

[Next: Abstract]

[Title Page | Abstract | Introduction | Materials and Methods]
[Results | Discussion | References]

3-D Image Registration for Multimode, Extended Field of View, and Sequential Ultrasound Imaging

Jochen F. Krücker, Dipl.-Phys., Gerald L. LeCarpentier, Ph.D., Charles R. Meyer, Ph.D.,
Marilyn A. Roubidoux, M.D., J. Brian Fowlkes, Ph.D., Paul L. Carson, Ph.D.

Abstract

Several potential uses of image registration and new display techniques in 3-dimensional ultrasound imaging are demonstrated in three examples, representing several types of applications: First, the gray-scale information of a color-flow image set was coregistered with a high resolution gray-scale set covering the same region of interest. The high accuracy achieved in this registration suggests that this technique can create improved images from combined ultrasound modes. Second, several parallel, partly overlapping gray-scale scans of a female breast with several lesions were coregistered and combined into one larger volume. Only in this extended field of view could the lesions be viewed simultaneously and their relative sizes and positions be appreciated, suggesting the potential of better detection of changes in breast regions being followed for potential cancer. Third, the image registration was applied to a series of ultrasound breast exams for cancer therapy assessment. In spite of considerable tumor shrinkage between the two scans obtained several weeks apart, the coregistration mapped the dominant features in the region of interest and thus facilitated tracking of changes over time, both with direct comparison and with displays that highlighted changes. The quality of the semiautomatic coregistrations achieved and the significance of the applications demonstrated here indicate that image registration may become a valuable tool in improving ultrasound diagnostics.

[Previous: Title Page] [Next: Introduction]

[Title Page | Abstract | Introduction | Materials and Methods]
[Results | Discussion | References]

Introduction

Image registration or coregistration, the alignment of two or more 2-dimensional (2-D) or 3-dimensional (3-D) images of an object, has been applied to medical imaging for more than ten years. One major application of medical image registration is fusion of morphological images such as magnetic resonance imaging (MRI) and X-ray computed tomography (CT) with functional studies such as positron emission tomography (PET) and single photon emission computed tomography (SPECT) (1-7). Other applications of coregistrations include motion detection (8, 9), subtraction imaging (10, 11), and treatment planning (12, 13). A comprehensive review of different approaches and techniques in medical image matching can be found in (14).

Until recently, ultrasound image registration has not been successful, partly because of the small 2-D field of view and possibly strong tissue motion and deformation which make it difficult to obtain consistent image pairs for coregistration using conventional manual scanning.

With the advent of 3-D sonography in research (15, 16) and, more recently, in commercially available ultrasound scanners, volumetric ultrasound data have become available and can, in principle, be registered like 3-D data sets from other imaging modalities. However, the speckle noise and image artifacts usually present in ultrasound images and the strong angular dependency of the apparent brightness of specular reflectors challenge the robustness of registration algorithms.

Apparently the first successful coregistration of 3-D ultrasound scans in a phantom and in the breast was reported in (17), using registration software that required user definition of homologous points, lines, and planes in the data sets. Semiautomatic coregistrations of ultrasound scans were achieved very recently (18, 19) using software based on the mutual information (MI) of two data sets. The same software was used in this study to demonstrate three examples of potential applications of coregistration in ultrasound breast imaging. The display possibilities in this electronic medium, especially the movie features, should allow better visualization of registration quality and assessment of errors than conventional journals.

The gray-scale image obtained along with the color information in Doppler modes usually suffers from poor spatial resolution compared to the high resolution obtainable in the gray-scale-only mode. After registration of a 3-D Doppler mode data set with a gray-scale set, the color information can be superimposed on a high resolution gray-scale background, thus extracting the best of both imaging modes. Potentially, this allows more accurate diagnosis and higher sensitivity in lesion detection by displaying flow information in place with a high quality gray-scale image.

The small field of view (FOV) usually covered by a high resolution scanhead may be insufficient to use the full capabilities of 3-D ultrasound to detect and track changes in breast regions being screened or followed for possible lesions or response to treatment. Often the FOV is also too small to use the full advantages of 3-D in displaying morphologic distortions of normal tissue and flow surrounding the mass and differences between the possible mass and a statistically robust sampling of surrounding tissues. To create a complete or more complete image of the breast, the small volume covered by a single scan can be extended by repeatedly scanning the breast in parallel, partially overlapping sweeps which can then be combined using coregistration of the overlap. Compared to a commercially available 2-dimensional extended filed of view approach (20, 21), our method allows much faster acquisition of 3-dimensional volumes and is applicable as a post-processing scheme after the individual scans have been obtained.

In ultrasound screenings of the breast, some malignant changes are manifest as changes in echogenicity, texture, and morphology. Early detection of these changes can improve survival rates (22). Changes in a structure's size or shape can also aid detection of a malignancy or give important feedback in serial ultrasound exams for the assessment of response to cancer therapy. Coregistration of 3-D ultrasound exams can facilitate the temporal tracking of changes by coregistering the suspect regions of interest imaged at different times, thus allowing direct comparison of the 'before' and 'after' texture and morphology.

[Previous: Abstract] [Next: Materials and Methods]

[Title Page | Abstract | Introduction | Materials and Methods]
[Results | Discussion | References]

Materials and Methods

A LOGIQ 700 ultrasound scanner (**GE Medical Systems**, Milwaukee, WI) with a 12 MHz 1.5-dimensional matrix linear array probe was used to obtain 3-D data sets of the breast. The probe was mounted in a holder that restricted it to a linear motion in the elevational direction (perpendicular to the image plane) while electronically encoding the position of the probe. A more detailed description of the data acquisition scheme can be found in (23).

The holder was placed on the breast and the transducer slowly moved by hand over the region of interest. The high resolution gray-scale (GS), frequency-shift (f-CDI), and power-mode color Doppler (p-CDI) images obtained were then interpolated and resampled with a uniform elevational spacing of approximately 0.4 mm using the position data stored along with the images. Display and registration of the data sets were performed using AVS/5 and AVS/Express (**Advanced Visual Systems**, Waltham, MA).

The 3D image registration software **MIAMI Fuse** was originally developed for fusion of data sets from multiple imaging modalities including various combinations of MRI, CT, PET, and SPECT.

To define the approximate relative position of the two data sets to be coregistered, three control points have to be defined in each set. This is usually done by assuming the images were obtained in the same location and in the same orientation and requires very limited user interaction. The algorithm then repeatedly performs geometrical transformations, rigid or full affine, on one of two sets and maps it onto the second set until the best fit between the two sets is found. Here, the mutual information (24, 25) of the data sets is used as a cost function to determine the quality of a fit. With more control points, warping transformations can be performed, but that was not done in this study. For a more detailed description of the algorithm and evaluation of its performance with PET/CT, PET/MRI and SPECT/CT multimodal data sets see (26). More details on the application of this image registration software to 3-D ultrasound data sets are given in (19).

The registration software was used here to demonstrate registration of 3-D ultrasound scans of the breast for three different applications. For each class of application, one typical case is displayed to demonstrate its potential value in ultrasound diagnostics.

All patient data were acquired after informed consent was obtained.

1. The first application is the fusion of color information from Doppler imaging modalities with gray scale information from a high resolution gray-scale scan of the same volume. For this purpose, the right breast of a forty year old female patient was scanned in f-CDI mode and, several minutes later, in high resolution gray-scale mode, using average elevational frame spacings of 0.43 mm and 0.47 mm, respectively. The gray-scale information of the two scans was then coregistered and displayed in various ways to evaluate the goodness of match.

2. Extended 3-D field of view imaging is the second application demonstrated in this study. Three parallel, high resolution gray scale scans were obtained in the left breast of a 65 year old woman diagnosed with a 60 mm invasive ductal carcinoma. The relative position and alignment of the scans is shown schematically in **Figure 1**. Starting with a scan in the center of the region of interest (B, average elevational frame spacing 0.32 mm), the 4 cm wide aperture of the transducer was then shifted 1 to 3 cm medially (A, frame spacing 0.29 mm) and laterally (C, frame spacing 0.37 mm), respectively, before the second and third scans. Thus, 3-D data sets with 25% to 75% overlap (AB, BC) were obtained. Volume registration was then performed on the overlapping regions to find the necessary transformations and exact relative positions of the data sets, mapping scan A and C into the reference frame given by scan B.

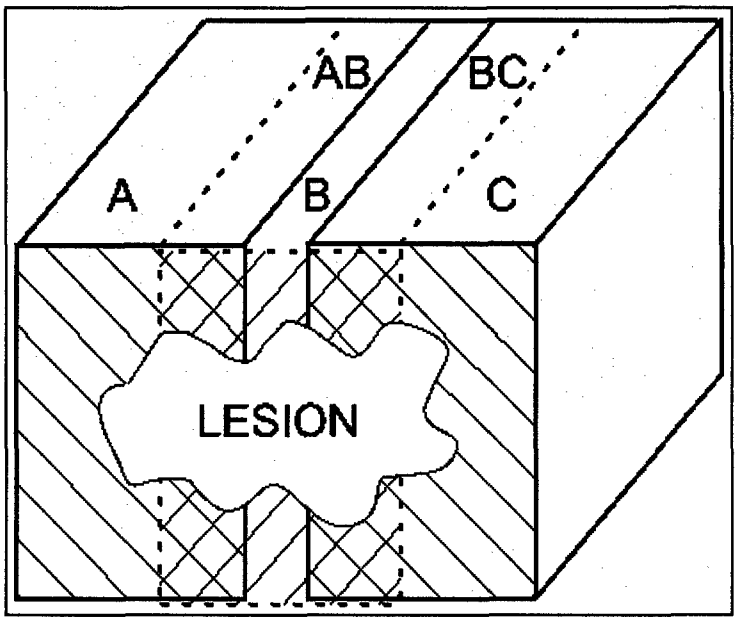

Figure 1. The diagram shows the relative positions of three individual scans A, B, and C, combined into one extended 3-D field of view. The three scans are approximately parallel and overlap at least 25% to achieve sufficient accuracy in the coregistration. Scan B serves as a reference, the overlap AB is used to align scan A relative to B, and similarly BC is used to align C relative to B.

3. The third application presented in this article is the registration of ultrasound scans obtained several weeks apart in the course of a serial study. For this application, the same subject was scanned as for the extended field of view imaging. The central lesion in the left breast of the woman was scanned four times, 8 days before and 29, 55, and 78 days after the first of four cycles of CAF (Cytoxin, Adriamycin, Flourouracil) chemotherapy. The second scan served as a reference relative to which the first, third and fourth scan were coregistered. Although visual inspection of the scans showed significant changes of the lesion, the coregistrations were performed without prior cropping or otherwise pre-processing the image sets. While this inherently increases the inaccuracy of the coregistration, it does serve to demonstrate the feasibility of using ultrasound image registration for evaluation of serial studies without significant user interaction.

In each application, the quality of the coregistration was evaluated by displaying the registered image sets side by side and manually defining pairs of corresponding feature landmarks in the two sets. The mean of the distances between point pairs defining common landmarks was then used as an estimate of the alignment errors after registration.

[Previous: Introduction] [Next: Results]

[Title Page | Abstract | Introduction | Materials and Methods]
[Results | Discussion | References]

Results

1. Multimodal Ultrasound Imaging

Figures 2 and **3** show the results of registering a 3-D f-CDI volume with a high resolution gray-scale volume. The two image volumes were acquired sequentially during a single patient visit. The forty year old female patient was diagnosed with right infiltrative ductal carcinoma. Note the 13 mm spiculated mass which appears in both **Figures 2(b)** and **3** (white arrow).

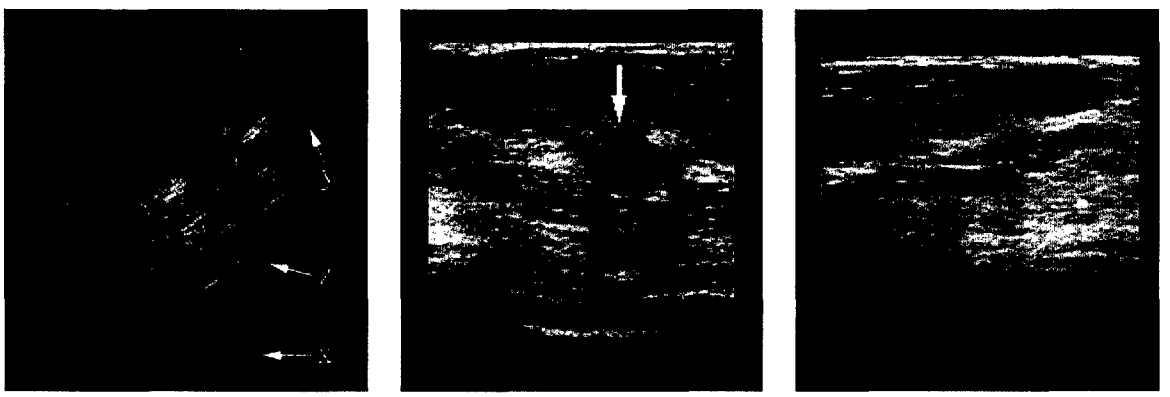

(a) **(b)** **(c)**

Figure 2. Composite representation of an f-CDI volume coregistered with a high resolution gray-scale volume. The high resolution gray-scale images are pseudo-colorized and superimposed onto the gray-scale of the f-CDI set. The scans were performed minutes apart. **(a)** Three orthogonal planes of the 3-D coregistered volume. The white labels indicate our naming scheme for the three planes. **(b)** Axial-lateral (z) scan plane. The white arrow points at the 13 mm spiculated mass. **(c)** Axial-elevational (x) transverse plane. Click each image to view its full sized counterpart. Click **here** for a Quicktime movie (444 kB) scanning through the entire volume and containing the frames shown in **(a)-(c)**. For a high-quality version of the same movie (1.2 MB), click **here**.

In **Figure 2**, the volumetric data is shown as composite images of the f-CDI and the high resolution gray-scale scans. **Figure (a)** displays three orthogonal planes of the 3-D volume, **(b)** and **(c)** display the axial-lateral and axial-elevational planes, respectively. The gray-scale component of the f-CDI is represented with a "gray-scale" map, while the high resolution gray-scale is colorized by the blue to red spectrum, representing dark to light echo regions. The two image sets are then superimposed onto each other. Note the overlap of features in all three images of the figure, with reds and yellows overlapping the lighter features. To view a Quicktime movie (444 kB) scanning through the entire volume, click **here** or follow the link in the figure caption.

In **Figure 3**, the particular scan plane shown in **Figure 2(b)** is presented in a different way. In this case, the coregistered planes are not combined into a composite view. Rather, a diagonal line separates the gray-scale from the f-CDI (upper left) from the high resolution gray-scale image (lower right). The viewer is then able to see the alignment of various features at the diagonal boundary for comparison. Note that the sharp borders of the spiculated mass (white arrow) clearly visible in **Figure 3(b)** are barely discernible in the gray-scale from the f-CDI image shown in **Figure 3(a)**. In a Quicktime "wiper" movie (348 kB), the viewer can appreciate both the accuracy of the registration as well as the sharpness of the high resolution gray-scale over that of the f-CDI view by sweeping the border back and forth over the suspicious region. Again, click **here** for the movie or follow the link in the caption.

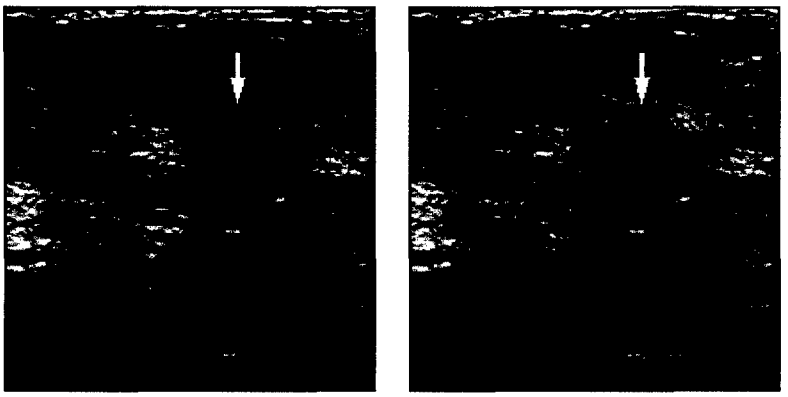

(a) (b)

Figure 3. Lateral-axial scan plane shown in **Figure 2(b)**. In both images, the left of the diagonal line shows the gray-scale from the f-CDI while the lower right shows the high resolution multifocal gray-scale image. **(a)** More of the lower resolution image is shown. Note the alignment of various structures at the diagonal image boundary. **(b)** In this view, more of the high resolution gray-scale is shown. Note the detectability of the spiculated mass (white arrow) just to the right of the diagonal line in the upper portion of the image. In **(a)** this structure is barely discernible. Click either image to view its full sized counterpart. Click **here** for a full Quicktime "wiper" movie (348 kB) containing the frames shown in **(a)** and **(b)**.

Even if the mapping of the two image sets displayed above appears to be very accurate, close inspection of the data reveals a small remaining error in the alignment of discernible landmarks. The main causes of error appear to be

1. Local tissue motion and deformation as caused by respiratory motion and compression of superficial tissue by the transducer itself. These local deformations can be corrected only in part by the global geometric transformation applied here to register the two data sets.
2. Noise in the image sets or any other inherent differences between the sets to be registered as introduced by employing different imaging modes or modalities (here: gray-scale and f-CDI ultrasound).
3. Changes in look direction which cause changes in the apparent brightness of specular reflectors since the echo received from specular reflectors strongly depends an the angle of incidence of the ultrasound pulse. Even if very apparent to the eye, this may actually only be a minor cause of misalignment since the volume covered by specular reflectors is small compared to the total volume, and thus the mutual information affiliated with it contributes little to the maximization of the total mutual information.

The quality of the registration was evaluated by a single observer as described above. The mean alignment error obtained, based on 13 manually defined common landmarks, was 1.1 mm. It should be noted that this value depends on the position and distribution of the selected points throughout the volume and is somewhat subjective. The peak alignment error estimate was 2.9 mm on the left side of the image near the chest wall whose movability is unrelated to the transducer pressure applied.

2. Extended 3-D Field of View Imaging

Figure 4 displays the extended 3-D field of view of an invasive ductal carcinoma scanned in a 65 year old woman. The orientation and relative position of the three scans used to form this extended view was described in **Figure 1**. In this particular example, the central (B) and medial (A) scans overlapped about 75%, the central and lateral (C) scans overlapped 25%, resulting in a total width of the extended field of about 7.9 cm. In **Figure 4**, the boundaries between the displays of the coregistered scans at 0.3 and 0.6 of the total width of the extended view, marked by white arrows in the 2-D view of **Figure 4**, are hardly noticeable. Note that no averaging or other processing (other than slight image compression for on-line display) was employed at the boundaries to smooth out the transition. The display changes abruptly from scan A to B and from B to C, which makes the continuous appearance of the extended view even more remarkable.

A Quicktime **movie** (548 kB) can be displayed for appreciation of the quality of the composite view throughout the volume.

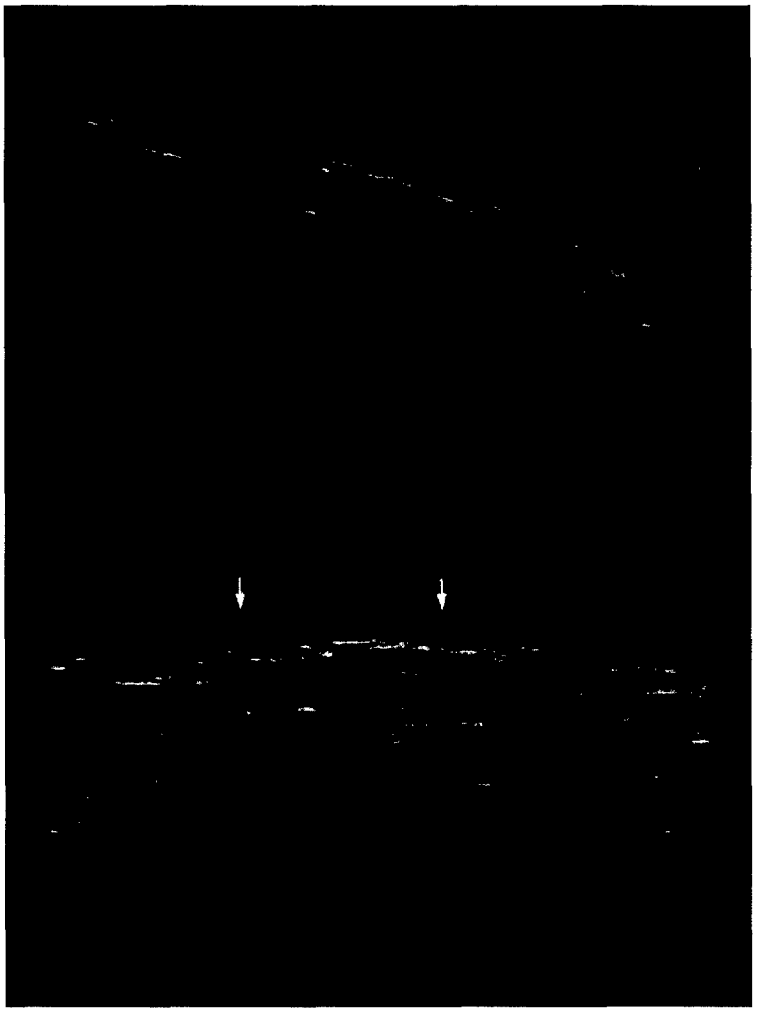

Figure 4. (Top) 3-D view of a volume combined from three parallel, partly overlapping scans in a 65 year old female with invasive ductal carcinoma. (Bottom) 2-D view of the axial-lateral plane displayed in the volume above. The width of this extended view is 7.9 cm. The boundaries between the original scans at about one third and two thirds of the width of the composite image (white arrows) are hardly noticeable. Click **here** for a Quicktime movie (548 kB) displaying an elevational sweep through the extended volume. For a high-quality version of the same movie (1.3 MB), click **here**.

In this example, commercially available high-resolution transducers, with aperture widths of typically four cm, could have only fully displayed one of the masses at a time. This limitation may make the visualization and evaluation of the entire structure using ultrasound more difficult. In the extended view, the three distinct masses are displayed simultaneously in their relative positions as determined by the coregistration in the overlapping regions. This allows immediate perception of the entire region of interest and reveals more of the overall anatomy and anatomical relationships. The large FOV should also diminish the danger of missing important details at the edges and facilitate measurements within the extended volume.

The remaining misalignment of the registered scans in the overlapping regions, based again on visual inspection of identifiable structures and measurement of their apparent shift, was estimated to be 0.8 mm mean (1.5 mm peak) in the 75% overlap region and 1.4 mm mean (3.1 mm peak) in the 25% overlap region.

3. Sequential 3-D Imaging

Figure 5 shows an example of a coregistration of sequential scans of a breast lesion in a patient undergoing CAF chemotherapy. The 65 year old woman had a palpable 2.5 cm mass and was later diagnosed with left invasive ductal carcinoma with a focal mucinous carcinoma component. The two scans displayed here were acquired 8 days before and 29 days after the start of the chemotherapy. Two more scans, obtained and coregistered 55 and 78 days, respectively, after the start of the therapy, yielded similar registration results and are not displayed here.

Although the size and shape of the lesion changed significantly between the first two scans, the registration procedure aligned the lesions well and allows better comparison and visualization of changes than without registration.

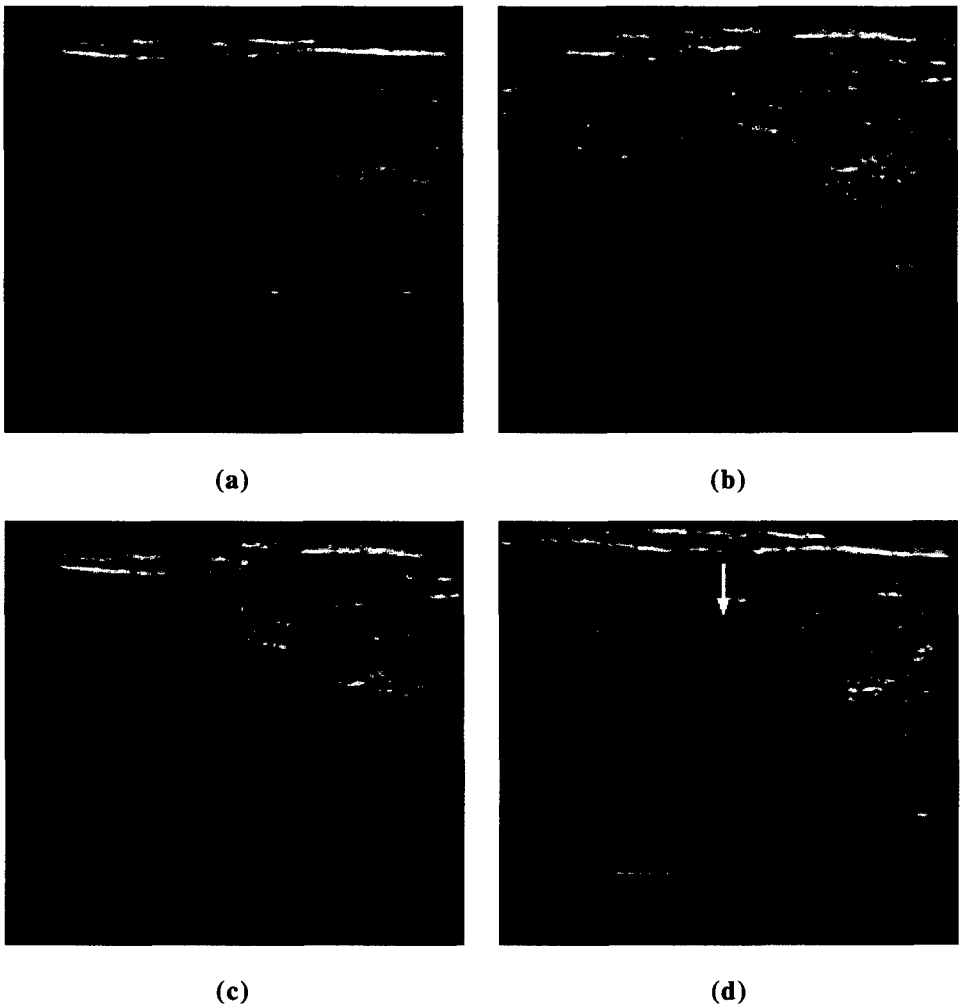

Figure 5. Coregistration of two sequential scans of a breast lesion in a patient undergoing chemotherapy. **(a)** Central B-scan frame of the first scan, obtained one week before the start of the therapy, coregistered and transformed to map onto the second scan. **(b)** Corresponding frame of the second scan, obtained 5 weeks later. **(c)** Combined view of the same frame in the first (left) and second scan (right). Click **here** for a Quicktime "wiper" movie (304 kB) showing the temporal changes throughout this frame by moving the border between the scans from left to right. **(d)** Pseudo-color image of the differences between the two scans, showing increased echogenicity (blue) where the mass shrank (white arrow), and decreased echogenicity (yellow) below the mass (gray arrow). Click **here** for a 292 kB movie displaying the differences throughout the scanned volume.

Figure 5(a) and **(b)** show corresponding frames from the center of the first and second scan, respectively, after coregistration of the volumes. In this case, the first scan was transformed using a full affine transformation to map onto the second one. In a serial study with scans obtained manually and several weeks apart, small changes in look direction or positioning of the transducer are unavoidable even if the sonographer carefully tries to reproduce the field of view of a previous scan. These variations can make direct comparison of two serial scans more difficult. However, if the two scans have enough common information, the registration software can detect these changes and transform one set accordingly. Hence, the slight rotation of the image in **(a)** can be understood as a correction for a small change in view direction between the two scans.

Figure 5(c) shows a combined view of the frames displayed in **(a)** (left half) and **(b)** (right half of the image), which reveals the change in size and other characteristics of the lesion. Also seen is a small error in aligning the specular reflectors at the top of the images, assuming the same tissue planes are producing the specular reflections in the two scans. This near field error is most likely induced by a local deformation of the tissue by the pressure of the transducer against the skin. The estimation of the average misregistration in this serial study is difficult and prone to error because of the additional effect of drug-induced changes over time. These changes cannot be unambiguously separated from the other causes of registration error as discussed above. However, estimating the average error by identification of corresponding landmarks in the two registered sets well outside the tumor volume, a mean error of 1.4 mm (peak 2.2 mm) was obtained.

For better visual evaluation of the registration quality and change in tumor size, a Quicktime movie (304 kB) can be viewed by clicking **here** or on the link in the caption of **Figure 5(c)**. In the movie, the border between the two scans as displayed in **(c)** can

be moved from left to right, thus revealing more of the first or the second scan.

In **Figure 5(d)**, the change in tumor size is highlighted using a pseudo-color display. By simultaneously feeding the gray-scale values of the coregistered first scan into the red and green channels of a RGB (red, green, blue) display and the gray-scale values of the second scan into the blue channel of the same display, a difference image is created with a color map from yellow (echogenicity of first scan larger) through gray (echogenicities identical) to blue (echogenicity of second scan larger). The shrinkage of the hypoechoic mass causes an increase in echogenicity on the mass periphery in the second scan compared to the first. This difference is clearly visible as a blue rim (white arrow) surrounding the proximal half of the mass in **(d)**. The distal part of the mass shows no such blue rim and therefore appears to be unchanged. This may be explained by the surroundning anatomy which can cause asymmetric tissue deformation and displacement around the shrinking mass.

The other prominent feature in this figure is the yellow area immediately below the tumor (gray arrow), indicating an area of decreased echogenicity. This decrease could be explained by a mostly blood-filled mass which has lower attenuation than the surrounding tissue and thus causes an apparent enhancement below the mass. The smaller mass in the second scan then causes less enhancement and therefore a decrease in echogenicity, which can also be seen by comparing **Figures 5(a)** and **(b)**, but which is more obvious in the color display of **(d)**.

By clicking **here** or on the link in the caption of **Figure 5(d)**, a movie (292 kB) can be displayed showing the difference image of **(d)** for 47 frames of the scanned volume. Note the shrinkage of the mass in all 3 dimensions by following the blue rim throughout the movie. Quantitative evaluation of the entire scans using polygons to manually define the border of the lesion in each frame yielded a reduction in lesion volume of approximately 27%.

[Previous: Materials and Methods] [Next: Discussion]

[Title Page | Abstract | Introduction | Materials and Methods |
[Results | Discussion | References]

Discussion

The examples described are successful and significant applications of image registration in 3-D ultrasound. They demonstrate the feasibility of a new technique to improve ultrasound diagnostics and potentially open a new range of related applications.

Routine coregistration and combination of image sets obtained using a variety of different ultrasound modes or using ultrasound and a second imaging modality should be possible with the same or only slightly modified version of the currently used registration software.

In ultrasound multimode imaging, the coregistration should allow image optimization, i.e. replacement of a lower quality component of one image set with the higher quality component of a different set, as in the substitution of high resolution gray-scale data for the lower resolution gray-scale 'background' of color flow imaging modes, as well as image fusion, i.e. the combination of images displaying different physical properties, which increases the diagnostic value of either one of the original images by relating one physical property to another. Possible modes for image fusion can include, but are not restricted to, frequency-shift and power mode Doppler, harmonic imaging, and new modes being researched and developed such as imaging with contrast agents or ultrasound elasticity imaging (27, 28). The quality of the registration will depend on the information content of the images, more specifically, the mutual information. Where only gray-scale information was employed for the registration, the accuracy did not allow an exact pixel by pixel match, but the registration was far better than can be done manually.

In multimodal imaging, coregistrations of ultrasound scans with MR, CT, and other 3-D data sets, or with projection images such as mammograms can be envisioned. If ultrasound scans are obtained in the same or a similar geometry as for a mammogram, a coregistration of a projection of the ultrasound scan with the mammogram could combine the most inexpensive and commonly used modalities for breast imaging. This would add 3-D information to the 2-D mammogram and allow more accurate tracking of spots identified in the mammogram using 3-D ultrasound.

The extended 3-D field of view is a method to overcome one of the major disadvantages of ultrasound imaging compared to most other modalities: the very limited field of view and unsystematic coverage of the region of interest. In breast imaging, a wider field of view should be particularly desirable in following suspicious regions and in detection of preclinical disease. To follow in 3-D the morphology of a large lesion and its effect on the surrounding tissue, a larger field of view will be essential. A combination of extended field of view and multimode (gray-scale and CDI) imaging would even allow tracking of vascular and tissue morphology simultaneously in high quality images. Screening of women at very high risk for breast cancer is beginning to draw more interest in the US with incidental detection of malignant foci at locations removed from the site of suspicion (29). Accordingly, the extended field of view is likely to increase the sensitivity of ultrasound in breast cancer detection. A wider field of view will also help in covering previously scanned sites and thus determining changes over time, either in screening of high risk groups, tracking suspicious regions, or monitoring response to treatment. While radiologists and sonographers can reach very high skill levels, it is often difficult for some operators to assure that the same views are obtained in two or more serial studies. Interpretation is also complicated when the interpreter has not personally performed the exam. Both problems could be reduced using 3-D extended FOV ultrasound imaging.

The accuracy of coregistrations of partly overlapping volumes appears to depend on the size of the overlap. It is possible that the larger the overlap, the more common structure is available to align the scans, and the less the registration algorithm is potentially affected by noise. The minimum overlap required for acceptable registration accuracy can vary with the information content of the data sets. However, in the examples studied so far, a 1 cm (25%) overlap generally produced acceptable registrations, judged by visual inspection.

For serial exams, the extended field of view technique might be combined with coregistration of scans obtained at different times. This would allow the visualization and quantification of changes in large lesions over time. In fact, the acquisition and composition of an extended field of view might prove to be necessary for tracking rapidly changing, large lesions because in this case a small field of view might not contain enough unchanged structure (which is usually found well outside the volume of the mass) for the coregistration to work properly. If routinely used in serial exams of women with high risk of breast cancer, coregistration could help detect early changes not apparent in multiple small FOV scans, thus increasing the chances of effective treatment.

The advantages of image registration in 3-D ultrasound may be more fully employed by using new display techniques such as the difference image shown in **Figure 5(d)**. Using this type of difference image it may be possible to segment regions of shrinkage and growth for rapid, semiautomatic volume change estimations.

For validation of quantitative measurements made in coregistered image sets, an automated error estimation is desirable. The quality of coregistrations can vary strongly with the available mutual information, which depends on the amount of shadowing, specular reflectors, and local tissue deformation present in the image sets. Manual evaluation, as in the examples presented here, may not be practical to assure accuracy of quantitative measurements of dimensions over long distances.

[Previous: Results] [Next: References]

[Title Page | Abstract | Introduction | Materials and Methods]
[Results | Discussion | References]

References

1. Pietrzyk U, Herholz K, Heiss WD. Three-dimensional alignment of functional and morphological tomograms. J Comput Assist Tomogr 1990; 14(1):51-9

2. Alpert NM, Bradshaw JF, Kennedy D, Correia JA. The principal axes transformation--a method for image registration. J Nucl Med 1990; 31(10):1717-22

3. Faber TL, McColl RW, Opperman RM, Corbett JR, Peshock RM. Spatial and temporal registration of cardiac SPECT and MR images: methods and evaluation. Radiology 1991; 179(3):857-61

4. Loats H. CT and SPECT image registration and fusion for spatial localization of metastatic processes using radiolabeled monoclonals. J Nucl Med 1993; 34(3 Suppl):562-6

5. Hill DL, Hawkes DJ, Gleeson MJ, et al. Accurate frameless registration of MR and CT images of the head: applications in planning surgery and radiation therapy. Radiology 1994; 191(2):447-54

6. Ardekani BA, Braun M, Hutton BF, Kanno I, Iida H. A fully automatic multimodality image registration algorithm. J Comput Assist Tomogr 1995; 19(4):615-23

7. West J, Fitzpatrick JM, Wang MY, et al. Comparison and evaluation of retrospective intermodality brain image registration techniques. J Comput Assist Tomogr 1997; 21(4):554-66

8. van Herk M, Bruce A, Kroes AP, Shouman T, Touw A, Lebesque JV. Quantification of organ motion during conformal radiotherapy of the prostate by three dimensional image registration. Int J Radiat Oncol Biol Phys 1995; 33(5):1311-20

9. Andersson JL. How to obtain high-accuracy image registration: application to movement correction of dynamic positron emission tomography data. Eur J Nucl Med 1998; 25(6):575-86

10. Yin FF, Giger ML, Doi K, Vyborny CJ, Schmidt RA. Computerized detection of masses in digital mammograms: automated alignment of breast images and its effect on bilateral-subtraction technique. Med Phys 1994; 21(3):445-52

11. Lehmann T, Sovakar A, Schmitt W, Repges R. A comparison of similarity measures for digital subtraction radiography. Comput Biol Med 1997; 27(2):151-67

12. Leszczynski KW, Loose S, Boyko S. An image registration scheme applied to verification of radiation therapy. Br J Radiol 1998; 71(844):413-26

13. Wilson DL, Carrillo A, Zheng L, Genc A, Duerk JL, Lewin JS. Evaluation of 3D image registration as applied to MR-guided thermal treatment of liver cancer. J Magn Reson Imaging 1998; 8(1):77-84

14. van den Elsen PA, Pol EJD, Viergever MA. Medical Image Matching - A Review with Classification. IEEE Eng Med Biol 1993; 12(1) 26-39

15. Candiani F. The latest in ultrasound: three-dimensional imaging. Part 1. Eur J Radiol 1998; 27 Suppl 2:S179-82

16. Campani R, Bottinelli O, Calliada F, Coscia D. The latest in ultrasound: three-dimensional imaging. Part II. Eur J Radiol 1998; 27 Suppl 2:S183-7

17. Moskalik A, Carson PL, Meyer CR, Fowlkes JB, Rubin JM, Roubidoux MA. Registration of three-dimensional compound ultrasound scans of the breast for refraction and motion correction. Ultrasound Med Biol 1995; 21(6):769-78

18. Meyer CR, LeCarpentier GL, Roubidoux MA, et al. Automated Coregistration of Three-Dimensional Ultrasound Volumes by Mutual Information: Sequential Examples of Breast Masses. (Proceedings of AIUM 42nd Annual Conference, Mar. 22-25) J Ultrasound Med 1998; 17:S1, S87.

19. Meyer CR, Boes JL, Kim B, et al. Semiautomatic Registration of Volumetric Ultrasound Scans. Ultrasound Med Biol (in press).

20. Weng L, Tirumalai AP, Lowery CM, et al. US extended-field-of-view imaging technology. Radiology 1997; 203(3):877-80

21. Kroger K, Massalha K, Dobonici G, Rudofsky G. SieScape: a new sonographic dimension with fictive images. Ultrasound Med Biol 1998; 24(8):1125-9

22. Sivaramakrishna R, Gordon R. Detection of breast cancer at a smaller size can reduce the likelihood of metastatic spread: a quantitative analysis. Acad Radiol 1997; 4(1):8-12

23. LeCarpentier GL, Tridandapani PB, Fowlkes JB, Moskalik AP, Roubidoux MA, Carson PL. Utility of 3D Ultrasound in the Discrimination and Detection of Breast Cancer. Submitted to RSNA Electronic Journal.

24. Maes F, Collignon A, Vandermeulen D, Marchal G, Suetens P. Multimodality image registration by maximization of mutual information. IEEE Trans Med Imaging 1997; 16(2):187-98

25. Kim B, Boes JL, Frey KA, Meyer CR. Mutual information for automated unwarping of rat brain autoradiographs. Neuroimage 1997; 5(1):31-40

26. Meyer CR, Boes JL, Kim B, et al. Demonstration of accuracy and clinical versatility of mutual information for automatic multimodality image fusion using affine and thin plate spline warped geometric deformations. Med Image Anal 1997; 1(3):195-206

27. Shapo BM, Crowe JR, Erkamp R, Emelianov SY, Eberle MJ, O'Donnell M. Strain imaging of coronary arteries with intraluminal ultrasound: experiments on an inhomogeneous phantom. Ultrason Imaging 1996; 18(3):173-91

28. Erkamp RQ, Wiggins P, Skovoroda AR, Emelianov SY, O'Donnell M. Measuring the elastic modulus of small tissue samples. Ultrason Imaging 1998; 20(1):17-28

29. Gordon PB, Goldenberg SL. Malignant breast masses detected only by ultrasound. A retrospective review. Cancer 1995; 76(4):626-30

[Previous: Discussion]

[Title Page | Abstract | Introduction | Materials and Methods]
[Results | Discussion | References]

ELSEVIER

Ultrasound in Med. & Biol., Vol. 24, No. 9, pp. 0000–0000, 1998
Copyright © 1998 World Federation for Ultrasound in Medicine & Biology
Printed in the USA. All rights reserved
0301-5629/98/$–see front matter

PII S0301-5629(98)00148-3

Original Contribution

SEMIAUTOMATIC REGISTRATION OF VOLUMETRIC ULTRASOUND SCANS

CHARLES R. MEYER, JENNIFER L. BOES, BOKLYE KIM, PEYTON H. BLAND, GERALD L. LECARPENTIER, J. BRIAN FOWLKES, MARILYN A. ROUBIDOUX, and PAUL L. CARSON

Department of Radiology, University of Michigan Medical School, Ann Arbor, MI

(*Received 5 May* 1998; *in final form 7 September* 19p8)

Abstract —We demonstrate the ability to register easily and accurately volumetric ultrasound scans without significant data preprocessing or user intervention. Two volumetric ultrasound breast scan data sets were acquired from two different patients with breast cancer. Volumetric scan data were acquired by manually sweeping a linear array transducer mounted on a linear slider with a position encoder. The volumetric data set pairs consisted of color flow and/or power mode Doppler data sets acquired serially on the same patients. A previously described semiautomatic registration method based on maximizing mutual information was used to determine the transform between data sets. The results suggest that, even for the deformable breast, three-dimensional full affine transforms can be sufficient to obtain clinically useful registrations; warping may be necessary for increased registration accuracy. In conclusion, mutual information-based automatic registration as implemented on modern workstations is capable of yielding clinically useful registrations in times <35 min.
© 1998 World Federation for Ultrasound in Medicine & Biology.

Key Words: **Ultrasound, Mutual information, Registration, Volumetric, affine, Thin plate spline warping.**

INTRODUCTION

Fn1

There are potentially many reasons why ultrasound examinations might benefit from registration. Images from different transducer positions are at least partially, if not fully, uncorrelated, and summing them can significantly improve the contrast-to-speckle noise ratio. Doppler color flow acquisitions suffer from undetected flow where the flow is parallel to the transducer's face. Volumes collected from different viewing directions may detect such missing flow vectors, and registration across acquisitions can assist in computing flow velocity vectors that are consistent across different views. Perhaps the most important reason to register ultrasound data sets is to assist the comparison of serial examinations performed on the same patient. Presenting two-dimensional images from different serial examinations with the same orientation and partial volumes may help the clinician more easily to distinguish what has changed. To the extent that echogenicities from different examinations can be approximately equalized, registered serial examinations can be subtracted to emphasize changes. Such differential approaches could be especially important when serially monitoring patient response to chemotherapy or radiation therapy.

Although such automatic registration methods for ultrasound data sets may be desirable, there are preliminary reasons for caution in expecting automatic methods to function well. Such reasons include the ubiquitous speckle noise and attenuation artifacts such as "comet tails" of either shadowing or enhancement. Attenuation artifacts that present differently in each of the data sets depending on transducer orientation may compromise chances of successful registration for any automatic method. An additional source of inconsistent features comes from strong coherent echoes that are observed from structures large with respect to wavelength when observed in an orientation normal to the reflecting surface. Thus, coherent echoes as well as shadows in different data sets are often sources of inconsistent geometry when the data sets were acquired using different transducer orientations. Refraction, i.e., ray bending, may yield additional inconsistencies.

Address correspondence to: Charles R. Meyer, Department of Radiology, University of Michigan Medical School, Ann Arbor, MI 48109-0553, USA. E-mail: cmeyer@umich.edu

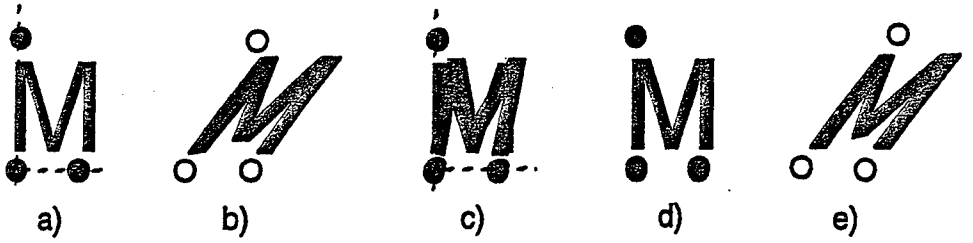

Fig. 1. A simplified two-dimensional example of the registration process is illustrated. (a, b) Two "multimodal" images in which the user has poorly chosen approximate homologous points. (c) Geometric registration that maps the corresponding markers onto each other after the user's initialization, but before automatic optimization begins. After initialization, although the markers are perfectly aligned, the images are still misregistered. (d) Resulting final registration obtained by the optimizer's driving the locations of the homologous points in (b) to minimize the cost function, −I, *i.e.*, maximizing I. Note that the position of the upper marker in (b) has been moved by the optimization process to a new position. (Reproduced with permission from Oxford University Press from Medical Image Analysis 1997;3:195–206.)

The following paragraphs describe the use of a semiautomatic registration technique that appears to be capable of registering ultrasound data sets based on the preliminary information presented herein. The term "semi" qualifies the description of the otherwise totally automatic method because the initial pose between the two data sets must be set by the user. At present, the authors are unaware of any semi- or fully automatic registration algorithms that have been applied successfully to ultrasound data volumes. A recent review of registration techniques in general can be seen in Maintz and Viergever (1998).

METHODS

Volumetric ultrasound data were acquired using a 9-MHz linear array clamped to a linear slide and position encoder on a hand-held frame (Fenn et al. 1997). The transducer manually was swept across the tissue of interest in a direction normal to the linear array's scanning plane. Accuracy of beam position measurement relative to the scan frame was 0.1 mm in the focal plane of the transducer. Data volumes on a uniform Cartesian grid were created by trilinear interpolation between acquired images from known positions.

Pairs of such ultrasonic volumes were registered using a method that requires an initial rough guess of the orientation between the two data sets. As can be seen later in the Results section for the random void phantom, the initial orientation may be far from accurate, but will still within the capture range of the algorithm and result in an accurate registration. The initial, approximate orientation is computed by having the user position a minimum of three corresponding point pairs in each data volume. One of the data sets is chosen by the user as the reference data set, and the other data set, which will be geometrically transformed onto the reference, is referred to as the homologous set. Points in both sets are deposited by clicking the computer's mouse as the cursor is positioned manually over similar-looking, three features. Then, under automatic control of the optimizer, the first three points in just the homologous data set are moved to recompute different geometric orientations of the homologous data set with respect to the reference data set. The points in the homologous data set are referred to as control points, because the geometric orientation between the two data sets is changed to satisfy the homology defined by the control points. The automatic optimizer repeatedly perturbs the loci of the control points in the homologous data set, such that the resulting mutual information, as computed for all voxels in the reference volume and all corresponding voxels in the homologous volume, is maximized to yield the final computed registration model between the two data sets (Collignon et al. 1995; Meyer et al. 1997; Studholme et al. 1997; Viola and Wells 1995; Wells et al. 1996). Figures 1, 2, and 3 help visualize the interplay among the control points, the computation of mutual information, and the recursive optimizer algorithm.

The entropy of a data set is defined as its average information content, whereas joint entropy is the average information of two ordered data sets. The joint entropy H(a,b) of two data sets, a and b, is related to mutual information of both, I(a,b), by the following classic relationship:

$$H(a,b) = H(a) + H(b) - I(a,b) \qquad (1)$$

where H(a) and H(b) are the individual entropies of data sets a and b, respectively (Papoulis 1984). As can be seen in the classic relationship, mutual information I(a,b) is the amount by which the sum of the individual data set entropies must be reduced to account for correlations that

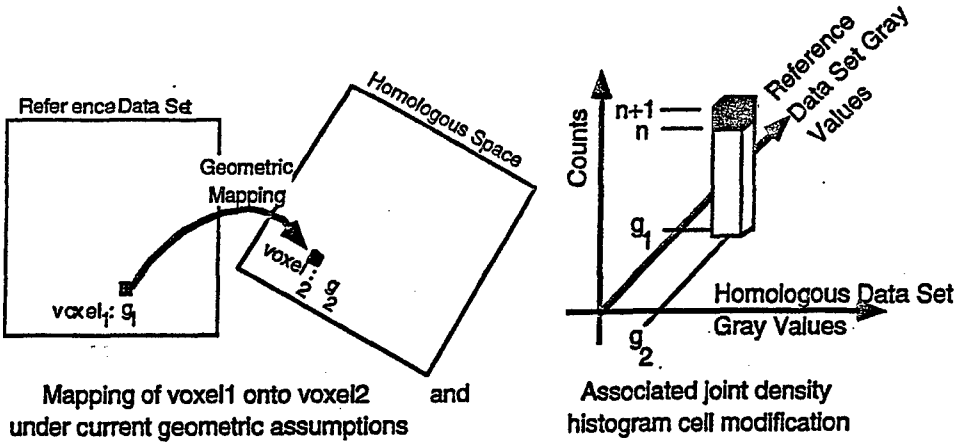

Fig. 2. Two-dimensional joint histogram constructed by raster scanning through all voxels in the reference image set and incrementing bin counts corresponding to the gray-scale values from geometrically mapped voxel pairs under an assumed geometric transformation, which changes with each iteration of the optimizer. (Reproduce with permission from Oxford University Press from Medical Image Analysis 1997;3:195–206.)

exist between the two individual data sets (H and I are non-negative). The previous expression defining mutual information in relation to entropies reduces to the following equation for mutual information in terms of the more fundamental probability density functions for data sets a and b:

$$I(a,b) = \int\int da\, db\, p(a,b) \log(p(a,b)/p(a)p(b)). \quad (2)$$

The initial geometric transform model optimized via moving the initial three control points is the simple, rotate–translate (six degrees of freedom) transform. In a subsequent optimization, the parameters for a full affine (linear, 12 degrees of freedom) transform are estimated via four control points (the three previous plus one new control point positioned automatically into the homologous data set using the previously optimized rotate–translate transform). Finally, if desired, repeated thin plate spline warpings are computed using five or more control points as necessary, where the previous full affine optimum transform is used to instantiate the additional control points. In this manner, the mutual information is optimized at each stage of increasing geometric model complexity, while requiring the user only roughly to estimate approximate geometric homology for the three initial points. The additional control points beyond the first three, which eventually are mapped into the homologous data set, initially are placed in the reference data

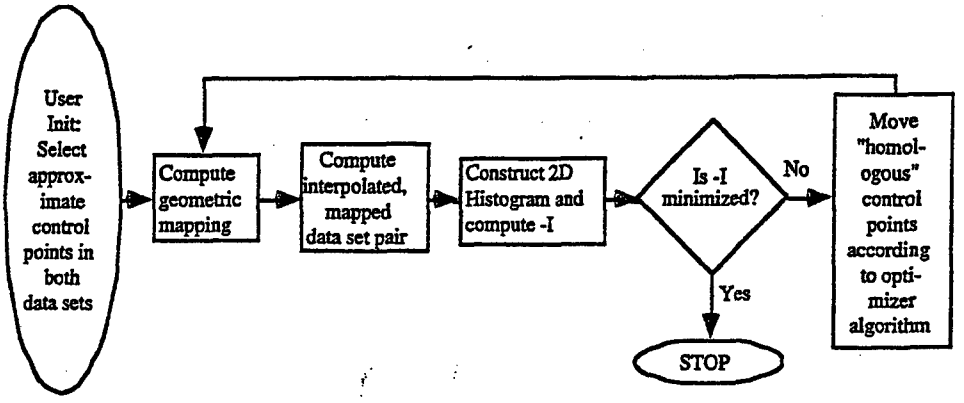

Fig. 3. Functional flow chart of the automatic registration algorithm for one optimization cycle. The process is repeated using the previously computed optimized control point positions as the new starting vector, until the incremental change in mutual information between cycles falls below a user set threshold, typically 0.0002 bits. (Reproduced with permission from Oxford University Press from Medical Image Analysis 1997;3:195–206.)

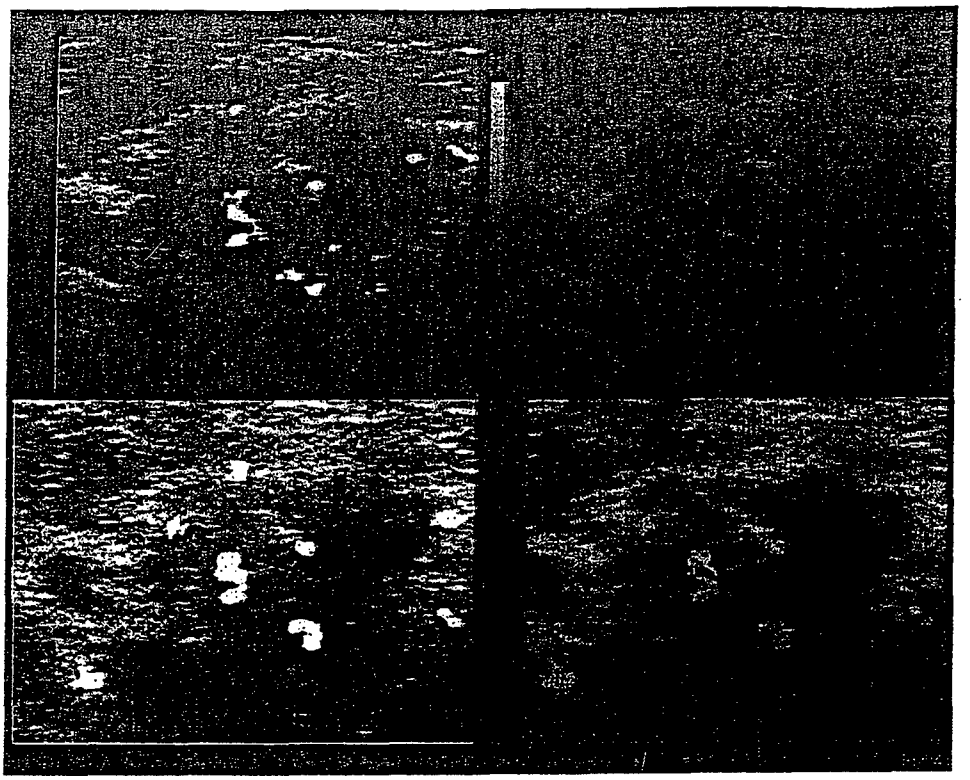

Fig. 4. (a) Image from the red channel of a color flow volume breast examination. (b) Pseudocolored image of (a). Lowest echogenicities are represented by dark blue, intermediate echogenicities by green, and highest echogenicities by bright red hues. Color mapping relationship is explicitly demonstrated in the attached gray-scale and color bars. (c) Power mode data corresponds to same loci as the color flow slice of a following registration. (d) Composite image constructed using "screen door" transparency, where adjacent pixels alternate between the color and gray-scale sources of (b) and (c).

set by the user, without identification of corresponding positions in the homologous data set.

Uniformly sampled data volume sizes are approximately 400 × 350 × 55–100 voxels depending on the manual acquisition; voxel volumes are typically 80 × 80 × 200 μm^3. The registrations computed herein use decimated reference data sets to speed computation. During the initial use of the rotate-translate model, only every fourth voxel in the three major coordinate directions is used in the reference data sets. Each optimization cycle stops when the controller requests control point movements of less than some user chosen criterion, selected here as 0.1 mm, in each coordinate direction. The optimizer is the standard Nelder simplex algorithm, often referred to as "amoeba" (Press et al. 1988). Optimization cycles are repeated until the mutual information increment in the last cycle is less than or equal to another user chosen criterion, selected here and for almost all other modality pairings as 0.0002. After computing the optimal forward transform, which maps the homologous data set onto the reference, the high-resolution mapping of every voxel of the reference data set onto the homologous is computed once, using the inverse transform.

RESULTS

The first registered volumetric data set pair shown in Fig. 4 consists of color flow and power mode Doppler data sets acquired serially during the same patient examination visit. A three-dimensional, nine control point (27 degrees of freedom) thin plate spline warping was computed in 31 min of CPU time on a 200-MHz DEC Alpha workstation, model 3000/500x, using a total of 1552 iterations (where each iteration consists of calculating the geometric transformation, reconstruction of the mapped homologous gray-scale volume, joint histogram, and resulting mutual information) . The red channel of each data set pair was used to compute the geometric mapping. Although radiologists commonly avoid the use of pseudocolored images, such composite images assist in visualizing the results of registration. Display of the registered data sets as shown in Fig. 4d enhances visual differentiation of the individual image sources and facilitates the visual assessment of registration accuracy at all locations in a single image.

Figure 5 allows the reader to assess the accuracy of the volumetric registration over a large volume of sup-

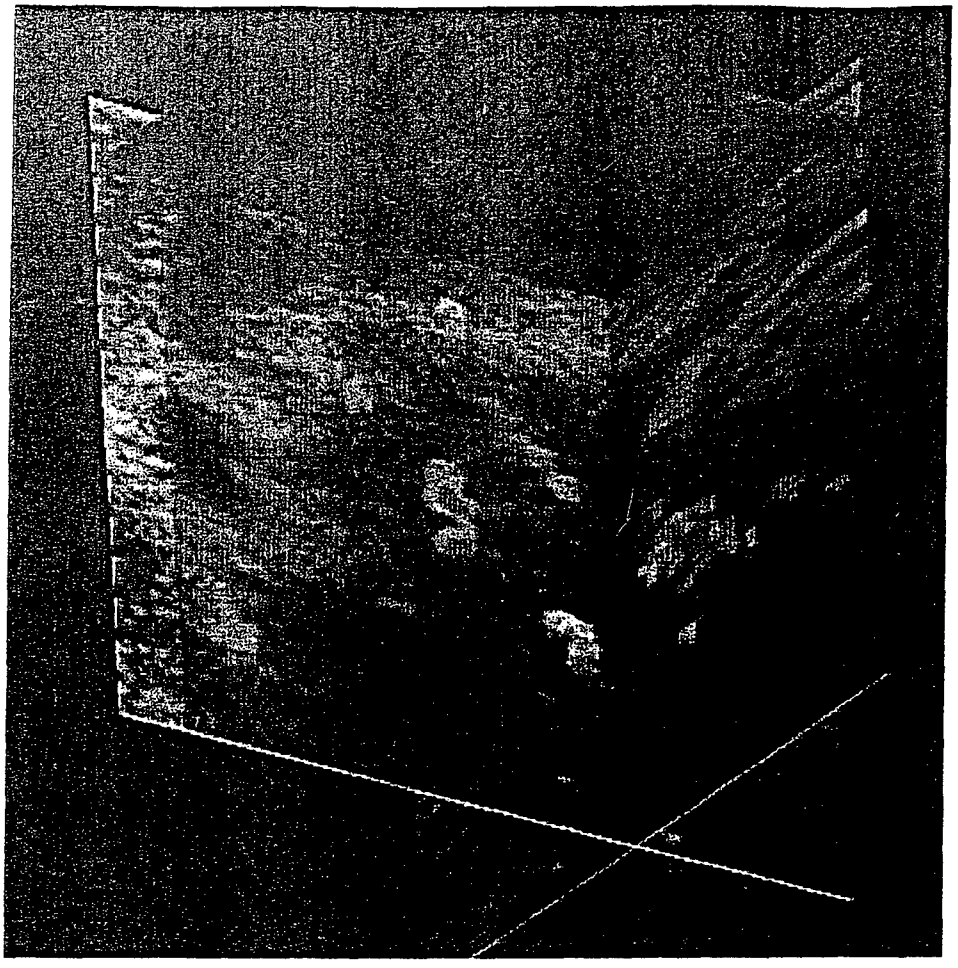

Fig. 5. View of the registered color flow and power mode volumes visualized on three orthogonal, intersecting cut planes using a color composite rendering method that approximates the screen door transparency shown in Fig. 4d. The observer's viewpoint presented here is one of looking back at the transducer from a distal position deep within the breast (top of the image is still patient's anterior). The cut plane whose orientation is nearly perpendicular to the viewer is the same image as that shown in Fig. 4d, where the underlying gray-scale image represents one of the (high resolution) acquisition planes of the color flow data volume. The intersecting cut plane across the top of the volume renders the registration at a constant, shallow depth below the transducer (C-mode), and the remaining cut plane right of center renders a slice of the registered volume below the line traversed by a single transducer element during the manual sweep of the transducer. The color bars that define the pseudocolor conversion for the reference scan is visible on the reader's left.

port. The color composite display computes the relative color contribution to each voxel, based on a linear combination of the intensities of the voxels of the two registered input volumes. The orthogonal cut plane method of display was chosen because of its clarity, intuition, freedom from confusing intervening structures, and the ability simultaneously to display spatially diverse, three-dimensional locations.

F6 Figure 6a demonstrates the effects of the computed geometric warping, by applying the same warping to a rectilinear grid occupying the power mode volume. Figures 6b–6d show views of the deformation from the right, front, and top, respectively. Note that the major component of the geometric transform is a simple affine transformation, as best seen in Fig. 6d, where the volume has been sheered to the left as a function of distance away from the observer, *i.e.*, transducer position. Upon closer inspection, a nonlinear warp can be observed in the front central section of the volume, the same region occupied by the lesion, indicating that, during the second scan, the lesion moved differently than the surrounding tissue.

The second pair of registered volumetric data sets presented here consists of two power mode Doppler data sets acquired on the same patient and separated by 45 d during chemotherapy for locally advanced infiltrating ductal carcinoma. In contrast to the previous case, the registration model's complexity was capped at the level of the full affine (linear, 12 degrees of freedom) trans-

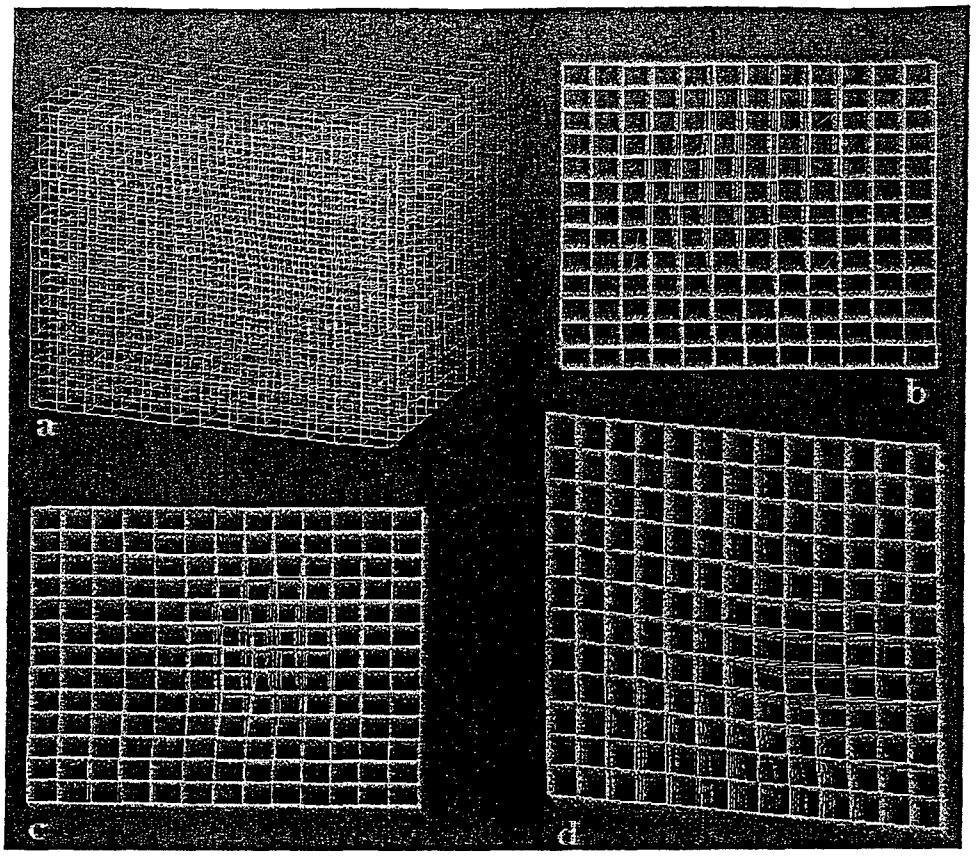

Fig. 6. (a) Computed geometric warp of the power mode volume is demonstrated by applying the same warp to a rectilinear grid occupying the initially undistorted power mode volume. (b, c, d) Views of the warped deformation from the right, front, and top of the scanned volume, respectively.

form due to the resulting excellent overall accuracy, as determined visually. Computing this transform from the initial rough estimate required 909 total iterations over the period of 11.3 min. As in the previous case, the red channel of each pair was used for computing the geometric mapping and display of results. Figure 7a shows three orthogonal cut planes through the registered data set volumes, as visualized from a position above the transducer looking deeper into the scanned volume. Note the shear (most appreciated on the plane nearly perpendicular to the viewer) required to register the data sets. Figure 7b is a single slice of the more recent data set, and Fig. 7c shows the data from the earlier scan corresponding to the geometry of the slice shown in Fig. 7b obtained after volumetric registration. Because the two cases were performed with nearly equivalent depth-gain compensation, equalization of the echogenicities of both scans was trivially achieved using linear gray-scale contrast adjustment. Figure 7d demonstrates the signed difference between the two scans, where the yellow hue represents differences of positive sign, the blue hue represents differences of negative sign, and the intensity for each hue is proportional to the magnitude of the difference. Although some bright, horizontal, linear, coherent structures clearly are represented in the difference image, a lower contrast echogenic structure also is visualized (arrow), *i.e.*, present in the earlier data set but missing in the later volume.

F7

In addition to the two breast data sets presented herein, we include results from scanning a commercially available, random void phantom in two different orientations. The phantom is made by Computerized Imaging Reference Systems, Inc. (Norfolk, VA, USA) and consists of two slabs of randomly placed spherical voids surrounded by a random scattering medium having an attenuation of 0.5 dB cm^{-1} MHz^{-1}. One slab consists of 5-mm diameter voids, and the other consists of 3-mm diameter voids. The two slabs are separated by a voidless slab consisting of the same random scattering medium used to surround the voids in the other slabs. Scattering from the voids averages 14 dB down from the surrounding random scattering medium. Nylon fibers run parallel to the slabs at depth ranges of 2 and 6 cm.

One volumetric scan acquisition was made by manually translating the transducer parallel to the sides of the phantom and, thus, parallel to the wall of spherical voids

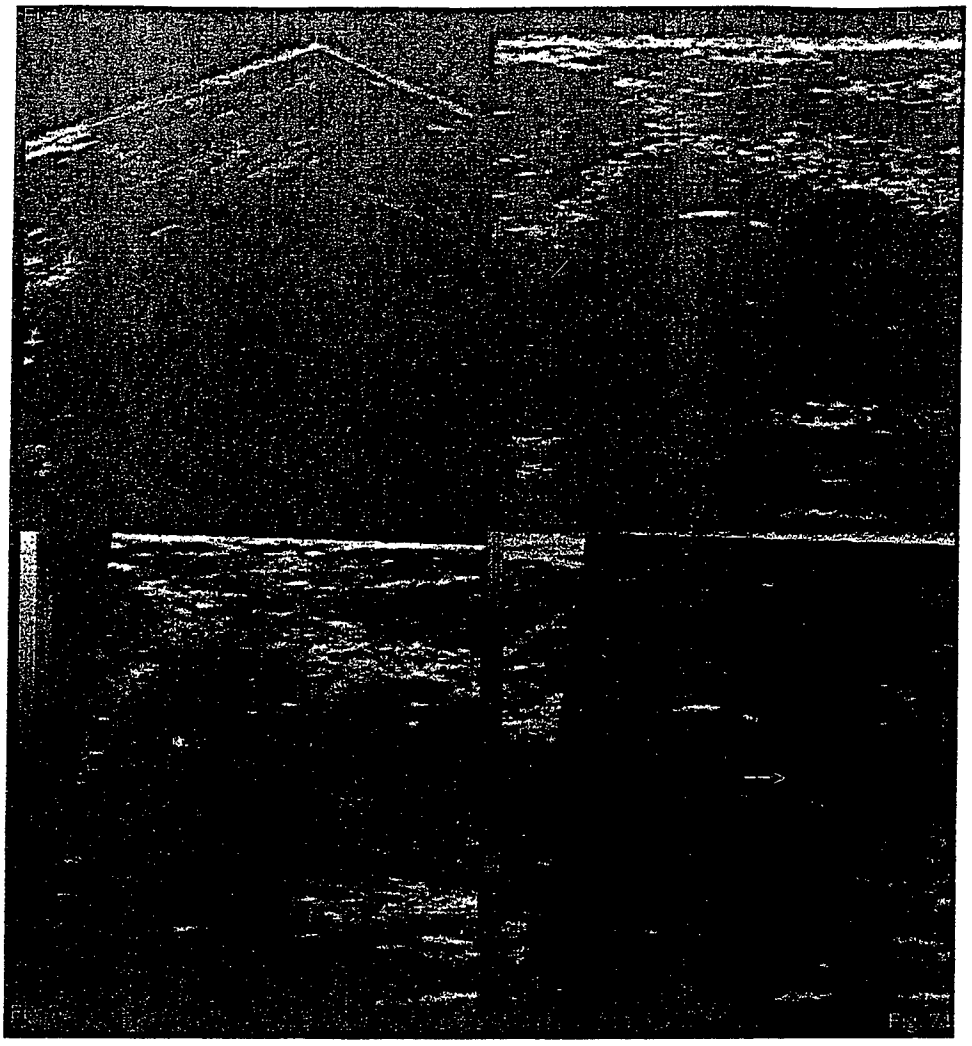

Fig. 7. (a) Orthogonal cut planes through the registered power mode data set volumes from serial examinations visualized from a position above the transducer looking deeper into the scanned volume. The pseudocolored volume was acquired 45 d earlier than the gray-scale volume. (b) Single slice of the more recently acquired data set. (c) Data from the earlier scan corresponding to the geometry of slice (b) after volumetric registration has been implemented; (c) also is visible as the pseudocolored component in (a). (d) Signed difference between (b) and (c), where the two hues represent differences of opposite sign, whereas intensity of each hue is proportional to the magnitude of the difference. In the color bar, a difference of +127 is represented by bright yellow, a difference of zero is black (center of bar), and a difference of −128 is bright blue.

with the transducer held approximately perpendicular to the phantom's surface. The second scan was taken by reorienting the translation path 45° to the initial position using a draftsman's triangle. Thus, in the second scan, the transducer remained approximately perpendicular to the phantom's surface, whereas the path of the translated transducer crossed the wall of voids diagonally. The initial poor placement of the starting markers was intentional, to demonstrate to the reader how severe misregistration of features appears (Fig. 8a) using the display technique shown in Figs. 4 and 5, where blended pseudocolor and gray-scale scans demonstrate the large capture range of the automatic registration algorithm. Note that the bright gray-scale line in the homologous data volume represents the same nylon fiber in the phantom as the red pseudocolor line in the reference volume. The angular misregistration is readily apparent between the two data sets. Note that the voids appear to be filled with higher level scattering, due to the misregistration of the two data volumes.

The results of the final registration are presented in Fig. 8b. The linear nylon fiber in the homologous data set has been superimposed with the red pseudocolored reference data volume fiber. The linear fiber superimposi-

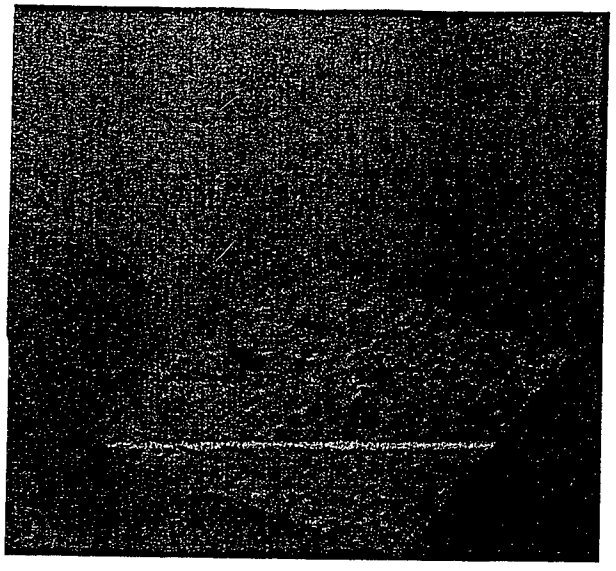

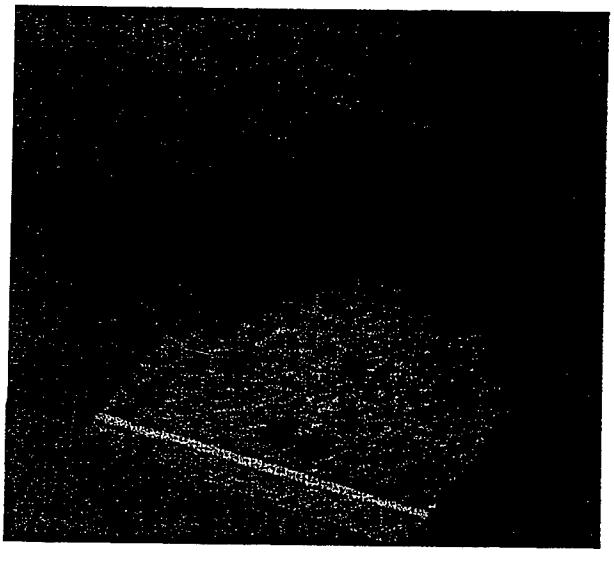

Fig. 8. (a) Initial pose of the 45° diagonal scan of void phantom in gray scale with 0° reference scan in pseudocolor is displayed on three orthogonal planes through data volume. Note the filled appearance of the voids as well as the lack of alignment of the linear nylon fiber in this initially misregistered pose. The reference data set is shown in pseudocolor, with the same color conversion relationship used previously. (b) The same display of reference data set shown in (a) after automatic registration of the volumetric 45° scan with the reference 0° scan. Note that, after registration, the voids have more contrast, because they are not inappropriately filled with misregistered scatterers, and the nylon fiber in the 45° scan is nearly collinear with its position in the reference volume.

tion is nearly perfect to the viewer's right, whereas a slight misregistration can be observed to the viewer's left, as a partial separation of both bright gray and red. This slightly visible error correlates well with the computed angles of $-1.0°$, $-45.4°$, and $-0.5°$ for θ_x, θ_y, and θ_z, respectively, of the rotate-translate approximation to the computed full affine geometric transformation matrix; we would expect 0°, 45.0°, and 0° for a perfect result. The mutual information of the initial pose was 0.064 bits, which was optimized to 0.229 bits in 17 cycles of 1025 total iterations under the rotate-translate geometry model, and finished at 0.383 bits after 16 additional cycles consisting of a total of 1869 iterations, using the full affine geometry model. It is worth noting that simple low-pass filtering of the two data sets significantly speeds the convergence of the registration algorithm, by reducing the grand total of all iterations to 1200, which require total compute times <9 min on a 433-MHz DEC Personal Alpha workstation.

DISCUSSION

Volumetric registration was computed in all cases using a full affine transform as the first endpoint. If the resultant registration was judged by visual inspection to be flawed in local regions, a higher degree of freedom geometry model, *i.e.*, warping, was computed. Thus, the thin plate spline warping of the data set associated with Figs. 1 and 2 was implemented using both a number, *i.e.*, nine, and placement of control points that resulted in a better global solution. The improved accuracy of the registration resulting from warping was determined both visually and quantitatively by the increase in the final, optimized mutual information, *i.e.*, a significant 27% increase in MI was observed from 0.805 for the full affine solution to 0.827 for the nine point TPS solution. The presence of a small mass with different elastic modulus than the surrounding tissue is suggested by observing the nonlinear warping depicted in Fig. 3, because the computed tissue deformation indicates a local rotation. This rotation could have been in response to the overall deformation caused by the pressure of the transducer on the skin in the process of scanning.

For the case of the void phantom, although the error associated with θ_y was <0.5° from the expected value of 45°, the error of 1° in θ_x can be explained by our inability accurately to mount the transducer perpendicular to the plane of the manual translation baffle. Any deviation away from 90° in the angle subtended by the rotation of the autoscanning plane of the transducer into that of the manual scanning baffle, *i.e.*, θ_x, will require compensation by both θ_x and θ_z, depending on the rotation imposed on θ_y. Additional registration accuracies using phantom data from computed tomography, magnetic resonance imaging, and positron emission tomography, are available in Meyer et al. (1997). Although no preprocessing was necessary for the phantom data to obtain accurate registrations, a >50% decrease in registration

time was obtained by low-pass filtering the input data sets before registration. Such behavior should be expected, because low-pass filtering increases the long range correlations in the data sets and smoothes the resulting cost function, such that convergence can be obtained without entrapment by many local maxima.

Because bright, linear structures in the scanned volume occur when the transmitted beam is perpendicular to an echogenic surface, a lack of overlapping alignment of such linear structures is expected, due to the variation in transducer angles used to acquire the different volumes. Conversely, good registration of less intense, incoherent backscattering structures is expected and should be used as an independent visual evaluation tool for qualitatively judging the accuracy of the registration.

The robust behavior of the previously developed mutual information for automatic multimodality image fusion (MIAMI Fuse) registration algorithm (Meyer et al. 1997) for these pairs of same-modality, *i.e.*, ultrasound, data sets was a pleasant surprise. No preprocessing of the data sets, such as speckle reduction, was necessary, and the resulting registrations were of excellent quality and were obtained in relatively short times. Even the demanding task of warping using nine control points, *i.e.*, 27 degrees of freedom, yielded accurate, repeatable registrations, a feat even the authors initially considered as unlikely.

Acknowledgements—This work was supported in part by DHHS PHS NIH grants 2R01CA59412-04, 1R01CA55076, and U.S. Army Contract No. DAMD17-96-C-6061. Assistance in acquiring the scanning data provided by Theresa Tuthill and Stanley Samuel is gratefully acknowledged as well.

REFERENCES

Collignon A, Maes F, Delaere D, et al. Automated multimodality image registration using information theory. In: Viergever MA, ed. Computational imaging and vision, vol. 3. Ile de Berder: Kluwer Academic Publishers, 1995:263–274.

Fenn R, Fowlkes J, Moskalik A, et al. A hand-controlled, 3-D ultrasound guide and measurement system. In: Lees S, ed. Acoustical imaging, vol. 22. New York: Plenum Press, 1997.

Maintz J, Viergever M. A survey of medical image registration. Med Image Anal 1998;2:1–36.

Meyer CR, Boes JL, Kim B, et al. Demonstration of accuracy and clinical versatility of mutual information for automatic multimodality image fusion using affine and thin plate spline warped geometric deformations. Med Image Anal 1997;3:195–206.

Papoulis A. Probability, random variables, and stochastic processes. New York: McGraw-Hill, Inc., 1984.

Press WH, Flannery BP, Teukolsky SA, Vetterling WT. Numerical recipes in C: The art of scientific computing. Cambridge: Cambridge University Press, 1988.

Studholme C, Hill DLG, Hawkes DJ. Automated 3D registration of MR and PET brain images of the head by multiresolution optimization of voxel similarity measures. Med Phys 1997;24:25–35.

Viola P, Wells WM. Alignment by maximization of mutual information. 5th Int'l. Conf. on Computer Vision, vol. 95CH35744, IEEE, MIT, 1995:16–23.

Wells W, Viola P, Atsumi H, Hakajima S, Kikinis R. Multimodal volume registration by maximization of mutual information. Med Image Anal 1996;1:35–51.

AQ: 3

Our reference: UMB 5398

ELSEVIER SCIENCE INC.
TRANSFER OF COPYRIGHT AGREEMENT

Scientific publishers and authors share a common interest in the protection of copyright: authors principally because they want their creative works to be protected from plagiarism and other unlawful uses, publishers because they need to protect their work and investment in the production, marketing and distribution of the article written by the author. In order to do so effectively, publishers need a formal written transfer of copyright from the author(s) for each article published. Publishers and authors are also concerned that the integrity of an article (once refereed and accepted for publication) be maintained, and in order to protect that reference value and validation process, we ask that authors recognize that distribution (including through the Internet/WWW or other on-line means) of the version of the article as accepted for publication is best administered by the publisher. Please complete and return this form promptly.

Article entitled: Semiautomatic registration of volumetric ultrasound scans

Author(s): Dr. C.R. Meyer

To be published in the journal: Ultrasound in Medicine & Biology

Effective upon acceptance for publication, copyright (including all rights thereunder and the right to obtain copyright registration in the name of the publisher, whether separately or as a part of a journal issue or otherwise) in the above article and any modifications of it by the author(s) is hereby transferred throughout the world and for the full term and all extensions and renewals thereof, to:
World Federation for Ultrasound in Medicine and Biology

This transfer includes the right to adapt the article for use in conjunction with computer systems and programs, including reproduction or publication in machine-readable form and incorporation in retrieval systems.

Rights of authors

Elsevier Science Inc. and World Federation for Ultrasound in Medicine and Biology

recognizes the retention of the following rights by the author(s):

1. Patent and trademark rights and rights to any process or procedure described in the article.

2. The right to photocopy or make single electronic copies of the article for their own personal use, including for their own classroom use, or for the personal use of colleagues, provided the copies are not offered for sale and are not distributed in a systematic way outside of their employing institution (e.g. via an e-mail list or public file server). Posting of the article on a secure network (not accessible to the public) within the author's institution is permitted. However, if a prior version of this work (normally a preprint) has been posted to an electronic public server, the author(s) agree not to update and/or replace this prior version on the server in order to make it identical in content to the final published version, and further that posting of the article as published on a public server can only be done with Elsevier's written permission.

3. The right, subsequent to publication, to use the article or any part thereof free of charge in a printed compilation of works of their own, such as collected writings or lecture notes, in a thesis, or to expand the article into book-length form for publication

Note

All copies, paper or electronic, or other use of the information must include an indication of the Elsevier Science Inc. and World Federation for Ultrasound in Medicine and Biology

copyright and a full citation of the journal source. *Please refer requests for all uses not included above, including the authorization of third parties to reproduce or otherwise use all or part of the article (including figures and tables), to*

Elsevier Science, Rights & Permissions Department, P.O. Box 800, Oxford, OX5 1DX, UK

Jonathan M. Rubin, MD, PhD • Ronald O. Bude, MD • J. Brian Fowlkes, PhD
R. Steven Spratt, PhD • Paul L. Carson, PhD • Ronald S. Adler, PhD, MD

Normalizing Fractional Moving Blood Volume Estimates with Power Doppler US: Defining a Stable Intravascular Point with the Cumulative Power Distribution Function[1]

PURPOSE: To normalize the power Doppler ultrasound (US) signal to the expected signal from 100% blood in the calculation of a fractional moving blood volume estimate.

MATERIALS AND METHODS: To locate the signal from flowing blood with a consistent backscatter coefficient, the authors estimated the knee of the cumulative Doppler power distribution function. They used a flow-tube phantom to test the use of this knee to locate a radial position that would fall into a region of high shear stress and minimal rouleaux formation. They also studied how well the method normalized fractional moving blood volume estimates of the right renal cortex in a volunteer when simulating different body habitus and in a group of six healthy volunteers to estimate variability.

RESULTS: Over five flow velocities and over undersaturated to severely oversaturated receiver gains, the calculated flow-tube area was a mean 89% ± 7 (± standard deviation) of a standard. In humans, the technique normalized the fractional moving blood volume estimates over an 8-dB receiver gain variation; the mean ± standard deviation of fractional moving blood volume estimates for the six volunteers was 37.6% ± 3.6.

CONCLUSION: Vascularity estimates with power Doppler US are feasible with a normalization scheme based on the cumulative Doppler power distribution function.

ALTHOUGH of substantial interest, ultrasound (US) Doppler vascularity measurements have been used on a variable basis in several organ systems (1–4). They have generally, but not exclusively, been based on the counting of color pixels in standard color Doppler US scans and have been used clinically most frequently to assess tumor vascularity in the breast and prostate (5–13). The choice of these organs is informative, because it reveals one of the greatest shortcomings of US vascularity assessments: their depth dependence. In all of the examples in which quantitation has been used, either the target is superficial or the transducer has been positioned very closely to the area of interest. This is because vascularity is assessed by counting the number of color pixels in a given region, and anything that alters color pixel count will affect a vascularity assessment. Unfortunately, the density of blood vessels, the quantity one wishes to measure, is only one of the factors that influences the color pixel count. Major contributors to this measurement are attenuation, aperture size, or any other property that alters the strength of the backscattered echoes. Given identical tissue samples, their vascularity at US will change the deeper in the body they are located. The closer a tissue is to the transducer, the more vascular it will appear. For example, flow in ovaries may be very hard to detect transabdominally and yet very easily seen transvaginally. The vascularity detection improvement is due primarily to a reduced attenuation path in the latter, which yields some combination of higher signal and which allows the use of higher frequency transducers (14). Because of this very definite attenuation effect, vascularity measurements with US are tricky to make and interpret.

A potential solution to this problem does exist. If one can identify an object of known vascularity or blood volume, one can use the Doppler power in that object to normalize the values in the surrounding tissue (15–17). If the tissues of interest are near enough to the known object, the fraction of the Doppler power in the surrounding tissue relative to the standard can be used as a vascularity estimate. This process effectively compensates for any attenuation or transducer beam profile effects. Because blood vessels contain 100% blood, objects of known vascularity exist throughout the body and could be used to normalize vascularity measurements. We will call such measurements fractional moving blood volume estimates (17).

There is one problem, however, that has to be overcome before this method can be applied. The problem arises because the backscattered signal from blood is variable owing mostly to the degree of rouleaux formation (18–22). The reason for this is that rouleaux

Index terms: Blood, flow dynamics, 9*.12983[2] • Blood vessels, US, 9*.12983 • Ultrasound (US), power Doppler studies, 9*.12983 • Ultrasound (US), technology, 9*.12983

Radiology 1997; 205:757–765

[1] From the Department of Radiology, University of Michigan Hospitals, 1500 E Medical Center Dr, Ann Arbor, MI 48109 (J.M.R., R.O.B., J.B.F., P.L.C., R.S.A.); and Diasonics, Santa Clara, Calif (R.S.S.).
Received May 19, 1997; revision requested July 8; revision received August 12; accepted August 13. Supported in part by a grant from Diasonics, U.S. Public Health Service grant RO1CA55076 from the National Cancer Institute, and the U.S. Army Medical Research Materiel Command contract DAMD17-94-J-4144. Address reprint requests to J.M.R.

[2] 9* indicates vascular system, location unspecified.

© RSNA, 1997

effectively increases the size of the scattering units in blood. Clumps of red blood cells will backscatter more ultrasound energy than will individual cells, which makes areas of vessels with more rouleaux have stronger Doppler signals than those with less. This effect is most pronounced when comparing the Doppler power in the center of large blood vessels with the Doppler power in the edges. There is typically much more signal amplitude in the center of the vessels owing to increased rouleaux formation (23). The higher shear rate and shear stress near the vessel wall apply more force to separate rouleaux clumps of red cells. The magnitude of the shear rate, which is directly proportional to the shear stress, depends on the velocity profile (24). For a parabolic flow profile, the shear rate and, thus, the shear stress are directly proportional to the radius (20). Hence, for a 1-cm-diameter vessel, the shear rate at the wall will be 10 times that 0.5 mm from the center of the vessel. For near plug flow, the shear rate at the wall can be arbitrarily high. Because of this variation in the appearance of blood flow, one cannot just identify a blood vessel, obtain a normalization value, and calculate a fractional moving blood volume estimate at a given depth. A more sophisticated technique is required.

It is known that smaller vessels have greater shear than do larger vessels for a given mean velocity (25). Because we would like to normalize vascularity by the power that corresponds to 100% blood in tissue, where the blood vessels are small, a value outside the region of high rouleaux would be appropriate. Because of a condition of no slippage at the wall or boundary, there is no flow immediately adjacent to the wall of a vessel. Hence, the "correct" normalizing value lies somewhere between the high value in the center of a vessel and the zero value at the wall.

To perform a fractional moving blood volume estimate, we first calculate a cumulative Doppler power distribution function over the region of interest (see below). We then identify the knee of the cumulative Doppler power distribution function. This knee is used in an algorithm to define a boundary point within highly vascular areas in which we will search for a normalization value. The knee of this distribution is a reasonable choice for segmenting a population into two groups, which is similar to what is done in segmenting populations in receiver operating characteristic analysis (26,27). Once the normalization value is measured, we use that value to determine the fractional moving blood volume estimate in tissue.

We performed this study to normalize the power Doppler US signal to the expected signal from 100% blood in the calculation of a fractional moving blood volume estimate. We used this technique to compensate for depth, attenuation, receiver gain, and machine variability. Ultimately, we believe that the results strongly suggest that this technique could be generally used to assess vascularity in tissues.

MATERIALS AND METHODS

Definition

The cumulative Doppler power distribution function is the integral of the histogram of the Doppler powers within a region of interest (28). It is defined in a discrete sense as

$$N(p) = \sum_{i=0}^{i=p} n(i),$$

where $n(i)$ is the number of pixels with the ith power value and $N(p)$ is the total number of pixels with power values less than or equal to p; that is, $i \leq p$. Because this is an integral of the histogram, the cumulative Doppler power distribution function has some nice random noise–suppressing properties that make it an interesting candidate for finding a normalization value. In a cumulative distribution, fluctuations are referenced to the entire display range, whereas with a standard histogram, being the derivative of the cumulative distribution, fluctuations are seen relative to locally changing values for which any variation is a much larger percentage.

Phantom Studies

We designed a flow-tube experiment to evaluate the boundary-detection properties of the cumulative Doppler power distribution function. The tube consisted of an elongated balloon of 5.5 mm in diameter in a fluid bath. The balloon was draped across a sound-absorbing pad to suppress reverberations. Flow in the balloon was generated by using a pulsatile pump (Harvard Apparatus, South Natick, Mass) with a 70% duty cycle and 50 strokes per minute. Before reaching the balloon, the fluid passed through a long segment of compliant gum rubber tubing that made the flow nonpulsatile. Degassed water that contained corn starch particles (0.5 g per liter of water) as scatterers was run through the balloon. To simulate real flow-containing tissue, we put cross-linked dextran beads (Sephadex particles; Sigma Chemical, St Louis, Mo; 20–80 μm diameter at concentrations of 0.0373–0.2372 g/L, depending on the background Doppler power level) into the bath outside the balloon. By stirring the bath, we could introduce a Doppler shift in the medium and generate Doppler power in the background similar to the effect of tissue that contains flowing blood. The quantities of cross-linked dextran beads and corn starch were selected so that the tube always visually had more power than the water bath at each flow setting, thus simulating a vessel surrounded by flowing blood within perfused tissue. We made three measurements at each flow rate investigated (Table 1). These three measurements were made with low gain to simulate a weak signal deep in tissue, optimal gain (see below) to simulate tissue that was superficial enough or vascular enough to supply sufficient signal, and high gain in which the signal in the tube was saturated to simulate bad technique or the presence of contrast agents.

Table 1
Raw Data from the 15 Flow Experiments

Run	Mean Flow Velocity (cm/sec)	Pulse Repetition Frequency (Hz)	Receiver Gain Setting (dB)	Fractional Area*
1	17	1,250	79	0.849
2	17	1,250	86	0.972
3	17	1,250	92	0.875
4	35	2,250	80	0.941
5	35	2,250	85	0.893
6	35	2,250	90	1.03
7	51	2,750	84	0.894
8	51	2,750	89	0.889
9	51	2,750	94	0.93
10	60	3,500	84	0.704
11	60	3,500	89	0.917
12	60	3,500	94	0.885
13	79	4,500	84	0.903
14	79	4,500	89	0.897
15	79	4,500	94	0.886

*Fractional area is the area of the tube calculated by using the knee of the cumulative distribution over the image divided by the area subjectively determined by tracing the outline of the tube.

To define the gain settings for the flow-tube measurements in testing the cumulative Doppler power distribution function algorithm, we had to define what low gain, optimal gain, and high gain would be. We used VST US scanners (Diasonics, Santa Clara, Calif) to make the measurements. We used a 10-MHz linear-array transducer (Diasonics) with a 6.0-MHz Doppler frequency. The angle of the scanhead to the tube was 22° to generate a Doppler angle. We measured signal strength and saturation level by assigning a green-tag value to Doppler power measurements. Each green-tag step defined by the manufacturer corresponded to 0.4 dB. We set the saturation level such that the highest green-tagged pixels in the flow tube were within three click steps of the highest decibel level, 24 dB. This corresponded to having the highest pixel values in the flow tube be no more than 23.2 dB on the 24-dB scale, which represents the

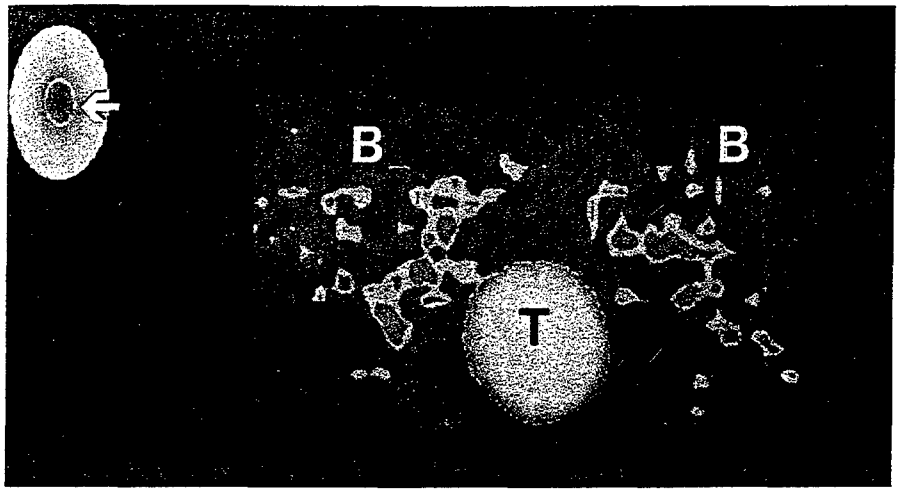

Figure 1. Cross-sectional US image of corn-starch–containing flow tube (*T*) in a water bath (*B*) that contains cross-linked dextran beads. The water bath was manually stirred to generate a Doppler signal, represented in yellow, and simulated viable, blood-perfused tissue. The tube, which represents a blood vessel, corresponds to 100% blood and, hence, has more Doppler power than the water bath, which simulates less vascular tissue. This is demonstrated as a tube brighter than the water bath in power mode. The outer margin of the blue outline of the flow tube marks the boundary of the tube, as calculated by using the automated boundary detector. The blue line is actually thicker than the true boundary threshold for purposes of display. The blue pixels equal the set of all pixels in the image, such that threshold ≤ pixel value ≤ threshold + 0.9 dB. Note that there are regions in the water bath that also either are surrounded by blue or are blue. These correspond to potential areas of 100% blood in tissue. The black area behind the tube and water bath is the top of the sound-absorbing rubber pad. Also note that there is a blue ring in the color wheel in the upper left-hand corner (arrow). The area of the wheel that is located between the blue ring and the outer edge represents the portion of the entire power dynamic range that is assigned to 100% blood in this particular trial.

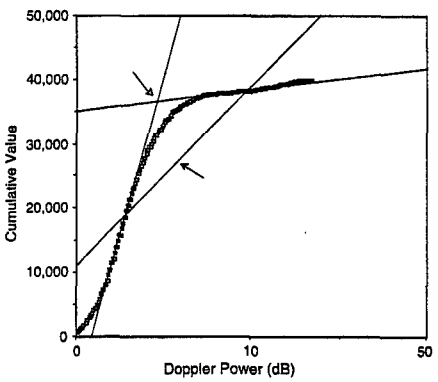

Figure 2. Cumulative distribution for one of the phantom flow experiments. The plot shows the three best-fit lines used in the two-tangent technique. The global best-fit line (solid arrow) intersects the distribution at two points. A tangent line is defined at each intersection point, and the intersection of the tangents (open arrow) defines the position of the knee. This technique clearly underestimates the position of the knee. This particular plot was for one of the undersaturated experiments, which is why it does not extend to 24 dB.

dynamic range of the power-mode signal. When the Doppler gain was set such that the pixels with the highest power in the image fell into this range, the settings were considered optimally saturated. We then set the saturation limit in a range that was clearly undersaturated (5–7 dB), below the optimally saturated setting, and finally set a range in which the Doppler power in the tube was clearly oversaturated (5–7 dB above optimal saturation). A representative image from each flow run was stored digitally to the hard disk on the scanner and transferred to an image analysis program (AVS; Advanced Visual Systems, Waltham, Mass) for analysis.

The boundary of 100% blood as seen with the ultrasound beam in the flow tube was identified by using a cumulative distribution based on the entire data set and was compared to an observer-traced perimeter of the tube, which was considered the standard of reference (Fig 1). To define the region over which the cumulative distribution was taken, an observer first traced the entire area of the stored image of the tube and the water bath, with the exclusion of the sound-absorbing rubber pad. The pad was excluded because, having no "flow," it would bias the measurement by introducing a structure that was much different from the paradigm of interest, that is, blood vessels and background tissue with flow. A cumulative distribution was calculated on the basis of the power values within this enclosed region. The knee or point of maximum curvature of the distribution was then subjectively selected on the cumulative distribution curve for each flow measurement. We used the visual estimate of the knee of the distribution for this calculation because it was deemed to be the best estimator of that point. To compensate for variability, we selected a range of about ±1 dB about the selected threshold and calculated the areas within these limits. Of course, this method of detecting the threshold would not work in practice; therefore, we developed techniques for automating the location of the knee (see below). For this part of the study, however, it was thought that our best estimate of the knee, the visual estimate, was the most appropriate to use.

An observer then traced the tube as a standard of reference for comparison with the cumulative distribution-selected boundary. The tube was traced three times at each flow setting, the area calculated with each traced perimeter, and a mean area calculated for the tube. The mean areas for the cumulative distribution–detected region and for the manually traced region were then compared.

Automated Distribution Determination

To implement a fractional blood volume measurement in vivo and to make more objective measurements, we wanted to use automation to calculate the position of the knee of the distribution. We used two techniques, each of which was initiated in the same way. A best-fit line was first plotted through the distribution by using a standard least-squares technique. For the first technique, the points of intersection of the line with the distribution were located, and tangent lines parallel to the cumulative distribution curve were drawn at the points of intersection. The intersection of these two tangent lines defined the knee of the cumulative distribution. The points of intersection were determined by taking the difference between the cumulative distribution value and the calculated estimate, which was accomplished by using the best-fit line for each successive power value. For those points at which the sign of the difference changes, there must be an intersection between the best-fit line and the distribution between that point and its neighbor, either one of which could be defined as the intersection for the purposes defined here. The tangent lines were empirically defined over 21 point regions, the intersection point ± 10 points (Fig 2). (Further details are in the Appendix.)

The second method begins as the first, with fitting of the cumulative distribution with a best-fit straight line. The distribution is then rotated about the best-fit line so that the line falls onto the abscissa. On the basis of the shape of the cumulative distribution, this function should have a negative curvature and there should therefore be a global maximum. A global maximum could then easily be identified and corresponded to the knee. To account for noise about the global maximum, a region of ±10 points around this initially identified global maximum was selected and fitted with a second-order polynomial. The power value that corresponds to the peak of this polynomial could also represent the knee of the distribution. Although not identical, this technique is similar to other methods in which second-order polynomials are used to search for maxima (29).

The tangent method and then the curve-fitting method, that is, the initial rotated peak and then the second-order polynomi-

al–fitted peak, were then each compared to the subjective standard of reference for finding the knees of the cumulative distributions for the tube-flow data by taking a mean absolute difference between the measurements.

Human Studies

The human studies were divided into two phases. The first consisted of the acquisition of multiple scans in one healthy volunteer at different gain settings to simulate different body habitus, while the second consisted of the acquisition of multiple scans in six healthy volunteers to investigate variability.

In the first phase, the right kidney of a single healthy male volunteer (age, 49 years; weight, 76 kg; height, 173 cm) was scanned on five different occasions. The studies were performed by using a 3.5-MHz curved linear scanhead with a pulse repetition frequency of 1,000, a color Doppler frequency of 2.5 MHz, and an ensemble length of 10. The receiver gain was successively increased from 102 dB to 112 dB in 2-dB steps. Over this range, the images clearly progressed from highly undersaturated to highly oversaturated. This manifested as a lack of flow detection at the 102-dB setting and as a very bright ballooned color display at the 112-dB setting. Again, this range was used to simulate scanning a deep structure without the use of contrast agents. The typical optimal setting for power Doppler, that is, when the noise floor just begins to break through the uniform color background (29), was at about 105–107 dB . During each sampling, the kidney was scanned longitudinally at each gain setting by using a region of interest defined by the machine's color box that included as much of the near-field cortex of the kidney as possible and at least half of the renal sinus. Because of the curvilinear shape of the color box implemented with this probe, some liver and perinephric fat were also included in the region of interest. The image of the cortex chosen for analysis at any given scanning setting was the one that subjectively had the most visible blood flow. The first cumulative distribution was taken over the entire color box, and the knee of the distribution was automatically calculated with both the tangent and the curve-fitting techniques described above. A green tag was assigned to all power values equal to or greater than the value identified as the knee of the distribution. The technique that helped identify a knee that resulted in assigning the greatest fraction of the color dynamic range to potentially 100% blood, that is, that resulted in green tagging of the most pixels, was then used in the next stage of the algorithm.

A second cumulative distribution was then taken over only those points selected in the first run. The knee of this second distribution was then identified by using the two techniques described above, and the value that assigned the largest fraction of the dynamic range to green was again used as the normalization value. This value became the normalization value for the fractional moving blood volume estimation, or, equivalently, the lowest Doppler power that corresponded to 100% blood. This process is demonstrated in Figure 3.

A region of cortex in which the fractional moving blood volume was to be estimated was then traced within the color box by using the machine's tracker ball. Other than the selection of the size and location of the color box itself, this was the only portion of the examination in which there was operator interaction. A fractional moving blood volume estimate was calculated from this region. The means and standard deviations of the selected initial green-tag level were plotted as a function of receiver gain to show the effect of attenuation and, potentially, body habitus on the normalization level. Further, a mean value and a standard deviation of the fractional moving blood volume estimate as a function of receiver gain were plotted over the five measurements.

The second phase comprised examinations of six healthy volunteers (one man, five women; mean age ± standard deviation, 34 years ± 6 years; age range, 27–41 years; mean weight, 78 kg ± 22; weight range, 57–116 kg; mean height, 173 cm ± 11; height range, 160–188 cm) by one examiner (J.M.R.). Each volunteer underwent scanning on 3 different days without preparation, for purposes of practicality. The volunteers were examined by using the same machines described above, with optimization of the setting for power Doppler in the usual manner, that is, the gain was increased sequentially until the noise floor just broke through the uniform background (30). Once the receiver gain was set, the same process for determining the fractional moving blood volume estimate in the single volunteer was used. The means and standard deviations for the fractional moving blood volume estimates for each of the volunteers were plotted.

RESULTS

Flow Experiment

The experimental flow runs are given in Table 1. The area of the tube detected by using the knee of the cumulative distribution was 89% ± 7 of the subjective boundary. It must be said that at the highly saturated settings, the difference between the boundary and the background scatterers in the medium was hard to see, and the knee of the distribution was often thought to be a better marker of the boundary than the standard of reference. Furthermore, it is obvious that there was blooming of the flow tube with increasing gain, which made the detected boundary move outward. This corresponded to a larger tube area for any given velocity (Table 1) and is to be expected with higher levels of saturation. This would manifest in vivo as enlargement of blood vessels with increasing gain.

We then compared the different knee-detecting techniques to see how well they identified the knee compared with the subjectively chosen location (Table 2). It is clear that the tangent method underestimates the subjectively designated position of the knee, thereby assigning more power values to 100% blood. The mean absolute difference between the two tangents and the knee was 0.91 dB. The second-order polynomial–fitting technique more closely approximated the subjectively selected knee: 0.33 dB for the peak value and 0.30 dB for the second-order polynomial–fitted peak.

Human Studies

The segmentation values of vascular structures from the less vascular background were plotted as a function of receiver gain (Fig 4). The plot shows a monotonic decline in the normalization level as a function of receiver gain. The slope is significantly different from zero (95% confidence interval: −0.996, −0.694). This result is what would be expected if the knee of the cumulative distribution were compensating for overlying attenuation and depth of the organ, that is, body habitus. The weaker the flow signal in general, the greater the portion of the dynamic range that may be assigned to 100% blood. Furthermore, despite this change in normalization level with gain, the ultimate fractional moving blood volume estimate is largely independent of receiver gain (Fig 5). This is based on taking a linear regression and determining the slope over the 8-dB highest dynamic range measurements, 104–112 dB, which is 0.00624 (95% confidence interval: −0.00067, 0.01315). Thus, zero is included in the 95% confidence limits. The addition of the lowest dynamic range measurement, 102 dB, produces a significant positive trend in the data, with a slope of 0.00798 (95% confidence interval: 0.00198, 0.01400). Finally, scans obtained in the six volunteers show the means ± standard deviations of the fractional moving blood volume estimates one might expect with this technique (Fig 6). The standard deviation for any single individual can be up to ±0.1. This corresponds to approximately a 30% variation relative to the mean value. However, the mean of the means ± the standard deviation of the means for the six volunteers' fractional moving blood volume estimates is 37.6% ± 3.6.

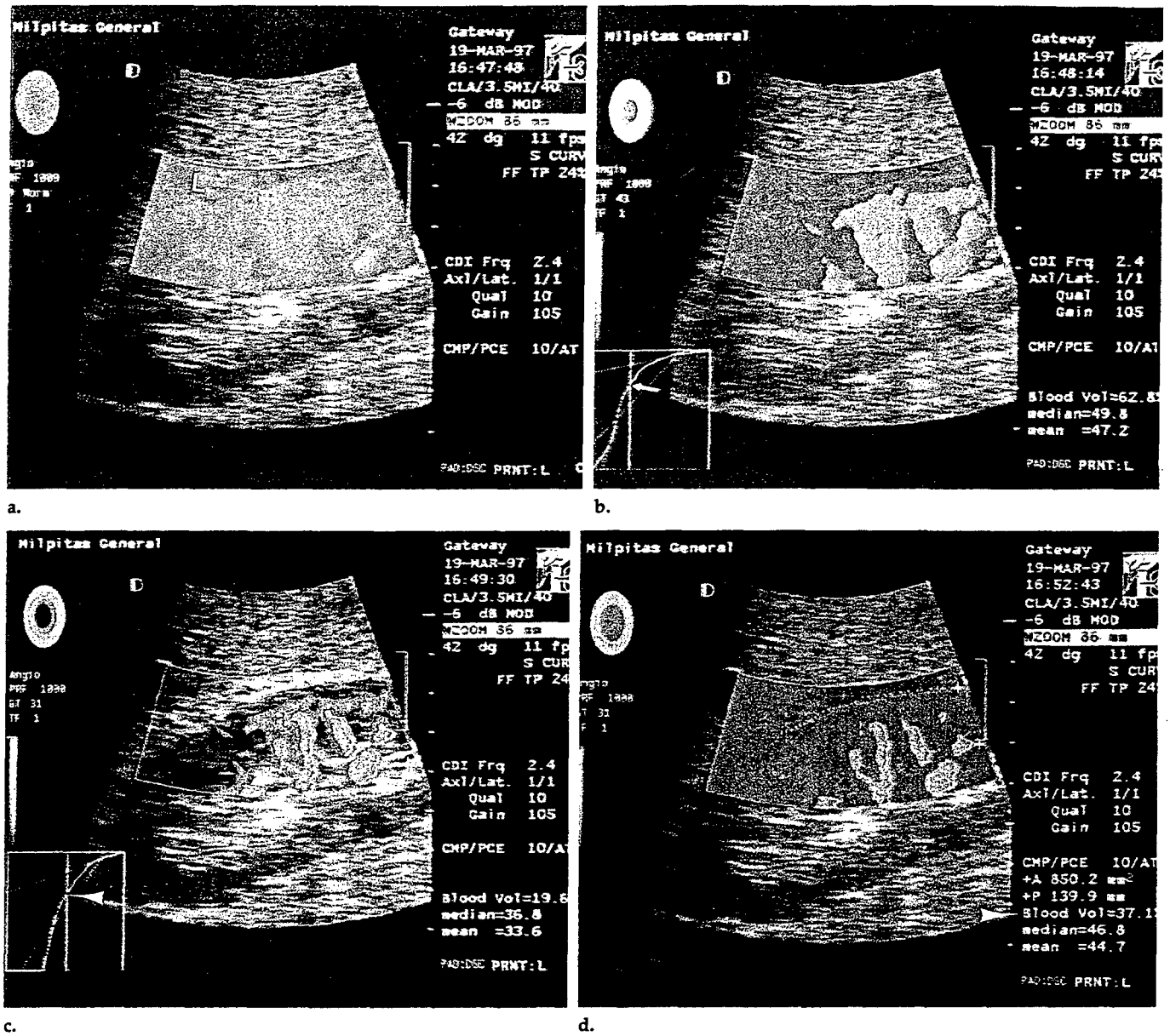

a. b.

c. d.

Figure 3. **(a)** Longitudinal US image of the renal cortex with near-field hilar vessels in a 49-year-old volunteer. The brighter the orange, the higher the Doppler power. Blue represents the noise floor or the lowest Doppler power displayed. Notice the large blue area in the near field, which corresponds to liver (*L*). **(b)** Same longitudinal US image as **a** after the first cumulative distribution has been taken over the entire color box in **a**. The green-tagged pixels correspond to those that could represent 100% blood on the basis of the knee of the cumulative distribution plot for the region of interest, shown in the lower left-hand corner. This curve is typical of the initial in vivo distributions in this study. The calculated position of the knee is marked with an arrow. All pixels with power values equal to or greater than the knee are green. (The highlighted pixels adjacent to the green-tagged regions are artifacts of photography and are not included in the green-tagged region.) **(c)** Same longitudinal US image as **b** after the second cumulative distribution has been taken over only those pixels labeled green in **b**. A second group of pixels, a subset of those in **b**, is labeled green and represents the final pixels determined to contain 100% blood. They were selected on the basis of the cumulative distribution plot, shown in the lower left-hand corner. The calculated position of the knee (arrowhead) corresponds to the lowest Doppler power that represents 100% blood; hence, this value is used to normalize all the tissue values in the image. Note that the second distribution demonstrates a much truer vascular geometry because it has segmented high-shear-rate from low-shear-rate blood flow within large vessels. Small vessels in tissue will not show up owing to high shear and partial volume averaging with tissue, that is, a fractional moving blood volume estimate of less than 100%. (The highlighted pixels adjacent to the green-tagged regions are artifacts of photography and are not included in the green-tagged region.) **(d)** Same longitudinal US image as **c** with the region of the cortex to be measured enclosed by the dotted line. The fractional moving blood volume estimate was calculated over that entire region and is normalized by the value selected in **c**. The fractional moving blood volume estimate in this case was 37.1% (arrowhead). (Again, the highlighted pixels adjacent to the green-tagged regions are artifacts of photography and are not included in the green-tagged region.)

DISCUSSION

The ultimate aim of many flow imaging techniques is to image vascularity or perfusion, and US is no exception. The opportunity for US to display vascularity has never been better. With contrast agents on the horizon and power Doppler, it is now possible for US to directly display the amount of moving blood in tissue, because, unlike standard mean-frequency color Doppler, the power in the Doppler signal is a reflection of the vascular blood volume of the tissue sample (20–22,31). Furthermore, power Doppler has the potential to overcome a major limitation of US vascularity measurements. By normalizing power Doppler signals in tissue against a blood vessel that is in or

near a region being evaluated, it is possible to compensate for the distance between the transducer and the region of interest, the attenuation coefficient of the overlying tissue, and the available imaging aperture, among other things (32).

The problem with this strategy is that the amplitude of the Doppler shift signal is highly dependent on rouleaux formation (18–22), which makes it impossible to merely select any point within a large vessel for normalization. However, by selecting a normalization value from the region of high shear near the vessel wall, the effects of rouleaux can presumably be minimized. This creates a situation that approximates that in small vessels in tissue where the shear is high and rouleaux is low (25).

Hence, a normalization technique must allow detection of blood vessels and identification of a position in the vessels to use for normalizing. The flow phantom study shows that the cumulative distribution can find blood vessels. In fact, it can optimally find them to within about 0.3 dB relative to the observer. In the clinical portion of the study, we typically used the tangent estimate, the poorer of the two estimating techniques, because it tended to overestimate the number of pixels that may contain 100% blood and thus increased the number of points included in the distribution. However, even by using an optimal technique such as the subjective method in the flow phantom, regions still are selected in the "hypovascular" tissue bath that were identified as flow-containing (Fig 1). Findings in the right kidneys studied were similar. This is not surprising and would be expected, at least in the first distribution, given the presence of small blood vessels inside tissue, which are analogous to the random high signals in the water bath.

We used a continuous-flow phantom, even though flow in vivo can clearly be pulsatile. We decided to do this because power Doppler is generally highly frame averaged in vivo. This has the effect of averaging out the pulsatility in the sampling. Hence, the nonpulsatile phantom would in some sense be an estimate of what happens in this first approximation. Yet, pulsatility will change the velocity distribution in a vessel, which will change the power distribution on the basis of the shear rate effects, as described above. This may require further study.

After determining the knee of the first distribution, we used a second distribution to find the normalization value in vivo. The reason for this is that, as in the flow phantom, the first distribution essentially located the wall or the neighborhood just outside of the walls of blood vessels that would be used for normalization. We needed to find a value inside the vessels to use as a standard in normalization. Thus, the second distribution over only the vessels accomplished this.

If we had not included a second distribution, we would have had the problem of distinguishing an organ of normal vascularity that is located deep in the body from a superficial organ with low vascularity. The reason for this is that the first distribution only basically locates the walls of large vessels, as shown above. It will find the walls whether an organ is deep and normal or superficial and hypovascular. Because we use an approximation of the knee as the threshold and this knee is defined relative to the parenchymal, hypovascular tissue, dividing this threshold into the tissue value will give a similar ratio in both cases. The distinction between a deep organ and a superficial one does not lie in the vessel boundaries but is in the Doppler power of the blood. For identical vessels, the more superficial, the more power the blood will have. This requires that a second distribution be taken over the vessels themselves to actually find a normalization value representative of the blood in the vessels. This value is a function of the vessel depth. We could have just identified the vessels manually or by using some other technique and performed a distribution over the vessels only. Then we would have needed only one distribution. The first distribution lets us automate the method.

There obviously have to be at least two points of negative curvature to find two knees in our process, and it makes sense that there should be at least two. The first knee separates the hypovascular parenchyma from the blood vessels, and the second knee separates the high-rouleaux central portions of blood vessels from the high-shear margins of the vessels. There will always be more points in the first distribution, because it includes the vessels and the hypovascular tissue, and, given a large enough region of interest, the first knee will dominate and will be the one selected with our method. Once the vessels have been segmented out, the method detects the second knee. If the number of points included in this second distribution is small, it may limit the ability to accurately detect a knee in some circumstances. We did not encounter this problem in this study; however, this may require a change in strategy when very small regions are being measured. This effect can be seen in Figure 3b and 3c: The knee is well defined in Figure 3b but is not as well defined, although present, in Figure 3c.

It is clear in this study that we have not determined where that precise site in the vessel is or what the true normalization value should be. However, we have done the next best thing; that is, we have identified a method that compensates for the rouleaux and at-

Table 2
Comparison of Methods for Locating the Knee Position of the Cumulative Distribution for the Flow-Tube Experiments

Run	Subjective Knee Position (dB)	Knee Position		
		Two-Tangent Model (dB)	Rotated Curve Peak (dB)	Second-Order Polynomial Fitted Peak (dB)
1	6.09	4.69	5.53	5.44
2	9.09	8.06	8.72	8.53
3	10.31	9.19	9.94	9.94
4	5.16	4.41	5.44	5.25
5	7.50	6.38	7.50	7.13
6	9.09	7.50	9.19	8.91
7	6.47	5.81	6.19	6.28
8	8.72	9.28	9.47	9.38
9	9.00	7.78	8.91	8.72
10	8.72	8.34	8.25	8.16
11	7.78	7.03	8.34	7.88
12	9.66	9.28	9.47	9.47
13	5.72	5.16	5.81	5.72
14	6.75	5.91	6.94	6.75
15	9.84	8.63	9.19	9.56

Note.—The subjective knee position is the standard of reference.

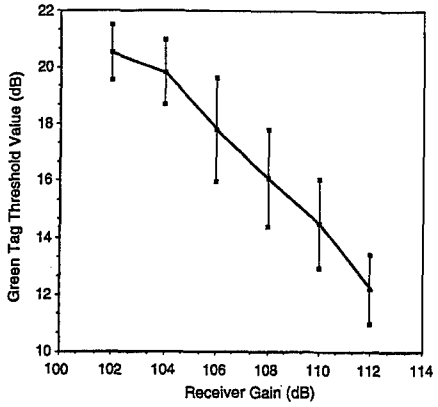

4.

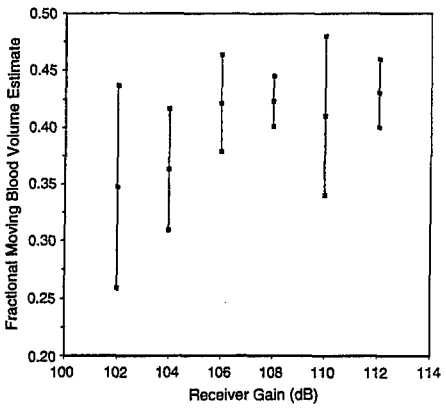

5.

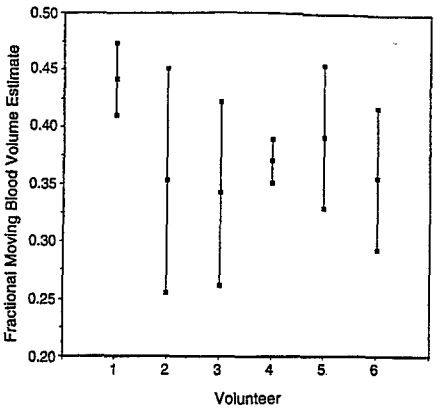

6.

Figures 4–6. **(4)** Green-tag threshold for the first cumulative distribution as a function of the receiver gain. These values represent the threshold for those pixels that may contain 100% blood. Only those pixels with higher power values than the threshold will be considered as possibly containing 100% blood in the algorithm used. The points are bounded above and below by ±1 standard deviation. Notice that the slope is negative, which means that the lower the gain, which corresponds to weak signal or large amounts of attenuation, the more dynamic the range that may be assigned to blood. **(5)** Fractional moving blood volume estimates as a function of receiver gain in the single volunteer. The points represent means ± 1 standard deviation. **(6)** Fractional moving blood volume estimates in the six volunteers. The points represent means ± 1 standard deviation.

tenuation problem in a general way. First, we have shown that the plot of the initial normalization value with receiver gain showed a continuous compensation for different amounts of signal by setting the normalization value to different fractions of the usable color dynamic range (Fig 4). This change in normalization compensated for the varying amounts of backscattered signal received at the different receiver gains, which corresponded to increasing amounts of attenuation, increasing depth, decreasing amounts of available transducer aperture, or a combination of these. The slope of the regression line through the data defined in Figure 4 shows a clear trend, with a 95% confidence interval that did not intersect zero. Thus, there was a distinct and significant decrease in the proportion of the color dynamic range that was assigned to 100% blood as the signal strengthened, or, conversely, the weaker the signal, the more of the dynamic range that was assigned to 100% blood.

This result makes sense if one considers that, if there were no detectable flow, flowing blood would look like everything else, and the entire dynamic range would look as if it contained 100% blood. The same problem would also occur in highly oversaturated images, where the gain is so high that everything, including noise, is enhanced to look like blood. This would have created a jump at the high receiver gain end of the curve if we had gone high enough. However, at that point, everything would be saturated and it would be impossible to distinguish blood vessels from less vascular surrounding tissue. This is unlikely to happen in practice because the user would immediately recognize it and turn the gain down, as occurs in blooming with contrast agents (33,34). However, the differential blooming effect of power Doppler is an advantage here, where, unlike in mean frequency color US, the display increase corresponds to the amount of signal present. Hence, vessels will still look brighter than background tissue, even with blooming (33,34), and our results suggest that as long as tissue can be distinguished from large blood vessels, the fractional moving blood volume estimate method could work in principle.

Second, once depth dependence of the transducer beam profile and attenuation are compensated for, the measurement of the same tissue region should be identical if the normalization method is working. Figure 5 shows this to largely be the case. The slope of the regression line through the data that describe the fractional moving blood volume estimates for gain settings of 104–112 dB was not different from zero to within 95% confidence (35). Hence, when there was sufficient signal to detect, the method compensated for the attenuation and transducer effects, as one would hope. However, when the data included the 102-dB values, there was a significant trend. In addition, the variability in the 102-dB measurement was higher than that in any of the others. The implication here is that when there is very little flow to detect, the method undercompensates and results become more variable. This suggests that when the signal is weak and is harder to detect, the method tends to locate a normalization value within the high-rouleaux portion of the flow stream and would, in a sense, overcompensate for the lost signal in the cortex, where the rouleaux effects are small. This would give a low estimate because the method would be comparing high-rouleaux areas in vessels to low-rouleaux areas in tissue. At some attenuation level, the Doppler signal will be too weak to measure, and any normalization technique will fail. One compensating fact is that when the signal gets very weak, it is still possible to compare the measurement to itself (17). Hence, the normalization from day to day may make it possible to evaluate relative flow changes in the same organ, even if the attenuation is high.

Finally, the evaluation of the volunteers without preparation estimated the potential variability in the method under scanning conditions. Clearly, one would like a technique with little or no variability at all; yet, in some cases the standard deviation in the measurements was up to 10%, which produced a variability relative to the local mean of approximately 30% from day to day, even when the signal was optimized. In these studies, there was no control for hydration, time of day, or fasting; all of which could have influenced the variability. Furthermore, given the single-volunteer studies, where the variance was smaller, it may be reasonable to presume that the variability is the true variation in the blood flow to the renal cortex. It is clear to anyone who does US that there are regions of the cortex with more flow than others; so, when performing scanning in the same per-

son on different days it is possible to obtain different results.

Will such variability preclude using this test? We do not think so. First, the mean values are very close among all the individuals, which suggests that a mean value may be usable in any given case. Thus, taking the mean of several measurements may give very reasonable results. This is exactly what is done presently with all resistive index measurements. Second, there can be equally wide variability among results of other parametric tests, such as resistive indices, pulsatility indices, acceleration, and acceleration times (36–38). Each of these has found use in the medical community. Finally, there are ways to improve the collection on the horizon, that is, three-dimensional imaging (16). This method would be perfectly integrated into a three-dimensional acquisition system. The segmentation would be used in the same way, but the sampling would be more robust. Given the large set of flows that would be sampled in the cortex in three dimensions, the flow variation in an organ would likely decrease.

Besides the limitations described above, there are others. As mentioned above, we have not defined the absolute fractional blood volume in the kidney. Although the mean values obtained are within or close to the published normal levels in the kidney (39–41), we do not know if those numbers measured here are in fact absolute fractional blood volume estimates. This may be true, but it will likely have little effect on the clinical application of such a measure as this. There are plenty of "indices" that relate to physiologic parameters of interest but may not directly measure them, such as the resistive index (42,43). Also, there are clearly flows that will not be included in this measurement. Capillary flow, for instance, is too slow to measure by using present Doppler techniques. Thus, these vessels will not be included in any vascularity estimate derived with our method. Of course, capillaries will not contribute to any US color Doppler vascularity measure, in neither mean-frequency color-flow nor power mode. In addition, vascularity assessments by using color Doppler techniques cannot be easily normalized, unlike ours. Hence, we believe that our method should surpass these.

In conclusion, we have defined a method for normalizing the power Doppler fractional moving blood volume estimate by using properties of the cumulative Doppler power distribution. The technique is almost completely nonsubjective and could easily be automated. The method works in phantom studies to find blood vessel boundaries, can be normalized for depth, gives constant measurements for the same flow situation largely independently of body habitus, and gives reasonable mean fractional moving blood volume estimates in healthy volunteers with a variability similar to that of other functional parametric indices. Further studies in pathologic cases are needed to define its usefulness.

APPENDIX

Quantitatively, the definition of the intersection points and tangent lines looks like this: $P'(x) = Ax + B$, which is the form of the best-fit line for a given distribution, where $P'(x)$ is the estimated cumulative value for a given x, the Doppler power, and A and B are constants. If $P(x)$ is the true distribution of the data, then $P(x) - P'(x)$ will be zero at the points of intersection of the true distribution and the best-fit line. Because this is real data, we cannot rely on the actual points of intersection being in the data set. Hence, one can identify the point in the data set closest to the intersection as being the one where there is a sign change. For example, an intersection would lie immediately between points x_i and $x_i + 1$ if $P(x_i) - P'(x_i) < 0$ and $P(x_i + 1) - P'(x_i + 1) > 0$. As a first approximation, one could choose either x_i or $x_i + 1$ as the intersection. Because we are interested only in a set of points centered at either x_i or $x_i + 1$ to define a tangent, it does not really matter which point we pick. Choosing either one of these points at each intersection, we empirically selected a 21-point region of interest centered about each selected point, for example, $x_i \pm 10$ points, and fitted a line through each group of 21 points. We selected a 21-point region because that worked well empirically. This local, fitted line is the local tangent.

The final complication is that it is possible that there could be more than two intersections of the global best-fit line with the distribution. To get around this possibility, we progressively identified each point of intersection of the best-fit line with the cumulative distribution by moving from the origin toward increasing abscissa values, that is, Doppler power. We then selected the first pair of tangent lines in which the difference between their slopes was negative, that is, in which their slopes were decreasing or the curvature was negative. For example, if T is a tangent line and i is a set of abscissa values of intersection points that range sequentially from 1 to n, then $T(i)$ is the line tangent to the cumulative distribution at i. If slope $T(i)$ is the slope of tangent line $T(i)$ and if $T(i)$ and $T(i + 1)$ are the first pair of tangent lines encountered when moving toward the right from the origin whose difference in slopes is negative (slope $T(i + 1)$ − slope $T(i) < 0$), then the intersection of $T(i)$ and $T(i + 1)$ is the chosen point for the knee. ■

References

1. Tanaka S, Kitamura T, Fujita M, et al. Color Doppler flow imaging of liver tumors. AJR 1990; 154:509–514.
2. Shiamato K, Sadayuke S, Ishigaki T, et al. Intratumoral blood flow: evaluation with color Doppler echography. Radiology 1987; 165:683–685.
3. Bourne T, Campbell S, Steer C, et al. Transvaginal colour flow imaging: a possible new screening technique for ovarian cancer. Br Med J 1989; 299:1367–1370.
4. Luker GD, Siegel MJ. Pediatric testicular tumors: evaluation with gray-scale and color Doppler US. Radiology 1994; 191:561–564.
5. Adler DD, Carson PL, Rubin JM, Quinn-Reid D. Doppler US color flow imaging in the study of breast cancer: preliminary findings. Ultrasound Med Biol 1990; 16: 553–559.
6. Sohn CH, Stolz W, Grischke EM, et al. Die dopplersonographische untersuchung von mammatumoren mit hilfe der farbdopplersonographie, der duplex sonographie und des CW-Dopplers. Zentralbl Gynakol 1992; 114:249–253. [German]
7. Dixon JM, Walsh J, Paterson D, Chetty U. Colour Doppler ultrasonography studies of benign and malignant breast lesions. Br J Surg 1992; 79:259–260.
8. Cosgrove DO, Bamber JC, Davey JB, McKinna JA, Sinnett HD. Color Doppler signals from breast tumors: work in progress. Radiology 1990; 176:175–180.
9. Cosgrove DO, Kedar RP, Bamber JC, et al. Breast diseases: color Doppler US in differential diagnosis. Radiology 1993; 189:99–104.
10. Kedar RP, Cosgrove DO, Bamber JC, Bell DS. Automated quantification of color Doppler signals: a preliminary study in breast tumors. Radiology 1995; 197:39–43.
11. Rifkin MD, Sudakoff GS, Alexander AA. Prostate: techniques, results, and potential applications of color Doppler US scanning. Radiology 1993; 186:509–513.
12. Newman JS, Bree RL, Rubin JM. Prostate cancer: diagnosis with color Doppler sonography with histologic correlation of each biopsy site. Radiology 1995; 195:86–90.
13. Carson PL, Moskalik AP, Govil A, et al. The 3D and 2D color flow display of breast masses. Ultrasound Med Biol 1997; 23: 837–849.
14. Shung KK, Sigelmann RA, Reid JM. Scattering of ultrasound by blood. IEEE Trans Biomed Eng 1976; 23:460–467.
15. Hottenger CF, Meindl JD. Blood flow measurement using the attenuation-compensated flowmeter. Ultrason Imaging 1979; 1:1–15.
16. Carson PL, Li X, Pallister J, Moskalik A, Rubin JM, Fowlkes JB. Approximate quantification of detected fractional blood volume in the breast by 3D color flow and Doppler signal amplitude imaging. In: Levy M, McAvoy BR, eds. 1993 ultrasonics symposium proceedings. Institute for Electrical and Electronics Engineers catalog no. 93CH3301-9. Piscataway, NJ: Institute for Electrical and Electronics Engineers, 1993; 1023–1026.
17. Rubin JM, Adler RS, Fowlkes JB, et al. Fractional moving blood volume: estimation with power Doppler US. Radiology 1995; 197:183–190.
18. Sigel B, Machi JJ, Beitler JC, Justin JR. Red cell aggregation as a cause of blood-flow echogenicity. Radiology 1983; 148:799–802.
19. Machi JJ, Sigel B, Beitler JC, Coelho JCU,

Justin JR. Relation of in vivo blood flow to ultrasound echogenicity. JCU 1983; 11:3–10.
20. Shung KK, Cloutier G, Lim CC. The effects of hematocrit, shear rate, and turbulence on ultrasound Doppler spectrum from blood. IEEE Trans Biomed Eng 1992; 39:462–469.
21. Shung KK. In vitro experiment results on ultrasonic scattering in biological tissues. In: Shung KK, Thieme GA, eds. Ultrasonic scattering in biological tissues. Boca Raton, Fla: CRC Press, 1993; 291–312.
22. Shung KK, Kuo IY, Cloutier G. Ultrasound scattering properties of blood. In: Roelandt J, Gussenhoven EJ, Bom N, eds. Intravascular ultrasound. Dordrecht, the Netherlands: Kluwer Academic, 1993; 119–139.
23. Yuan YW, Shung KK. Ultrasonic backscatter from flowing whole blood. I. Dependence on shear rate and hematocrit. J Acoust Soc Am 1988; 84:52–58.
24. Feynman RP, Leighton RB, Sands M. The Feynman lectures on physics. Vol 2. Reading, Mass: Addison-Wesley, 1964; 41–2.
25. Whitmore RL. The flow fluids. In: Whitmore RL, ed. Rheology of the circulation. Oxford, England: Pergamon, 1968; 37–46.
26. Metz CE. Basic principles of ROC analysis. Semin Nucl Med 1978; 8:283–298.
27. Halperin EJ, Albert M, Krieger AM, Metz CE, Maidment AD. Comparison of receiver operating characteristic curves on the basis of optimal operating points. Acad Radiol 1996; 3:245–253.
28. Papoulis A. Probability, random variables, and stochastic processes. New York, NY: McGraw-Hill, 1965; 92–94.
29. Press WH, Flannery BP, Teukolsky SA, Vetterling WT. Numerical recipes in C: the art of scientific computing. Cambridge, England: Cambridge University Press, 1988; 299–302.
30. Rubin JM, Bude RO, Carson PL, Bree RL, Adler RS. Power Doppler US: a potentially useful alternative to mean frequency-based color Doppler US. Radiology 1994; 190:853–856.
31. Meyerowitz CB, Fleischer AC, Pickens DR, et al. Quantification of tumor vascularity and flow with amplitude color Doppler sonography in an experimental model: preliminary results. J Ultrasound Med 1996; 15:827–834.
32. Goldstein A. Physics of ultrasound. In: Rumack CM, Wilson SR, Charboneau JW, eds. Diagnostic ultrasound. St. Louis, Mo: Mosby–Year Book, 1991; 2–18.
33. Murphy KJ, Bude RO, Dickinson LD, Rubin JM. Use of intravenous contrast in transcranial sonography: preliminary observations. Acad Radiol 1997; 4:577–582.
34. Burns PN. Harmonic imaging with ultrasound contrast agents. Clin Radiol 1996; 51(suppl):50–55.
35. Metz CE. Quantification of failure to demonstrate statistical significance: the usefulness of confidence intervals. Invest Radiol 1993; 28:59–63.
36. Kliewer MA, Tupler RH, Carroll BA, et al. Renal artery stenosis: analysis of Doppler waveform parameters and tardus-parvus pattern. Radiology 1993; 189:779–787.
37. Keogan MT, Kliewer MA, Hertzberg BS, DeLong DM, Tupler RH, Carroll BA. Renal resistive indexes: variability in Doppler US measurement in a healthy population. Radiology 1996; 199:165–169.
38. Paulson EK, Kliewer MA, Frederick MG, Keogan MT, Delong DM, Nelson RC. Hepatic artery: variability in measurement of resistive index and systolic acceleration time in healthy volunteers. Radiology 1996; 200:725–729.
39. Selkurt EE. The renal circulation. In: Hamilton WF, Dow P, eds. Handbook of physiology, circulation. Vol 2, section 2. Washington, DC: American Physiological Society, 1963:1471.
40. Ladefoged J, Pedersen F. Renal blood flow, circulation times and vascular volume in normal man measured by the intraarterial injection: external counting technique. Acta Physiol Scand 1967; 69:220–229.
41. Wiencek JG, Feinstein SB, Walker R, Aronson S. Pitfalls in quantitative contrast echocardiography: the steps to quantitation of perfusion. J Am Soc Echocardiogr 1993; 6:395–416.
42. Bude RO, Rubin JM, Platt JF, Fechner KP, Adler RS. Pulsus tardus: its cause and potential limitations in detection of arterial stenosis. Radiology 1994; 190:779–784.
43. Halpern EJ, Deane CR, Needleman L, Merton DA, East SA. Normal renal artery spectral Doppler waveform: a closer look. Radiology 1995; 196:667–673.

ELSEVIER

Ultrasound in Med. & Biol., Vol. 24, No. 7, pp. 945–952, 1998
Copyright © 1998 World Federation for Ultrasound in Medicine & Biology
Printed in the USA. All rights reserved
0301-5629/98 $19.00 + .00

PII S0301-5629(98)00055-6

● *Original Contribution*

3-D COLOR DOPPLER IMAGE QUANTIFICATION OF BREAST MASSES

PAUL L. CARSON, J. BRIAN FOWLKES, MARILYN A. ROUBIDOUX, AARON P. MOSKALIK, ANURAG GOVIL, DANIEL NORMOLLE[†], GERALD LECARPENTIER, SHINEY NATTAKOM, MARK HELVIE and JONATHAN M. RUBIN

Departments of [†]Radiology and [‡]Biostatistics, University of Michigan Medical Center, Ann Arbor, MI, USA

(*Received* 15 *September* 1997; *in final form* 3 *April* 1998)

Abstract—In this article, new measures obtained from color Doppler images are introduced and a pilot study is described, in which these and previously published indices are evaluated for use in future work. Twenty women with breast masses observed on mammography and going to surgical biopsy were studied. Of the masses, 11 proved to be benign and 9 were malignant. Both 3-D mean frequency shift (f-CDI) and power mode Doppler (p-CDI) imaging were performed. To identify the mass and other regions of interest, vessels were displayed as rotatable 3-D color volumes, superimposed on selectable grey-scale/color flow slices. Doppler signals were recorded in each of 6 ellipsoidal regions of interest in and around the mass and 2 in normal tissues. Seven measures were computed in each region, three from power mode, two from mean frequency and two from combinations of both. Radiologists rated the grey-scale appearances of the masses on a scale of 1 to 5 (5 = most suspicious) for each of 6 conventional grey-scale criteria. Of the individual vascularity measures in individual ROIs, the log speed-weighted pixel density and log power-weighted pixel density in the lesion internal periphery showed the greatest discrimination of malignancy, although neither was statistically significant nor as good as the peak variables described below. The mean visual grey-scale rating was the best discriminator overall, but two peak vascularity measures each made promising scatterplots in conjunction with the average visual grey-scale rating. These two vascularity measures were the log peak normalized power-weighted pixel density (peak NPD) and log of peak mean Doppler frequency times the peak NPD ($v_M \cdot NPD_M$). Each of these two values was the maximum in any one of the five chosen ROIs closely associated with the mass. A possible rationale for the relative success of these peak values is the blood signal's normalization and the inhomogeneity of most breast cancers and the expectation that the highest velocities (shunting) and largest collections of blood are not necessarily in the same region in and around the tumor. Peak NPD of cancers varied with age, decreasing by a factor of 45 from 33 to 77 y.
© 1998 World Federation for Ultrasound in Medicine & Biology.

Key Words: **Blood, Angiogenesis, Blood volume, Perfusion, Ultrasound, Doppler, Image processing, Three-dimensional imaging, Breast cancer, Diagnostic imaging.**

INTRODUCTION

Visual assessment of color Doppler imaging, both power mode (p-CDI) and frequency shift (f-CDI), may be aided by quantitative analysis of information provided in the images. Several quantitative and semiquantitative studies have been performed recently (*e.g.*, Cosgrove et al. 1993; Huber et al. 1994; Kedar et al. 1994; Carson et al. 1995; Meyerowitz et al. 1996) and others summarized by Meyerowitz et al. (1996). Typically, these studies used mean frequency f-CDI from which values of the mean color pixel value and fraction of color pixels were calculated. Using the mean color pixel value, Huber et al. (1994) achieved a much higher sensitivity and specificity for differentiation of carcinomas from benign lesions than they did with visual analysis. Meyerowitz et al. (1996) quantified information on murine lung tumors in the power mode color Doppler imaging (p-CDI). One of the indices they measured in regions of interest (ROIs) was the mean power of color pixels. Their other two indices and terminology, color pixel density and power-weighted pixel density, were the same as two of those we have been investigating (Carson et al. 1995).

To standardize breast lesion vascularity measures further, to evaluate information provided in the new power mode color flow images, and to aid visual analy-

Address correspondence to: Paul Carson, Ph.D., Professor of Radiology, Kresge III, Rm. R2315, Univ. of Mich. Med. Center, Ann Arbor, MI 48109-0553. E-mail: pcarson@umich.edu

sis, we undertook a visual and digital analysis of information in a study including 3-D ultrasound examinations of 20 patients scheduled for breast biopsy (Carson et al. 1997). Studies of these biopsy-proven 20 cases (4 fibroadenomas, 7 other benign masses and 9 cancer cases) were reviewed by radiologists for this qualitative analysis, using six visual criteria of grey-scale characteristics (described in Methods) and 8 visual criteria of power mode Doppler characteristics. 3-D vascular/pulse-echo display provided a much stronger subjective appreciation of vascular morphology and allowed a somewhat better ultrasound discrimination of malignant masses than did the corresponding 2-D images or videotapes (specificities of 85%, 79% and 71%, respectively, at a sensitivity of 90%). Only in the 3-D display did the vascularity measures display a trend towards significance in this small study. The combined pulse-echo rating was the best discriminator of cancer for all three display methods. That same visual, 3-D pulse-echo analysis is employed in this present report for comparison with the digital vascularity assessment. Much of the background of this study was discussed in the visual analysis paper (Carson et al. 1997).

MATERIALS AND METHODS

General methods

Data were collected from 39 subjects in 44 examinations in this preliminary study. Subjects were selected after the decision to biopsy based on identification of a mass in mammography, clinical examinations or simple grey-scale ultrasound. The quantitative measures were calculated for only 20 different subjects, due to the quality in some studies and inconsistent system settings in the earlier studies. Masses of very low suspicion (*e.g.*, most fibroadenomas) were not included. Of the masses, 9 were malignant, 4 were fibroadenomas, and 7 were other benign masses.

Each examination consisted of one or more power mode 3-D scans and a frequency shift 3-D scan of the mass and the surrounding tissue. (The power mode scan analyzed was the one in which the lesion was best centered or there were the fewest artifacts.) The 3-D scans were acquired using the system described in Moskalik et al. (1995). This system consisted of a conventional ultrasound scanner (Spectra VST, Diasonics, Inc., Milpitas, CA), a modified mammography unit that applied mild compression to stabilize the breast and a motorized transducer positioner mounted to the mammography unit. A typical scan through an acoustically transparent window produced a 3-D volume of ultrasound data of the suspicious region of the breast from a series of approximately coronal 2-D images separated typically by a distance of approximately 3/f (mm), where f is the Doppler imaging frequency[†] in MHz. At the 6-MHz Doppler frequency of our 6–10 MHz linear array, the step size was 0.5 mm. Data from the 50–120 images per scan were then transferred to a workstation. With the linear array scanhead employed for this study, the images were typically 38 mm by 40 or 50 mm. Power-mode Doppler ultrasound was performed at a PRF of 700 Hz, an ensemble length of 14, and the minimum sample length and maximum gain not producing frequent color noise. The same was done in color-flow mode but with a higher PRF of 1000 Hz. At this setting, there was some aliasing, which decreased the recorded mean velocity in some ROIs of some subjects. RGB video image signals from the ultrasound system were digitized with a frame grabber (Targa 64). Using the manufacturer-supplied color maps, log-compressed, RGB p-CDI image signals were converted from color and decompressed to linear values proportional to the Doppler signal power. This conversion was tested by comparing the decompressed signals with relative backscatter as determined by concentrations of small polystyrene particles in water (Rubin et al. 1995). Similarly, f-CDI RGB signals were digitized and converted to the linear mean speeds in each pixel, as described below. Mean velocity in a pixel was calibrated with a flow tube phantom at a measured Doppler angle.

The six visual grey-scale criteria were defined with scales from 1 to 5, 5 being those characterized as the most malignant. Defined in more detail in Carson et al. (1997), they were smoothness, shape, and visibility of the margins plus echogenicity, orientation and attenuation of the mass. For echogenicity, a rating of 1 corresponded to anechoic (cystic). With solid masses, the order was reversed, to keep 5 as the most malignant rating. A rating of 2 was most echogenic and 5 was hypoechoic (but not fully cystic).

Quantitative measures

The Doppler signal power imaging mode (Rubin and Adler 1993; Rubin et al. 1994) and frequency-shift imaging mode provide the data necessary to quantify the Doppler image signal characteristics listed below. These are not absolute measures of tumor flow characteristics because they are dependent on a number of uncontrolled factors, discussed below. The relation of these quantities to fractional blood volumes and perfusion are also discussed more extensively elsewhere (Carson et al. 1993; Rubin et al. 1994, 1995, 1997). These quantities were developed to aid in the objective assessment of the role of Doppler vascularity imaging for a more definitive diagnosis of suspected carcinoma.

[†] The step size should, ideally, be approximately half the elevational 6-dB beam width.

Table 1. Summary of studied measures from the power mode and frequency shift modes of the color flow doppler images.

Abbreviation	Full name	Formula
PD	Power-weighted pixel density	$PD = \sum_{i=1}^{N_b} P_i/N_t$
NMPCP	Normalized mean power in colored pixels	$NMPCP = \sum_{i=1}^{N_b} \frac{P_i}{P_b} \Big/ N_b$
NPD	Normalized power-weighted pixel density	$NPD = \sum_{i=1}^{N_b} \frac{P_i}{P_b} \Big/ N_t$
SWD	Speed-weighted pixel density	$SWD = \sum_{i=1}^{N_b} V_i/N_t$
$\bar{v}$	Mean speed in colored pixels	$\bar{v} = \sum_{i=1}^{N_b} V_i/N_b$
SNPD	Speed and power-weighted normalized pixel density	$SNPD = \sum_{i=1}^{N_b} \frac{V_i P_i}{P_b} \Big/ N_t$
$v_M \cdot NPD_M$	Peak mean speed times peak NPD	$v_M \cdot NPD_M = \max(\bar{v}) \cdot \max(NPD)$

As can be seen, the first three measures in Table 1 are obtained only from the power-mode images. The fourth and fifth are from the frequency-shift color flow images and the last two utilize data from both modes. Symbols are defined in the text.

Quantities in Table 1 were calculated in each of the eight regions of interest (ROIs) defined in Table 2, where the borders of the masses were taken from the pulse echo image and palpation. N_b is the number of pixels with flow in them and N_t is the total number of pixels in the region of interest. P_i is the power Doppler value of the ith pixel and V_i is the Doppler speed from the absolute value of the mean frequency shift in the ith pixel, assuming the cosine of the Doppler angle = 0.5. This would give the correct speed averaged over many pixels for an isotropic distribution of vessels. This isotropic assumption is necessary because no vessel angle information is recorded at this time. To represent 100% blood for normalization of the blood signals, P_b is the average Doppler power value measured in a large vessel. NPD_i refers to a single region i and NPD_M refers to the peak of NPD_is among a defined set of regions. For $v_M \cdot NPD_M$, the maximum of $\bar{v}$ over any region and maximum value of NPD over any region were taken for defined sets of regions. The four normalized measures were introduced in Carson et al. (1993).

There is a problem of measuring $\bar{v}$ without aliasing effects when it is desired to see as much of the vascular tree as possible in f-CDI mode (as is done in p-CDI mode). One could scan at higher PRFs to avoid aliasing, but then the number of vessels seen without contrast agents and the diversity of their orientations might be too small for the unknown Doppler angles to average out. An intermediate PRF was employed.

The problem with absolute measures from most unnormalized power mode signal indices, such as power-weighted pixel density (PD) and color pixel density in either mode, f-CDI or p-CDI, is that the absolute measures increase with system gain and output and decrease with depth in the tissues due to attenuation and the lack

Table 2. List of the eight ROIs used in the quantitative analysis of the 3-D data.

1.	Lesion periphery; normally from the outer grey-scale border to 1 cm inside
2.	Lesion periphery, proximal side only (hemiellipsoidal version of region)
3.	Central core of those lesions that are >2 cm in diameter
4.	External periphery—mass grey-scale boundary to 1 cm outside
5.	External periphery, proximal side only (hemiellipsoidal version of Region 4)
6.	Abnormal region of highest vascularity (>1.5 cm diameter and >1 cm from mass, but associated with it)
7.	Normal fatty tissue volume
8.	Normal fibroglandular ROI

The measures listed in Table 1 are calculated from each region. Regions 1–6 are associated with the mass. The other Regions, 7 and 8, did not show early promise and were not analyzed extensively.

of sufficient signal level in color Doppler imaging to effectively utilize TGC over much of the field of view. Some preset TGC is used in power mode. The power measures that are normalized to the power signal from the largest vessel at a representative depth range also probably can fluctuate strongly in some cases. This study begins the assessment of whether or not the normalization will improve stability of the vascular measures. What is needed for the normalization to work well is that the normalizing vessel be larger than the color Doppler sample volumes and be at the right depth or depths. In this study, the normalization was usually based on a single measurement at a single depth closest to the region of interest. Work is progressing on efforts to define signals from 100% blood, based on all the larger vessels in each given depth range (Rubin et al. 1997), and to eliminate signals from low-shear portions of vessels where abnormally high Doppler signals are produced by rouleaux formation.

3-D displays were illustrated in the visual analysis report (Carson et al. 1997). The data were used to form 3-D isosurface renderings of the vasculature that could be rotated and shown in correct positional relationship to grey-scale slices of the 3-D image. An example of the employed display on a nonpalpable, 7-mm intraductal carcinoma is illustrated more fully on our Web page: http://www.med.umich.edu/ultrasound/anim/develop/Case38.html.

A typical example of a 3-D color flow image display without vascular isosurface delineation is shown in Fig. 1a–d. The grey-scale borders of this infiltrating ductal carcinoma are demarcated by a translucent ellipsoid representing Region 1 (defined in Table 2) for quantitative analysis. Software was developed in AVS-5 (Advanced Visualization System, Waltham, MA) to select an ROI from the 3-D images as an ellipse or an ellipsoidal annulus whose 3 major and minor axes and center coordinates were entered and adjusted by the user to visually fit the borders of the desired ROI. AVS is available for most Unix workstations and on Windows NT systems. This was done to create reproducible ROI measurements and to help standardize the method of data acquisition between different sets of data. Subsequent to the analysis reported here, versions in AVS Express are now mouse-driven on the images and ROIs are arbitrarily-oriented ellipsoids and ellipsoidal annuli fit by least squares to a few border points marked on multiple slices or orthogonal views. Both ellipsoidal versions represent compromise between totally free shaping of the ROI (by laborious marking of borders on all slices and with cumbersome display and computations) and the rectangular ROI typically available on imaging systems. The quantities were calculated for each case in each of the regions of interest in Table 2 that could be identified. The 3-D image sets in both Doppler image modes were carefully compared to select, as well as possible, the same ROIs in both p-CDI and f-CDI image sets.

Because the two sets of images were obtained from sequential series of 3-D scans, spatial matching of p-CDI and f-CDI coded pixels was quite crude for the pixel-by-pixel calculation of SNPD. For the matching of the entire ROIs required for calculation of $v \cdot NPD$ within any region, the image set registration by ROI selection was generally adequate to compensate for relative motion of the tissue and hand-held scanner frame. Normalization of the power signal was done with respect to the mean signal power centered in the largest vessel at or near the depth of the lesion.

RESULTS

Although data have been collected for 39 subjects, 11 were presumed normal or the preliminary diagnoses were unconfirmed. Some early studies were not quantified correctly or the mass was missed on the 3-D scans. Some of the startup quantification errors included use of incorrect color maps and other system settings, as well as extensive flash artifact. Analyzable data on the region of a mass were obtained in 20 cases with p-CDI and, in 17 of those cases, f-CDI was obtained as well. This provided 20 cases for NPD_M and 17 for $v_M \cdot NPD_M$. In all the malignant and fibroadenoma cases analyzed, a mass could be identified from grey-scale ultrasound. Lesion detection was sometimes guided by the local vascularity. In three of the benign cases, the mass could not be found ultrasonically and a region of relatively high vascularity at least 1.5 cm diameter was selected as the "lesion." Subjects in whom the signals were analyzed quantitatively are given in Table 3.

As examples of some of the measured quantities, the ranges and means of the NPD and SNPD for one of the regions-of-interest (ROI 1) are shown in Table 4 for the three different lesion types. The signal was normalized to the signal power from the largest, strongest signal area at about the same depth as the mass. ROI 1 is defined in Table 2 by an ellipsoidal annulus between the lesion boundary and 1 cm inside. There is considerable overlap for the individual results in this single ROI, but the means of NPD for malignant masses in this region are differentiated reasonably well from benign conditions, particularly those other than fibroadenoma. Means of SNPD from ROI 1 also are quite different for malignant than for both benign classifications.

The NPD and SNPD in Region 4 are not particularly good individual classifiers of cancer. They revealed the significant vascularity in the outer periphery of fibroadenomas. Tables 4 and 5 reveal large ranges of the two measures, even in ROI 1, and suggest that single mea-

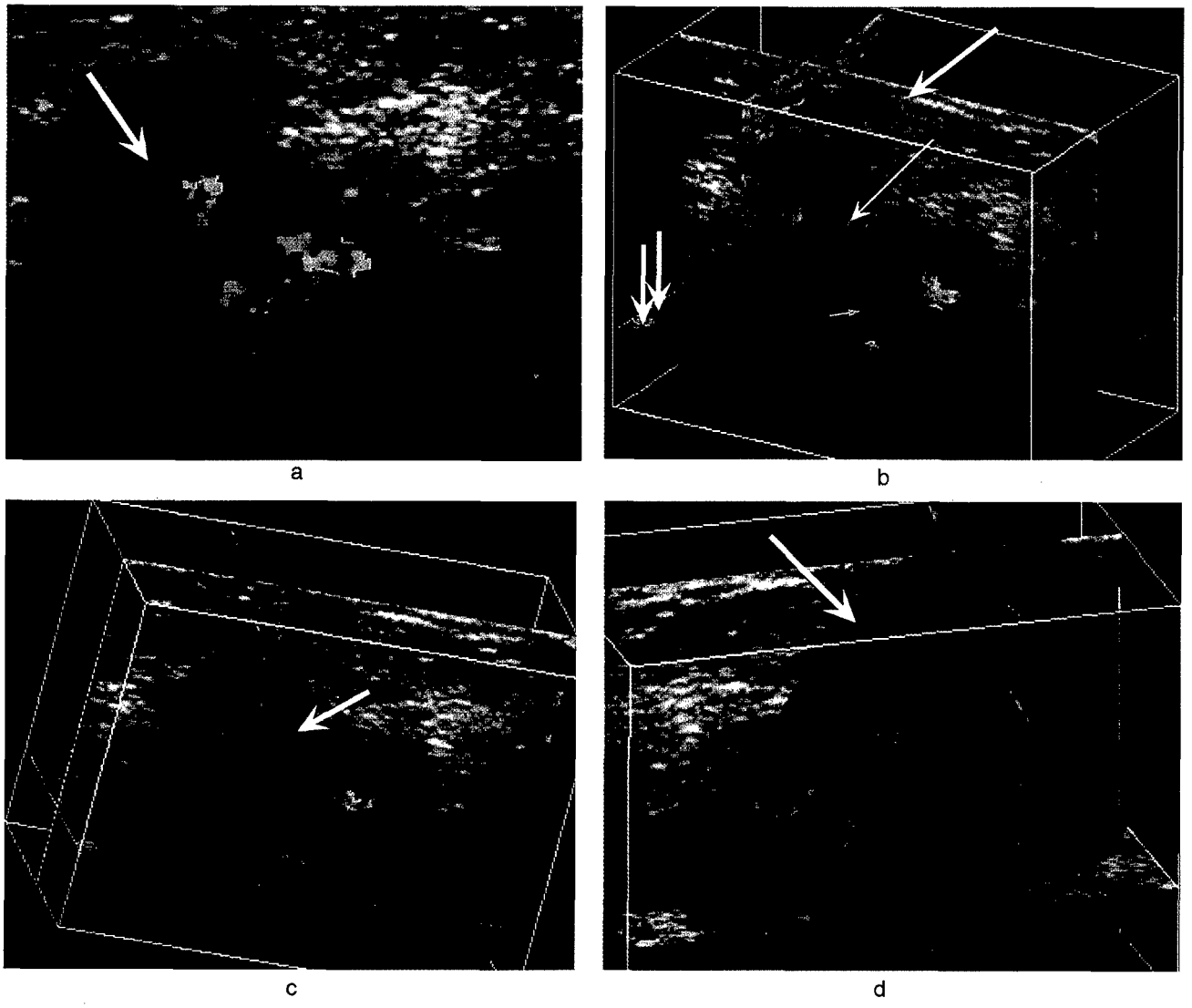

Fig. 1. 3-D display from a 49-y-old subject with an infiltrating ductal carcinoma. Clockwise from top left, vascularity detected in f-CDI mode is displayed (a) in one of the actual scan planes, and (b–d) in three orthogonal planes. In (a), the grey-scale-delineated mass is marked with the arrow. In (b–d), the border of ROI 1 is shown as a smooth, translucent, bluegreen, ellipsoidal surface. The large white arrow in (b) shows the line of contact of the scan head in the actual scanned plane and the dual arrows mark a plane at a constant depth from the surface, a C-plane. Vascularity in the scan plane and penetrating into the main tumor mass (ROI 1) is marked with small arrows. (c) Shows the same planes as (b), but with a different viewing angle. Also, the vascularity throughout the 3-D volume is shown as light blue 3-D isosurfaces (arrow), often obscuring the f-CDI colors lying within the individual planes. With rotation and stepping of planes, the 3-D vascularity isosurfaces display the vascular morphology quite well. (d) Is the same as (b), but viewed from the back side of the scanned plane. A dark blue ellipsoid shows the margins of the external periphery, ROI 4.

sures in individual ROIs may not be good indicators of overall discrimination ability of ultrasound.

Stepwise linear discriminant analyses were used as an exploratory tool to identify likely variables and combinations of variables in specific ROIs to discriminate between benign and malignant masses. The quality of a given discriminant function was evaluated by the cross-validated misclassification rates, and the importance of variables within those functions, by a *t*-test on the parameter. The only variable consistently identified as a discriminator between benign and malignant masses was speed-weighted color pixel density (SWD) in Region 1, the internal periphery of the lesion. A tree-based classification method was also employed and it consistently selected only power-weighted pixel density (PD), also from Region 1. In Region 1, for 100% correct identification of benign lesions, 50, 38 and 50% of cancers were correctly identified with SWD, PD and v · NPD, respec-

Table 3. Subjects examined and analyzed.

	Studied	Analyzed for NPD_M	Analyzed for $v_M \cdot NPD_M$
Presumed normal	8	–	
Fibroadenoma	7	4	3
Benign	8	7	7
Malignant	13	9	7
Unconfirmed	3	–	–

tively. At other thresholds, these true cancer and true benign rates were, respectively, 100% and 60% for SWD, 75% and 75% for PD and 67% and 89% for v · NPD.

More promising results were obtained when the highest value of a variable for any one of the mass-related regions was analyzed, rather than looking at a specific variable in a specified ROI. Two measures that made the most promising scatterplots in conjunction with the average of all 6 grey-scale visual classifications were the NPD_M (peak normalized power-weighted pixel density) in any of a subject's Regions 1, 2, 4, 5 & 6 and $v_M \cdot NPD_M$, in any one of those same regions. Region 3 was the only other region associated with the mass. It was not included because of its rare and inconsistent vascularity, although the small amount of vascularity in that region should not have affected the peak values discussed here.

Figure 2 shows such a scatterplot of log NPD_M and the average of all 6 grey-scale visual classifications for each subject. The malignant masses clustered near the upper right hand corner, as expected. The benign mass on the upper right, with a grey-scale rating of 3.0, was a rare case of bilateral diabetic mastopathy, that met many of our ultrasonic, mammographic and clinical criteria for cancer. The cancer with the lowest vascularity index had multiple small areas of flow in the proximal periphery of the mass (*i.e.*, the vascularity appeared lobular for what turned out to be a lobular carcinoma). Discriminant analysis on cancer vs. all benign masses provided the classification lines log $NPD_M = 1.55\ GS + 2.4$ and log $v_M \cdot NPD_M = 1.27\ GS + 3.0$, where GS is the average grey-scale rating. The sensitivities of 100% and specificities of 82% and 90%, for NPD_M and $v_M \cdot NPD_M$, respectively, are promising, but the statistical uncertainty in these numbers is large. Figure 3 shows a scatter plot of log $v_M \cdot NPD_M$ (peak $\bar{v}$ and peak NPD) and the average visual grey-scale for each subject studied. Note that all the measures of malignant masses are clustered near the upper right-hand corner and appear better differentiated from the benign measures than in Fig. 2. A line can be selected visually in Fig. 2 that provides 100% sensitivity and 100% specificity.

The vascularity of malignant lesions, as measured by the log of NPD_M among the five regions, did decrease significantly as a function of age. The linear regression was log $NPD_M = -0.028\ (\pm 0.007) \times \text{Age} - 0.47$. The

Table 4. Examples of two mass quantities for ROI 1, the lesion internal periphery.

	N	Min	Max	Mean
NPD (Lesion periphery to 1 cm inside mass)				
Benign	7	0.00000	0.00086	0.00029
Adenoma	4	0.00001	0.01088	0.00324
Malignant	9	0.00000	0.03718	0.00577
SNPD (Lesion periphery to 1 cm inside mass)				
Benign	7	0.00000	0.00193	0.00038
Adenoma	3	0.00000	0.00244	0.00097
Malignant	7	0.00000	0.03800	0.00618

Table 5. NPD and SNPD measures from ROI 4, which is defined as an ellipsoidal annulus between the lesion boundary and 1 cm outside.

	N	Min	Max	Mean
NPD (Lesion periphery to 1 cm outside mass)				
Benign	7	0.00002	0.00668	0.00167
Adenoma	4	0.00007	0.01500	0.00472
Malignant	9	0.00000	0.00684	0.00210
SNPD (Lesion periphery to 1 cm outside mass)				
Benign	7	0.00000	0.00311	0.00078
Adenoma	3	0.00003	0.02582	0.00925
Malignant	7	0.00000	0.02541	0.00400

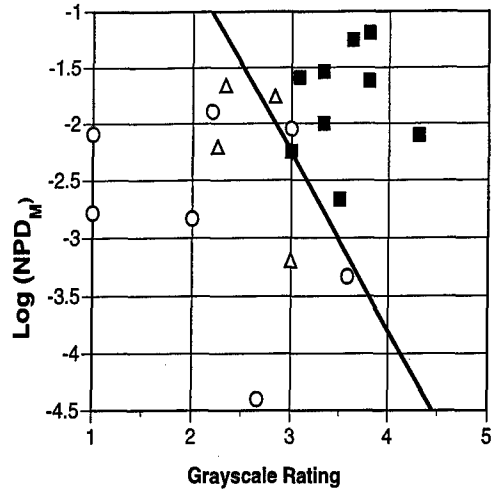

Fig. 2. Scatterplot of log NPD_M and grey-scale readings. Symbols are: benign = open circles; fibroadenomas = open triangles; cancer = solid squares. The linear discriminator is shown as the solid line.

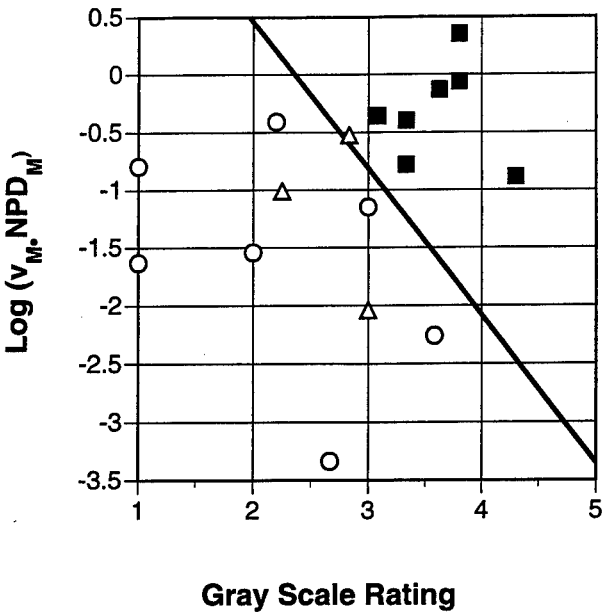

Fig. 3. The digital vascularity index shown here, $v_M \cdot NPD_M$ and grey-scale rating are over the regions used in Fig. 2 and symbols are as in Fig. 2.

intercept and slope of the fit were insignificant and significant, probability $< |t| = 0.22$ and 0.006, respectively (see Fig. 4). The decrease in NPD_M with age suggests that age might be a significant discriminator of cancer along with NPD_M and grey-scale rating. However, the number of data points in this study is too small for meaningful 3-variable analysis. Other key ultrasound

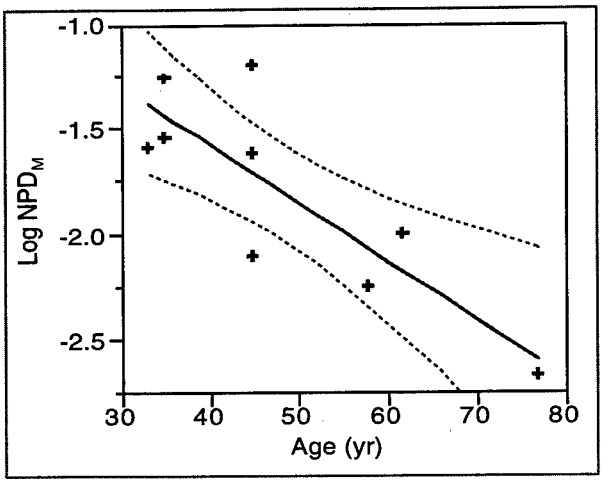

Fig. 4. Cancer vascularity as a function of age, showing a factor of 45 decrease in peak NPD among Regions 1, 2, 4, 5 and 6 from age 33 to 77 y. There is some uncertainty, as shown by the (dotted) 95% confidence limits of the (solid) linear regression line.

measures were not a significant function of age (*e.g.*, log NPD_M for benign cases, which had an insignificant but negative slope [$|t| > 0.12$]). An increase in grey-scale reading with age for benign cases was not significant nor was an increase in $v_M \cdot NPD_M$ with age for benign cases.

DISCUSSION

New, normalized measures of color Doppler image signals have been developed for potential assessment of tumor vascularity. Ellipsoidal ROIs have been applied in 3-D with recently developed display techniques to improve the sampling statistics and reliability of defining ROIs in and around the tumor, compared with measurements in only one or a few images.

Although the measures NPD and v · NPD are only an approximation to true fractional blood volume or perfusion, they provide quantification of what the clinician sees as well as some normalization for machine settings and ultrasound attenuation by tissues overlying the areas of interest. These measures may provide more reproducible results than what is currently done clinically. We previously referred to NPD as the detected fractional blood volume B_v, and to v · NPD as the speed-weighted detected fractional blood volume, B_{vv}, or even perfusion (Carson et al. 1993). We are now using the acronyms NPD and v · NPD, or their longer descriptive names, because of the potential for overinterpretation of the more vascularity-specific terms.

Speed-weighted pixel density (SWD) and power-weighted pixel density (PD) in Region 1 were identified as the best single discriminators in single ROIs. These observations are consistent with one recent criterion for discriminating malignant masses as those in which the vessels penetrate the mass (Bergonzi et al. 1993; Calliada et al. 1994; De Albertis et al. 1995).

The discrimination by either of these single variables in Region 1 alone was relatively poor. The less-than-stellar results of the linear discriminant and tree-based classification analyses might be expected, given the heterogeneity of cancer growth. Also, the statistical effects of small numbers of subjects were compounded by the relatively poor vascularization of the breast, so that there were large fluctuations in the vascularity in any one ROI detectable with the relatively high-frequency techniques employed for visualization of vascular morphology. It is possible that these statistical considerations were a reason that normalization did not improve the vascularity measures in individual ROIs in the same way that it did with the peak measures. The sparse vascularity made it not always possible to obtain an appropriate normalization value for each ROI.

Those concerns, including the anticipated tumor heterogeneity, were the basis for calculating the normal-

ized measures NPD_M and $v_M \cdot NPD_M$ from the peak value of NPD over the five employed regions associated with the mass and, separately, the maximum of $\bar{v}$ over those five ROIs. This utilization of peak values from possibly different ROIs provided the best discrimination on scatter plots as a function of grey-scale ratings. This relative success is consistent with the possibility that, due to shunting and other flow phenomena, peak $\bar{v}$ might be higher in one region associated with the tumor and high volumes of Doppler-imageable blood might be in another region. The specificity and sensitivity obtained using NPD_M or $v_M \cdot NPD_M$ in conjunction with mean grey-scale rating were consistent with or slightly higher than those obtained with visual vascularity and grey-scale ratings (Carson et al. 1997).

Decreased vascularity with age is to be expected in the normal breast, likely related to fatty replacement of glandular tissue in aging. The clear relation seen for NPD_M with age suggests that ultrasound vascularity measures as an indicator for cancer or for general tumor aggressiveness would be improved by normalizing for age.

Although these results are promising, the wide ranges of the vascularity measurements indicate that some breast cancers have very little detectable blood flow due to either low volume or low velocities. Some malignant cases only had vascularity in Region 6, a region associated with the mass but more than 1 cm away, suggesting fine vessel branching upstream from the cancer or most active perfusion well outside the cancer.

On either Fig. 2 or Fig. 3, a vertical line from the combined grey-scale score provides better discrimination in these data than does a horizontal line from either single vascularity measure. Vascularity will not be the sole criterion in most breast cancers, but it should contribute to the diagnosis because more malignant and benign masses were classified correctly here with inclusion of the vascular results. This additional discrimination was not statistically significant in this small set of subjects. These results, along with the known vascular characteristics of cancer such as localized shunting and blood pooling, do provide the basis for the hypotheses of a future study on an independent (test) set of subjects.

Acknowledgements—This work was supported in part by USPHS grant 1RO1CA55076 from the National Cancer Institute and to a lesser extent by the U.S. Army Medical Research and Materiel Command under Contract No. DAMD17-96-C-6061. The views, opinions and/or findings contained herein are those of the authors and should not be construed as an official Department of the Army position, policy or decision. Mihra Taljanovic, M.D. and Dorit D. Adler, M.D. contributed significantly to the clinical examinations and interpretations. The authors are indebted to Nancy Thorson, R.T., for assistance with subject recruitment, records and procedures and to Claudia Koitch for assistance with manuscript preparation.

REFERENCES

Bergonzi M, Calliada F, Corsi G, et al. Role of echo-color Doppler in the diagnosis of breast diseases. Personal experience. Radiol Med (Torino) 1993;85:120–3.

Calliada F, Raieli G, Sala G, et al. Doppler color-echo in the echographic evaluation of solid neoplasms of the breast: 5 years of experience. Radiol Med (Torino) 1994;87:28–35.

Carson PL, Govil A, Moskalik AP, et al. Lessons from digital vascularity measures in 3D power mode images of breast masses. In: Jellins J and Madjar H, eds. Didactic lectures and workshop presentations, International Breast Ultrasound School (with Ninth International Congress on the Ultrasonic Examination of the Breast), Indianapolis IN, International Breast Ultrasound School, Sept. 28–Oct. 1, 1995. 1995:186–191.

Carson PL, Li X, Pallister J, et al. Approximate quantification of detected fractional blood volume in the breast by 3D color flow and Doppler signal amplitude imaging. In: Levy M, McAvoy BR, eds. 1993 Ultrasonics Symposium Proceedings. Piscataway, NJ: Inst. for Electrical and Electronics Engineers (IEEE Cat. No. 93CH3301-9) 1993:1023–1026.

Carson PL, Moskalik AP, Govil A, et al. 3D and 2D color flow display of breast masses, Ultrasound Med Biol 1997;23:837–849.

Cosgrove DO, Kedar RP, Bamber JC, et al. Breast disease: color Doppler US in differential diagnosis. Radiology 1993;189:99–104.

De Albertis P, Oliveri M, Quadri P, et al. Retrospective analysis of color Doppler ultrasonography and flowmetry findings in solid nodular pathology of the breast. Radiol Med (Torino) 1995;89:28–35.

Huber S, Delorme S, Knopp MV, et al. Breast tumors: computer-assisted quantitative assessment with color Doppler US. Radiology 1994;192:797–801.

Kedar RP, Cosgrove DO, Smith IE, Mansi JL, Bamber JC. Breast carcinoma: measurement of tumor response to primary medical therapy with color Doppler flow imaging. Radiology 1994;190:825–830.

Meyerowitz CB, et al. Quantification of tumor vascularity and flow with amplitude color Doppler sonography in an experimental model: preliminary results. J Ultrasound Med 1996;15:827–833.

Moskalik A, Carson PL, Meyer CR, et al. Registration of three-dimensional compound ultrasound scans of the breast for refraction and motion correction. Ultrasound Med Biol 1995;21:769–778.

Rubin JM, Adler RS. Power Doppler. Diagnostic Imaging Dec. 1993; 66–69.

Rubin JM, Adler RA, Fowlkes JB, et al. Fractional moving blood volume estimation using Doppler power imaging. Radiology 1995; 197:183–190.

Rubin JM, Bude RO, Carson PL, Adler RS, Bree RL. Power Doppler: a potentially useful alternative to mean frequency-based color Doppler US. Radiology 1994;190:853–856.

Rubin JM, Bude RO, Fowlkes JB, et al. Cumulative power distribution function: Technique for defining a stable intravascular point for normalizing fractional moving blood volume estimates with power Doppler US. Radiology 1997;205:757–765.

Frederick W. Kremkau, PhD ▮ Christopher R. B. Merritt, MD ▮ Paul L. Carson, PhD ▮ Laurence Needleman, MD
Thomas R. Nelson, PhD ▮ Dolores H. Pretorius, MD ▮ Jonathan M. Rubin, MD, PhD

The American Institute of Ultrasound in Medicine and the Society of Radiologists in Ultrasound

Future Directions in Diagnostic US[1]

From modest beginnings about 50 years ago, ultrasonography (US) has become the most rapidly growing diagnostic imaging method in worldwide use today. Its versatility, portability, low cost, and efficacy have made US an indispensable tool in patient care. Recently, the value of US has been enhanced by improvements in both imaging and Doppler technology and the development of echo-enhancing agents.

Diagnostic US is based on the scattering of sound by tissue. Current methods of detecting and displaying amplitude and frequency contents of the backscattered ultrasound echoes have achieved high sensitivity and resolution, permitting excellent imaging of soft tissues and detection and characterization of tissue motion and blood flow in real time. Benefiting from dramatic improvements in computer power, basic US functions of gray-scale imaging and Doppler are expected to become even more powerful in the future. Even more exciting possibilities arise from the exploration of the complex interaction of sound with tissues to develop opportunities for novel methods of imaging that are not possible with other methods. Opportunities for further progress in diagnostic US are the following: (*a*) improved signal detection: echo-enhancing agents (contrast agents), harmonic imaging; (*b*) improved image display: three-dimensional US; (*c*) novel methods: anisotropic imaging, perfusion imaging, co-registration, elastography; (*d*) instrumentation: microimaging, endoimaging, telesonography; (*e*) therapy and intervention: high-intensity focused ultrasound therapy, guidance, gene therapy; (*f*) applications: intraoperative and endoscopic.

New developments that will affect the future of US are currently in progress and will constitute the focus of this overview. They include contrast agents, intraoperative and endoscopic applications, and three-dimensional imaging. Several other areas of development included in this discussion have not yet substantially penetrated clinical US but show promise for altering and improving the practice of US.

Index terms:
Radiology and radiologists, research
Subspecialty society messages
Ultrasound (US)

Radiology 1998; 209:305–311

[1]From the Center for Medical Ultrasound, Wake Forest University School of Medicine, Medical Center Blvd, Winston-Salem, NC 27157-1039 (F.W.K.); the Division of Diagnostic Ultrasound, Thomas Jefferson University Hospital, Philadelphia, Pa (C.R.B.M., L.N.); the Department of Radiology, University of Michigan, Ann Arbor (P.L.C., J.M.R.); and the Department of Radiology, University of California, San Diego (T.R.N., D.H.P.).
Received March 17, 1998; accepted May 16, 1998. **Address reprint requests to F.W.K.**
© RSNA, 1998
See also the article by Leopold (pp 312–313) in this issue.

Contrast Agents

Contrast agents (1–8) improve US by increasing the echo strength from within the body rather than by altering the US equipment. US contrast agents address several fundamental acoustic difficulties in imaging patients when there may be insufficient US contrast between diseased tissues and normal regions because the acoustic properties are not substantially different. Also, Doppler is less reliable in slow-flow velocities and in low-volume flow rates such as in high-grade stenoses, in which there are few moving erythrocytes to produce an adequate signal. Doppler signals also may be inadequate due to attenuation in such situations as deep vessels or when overlying plaque or bone diminishes the echo strength returning to the transducer.

The pharmaceutical industry is now creating a variety of US contrast agents. Agents being investigated include intravenous blood-pool agents that increase Doppler and gray-scale US signals systemically, and enteral agents that improve visualization of the bowel and the abdominal organs beneath the bowel. Companies have begun to market contrast agents overseas for radiologic and cardiac applications and in the United States for echocardiography.

Intravenous contrast agents rely on microbubbles of gas to strengthen the echoes by increasing backscatter. Manufacturing techniques ensure that there is uniformity of a small bubble size that permits the bubbles to cross the pulmonary circulation and capillary beds. Various designs have been used to keep bubbles intact so that the duration of enhancement can be extended to minutes. These designs include the use of fluorocarbons or other gases to resist dissolution and the use of a coating or shell over the bubbles to make them more resistant to destruction. The quantity of gas used is quite small, and the materials used with the gas are chosen to be as inert as possible, leading to safety profiles that have been quite good in clinical trials.

Clinical trials of contrast agents have shown that both spectral and color Doppler signals are increased after intravenous administration. Contrast material has been administered to a variety of sites, with the largest experience in the renal and liver circulations. Studies of both the main renal arteries (Fig 1) and intrarenal waveforms have shown improved imaging performance and faster examinations because of intravenous administration of

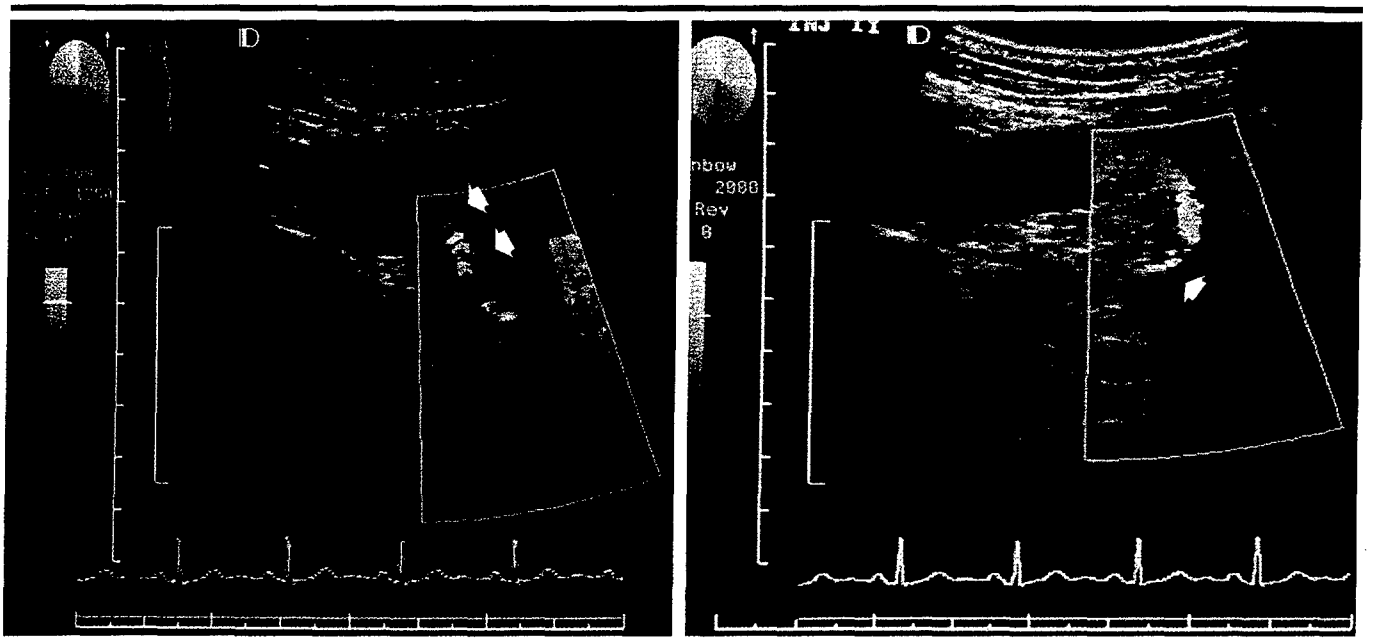

a. b.

Figure 1. Normal renal artery (angiographically proved) initially misinterpreted at US as renal artery stenosis. **(a)** Baseline Doppler image shows a portion of the renal artery (arrows). Spectral Doppler image initially showed increased velocity since the vessel was assumed to be straight and an incorrect spectral Doppler angle was assigned (not shown). **(b)** Contrast material–enhanced Doppler image shows a longer length of the renal artery and shows that the vessel actually has a tortuous course (arrow). The Doppler angle was then correctly assigned, and no elevated velocity was found.

contrast material. US examination in difficult liver cases such as slow flow in portal veins in patients with cirrhosis and in complete interrogation of transjugular intrahepatic portosystemic shunts has also been shown to be more accurate after administration of contrast material. More complete transcranial Doppler signals can be obtained after administration of contrast material. Contrast material cannot make a signal appear where the area of interest is completely obscured by bowel gas, but it can improve a partial signal that may be present. If contrast material can improve confidence in a negative examination or prove there is a pseudoocclusion, confirmatory, often more expensive testing can be eliminated. Gray-scale enhancement also is possible with some agents (Fig 2).

US studies with use of contrast agents initially will be used in selected cases in which US information is incomplete or difficult to obtain. This may be applied to individual patients or to all who will undergo a technically demanding study, such as renal artery or transcranial Doppler studies. Absence of nephrotoxicity may help make it an attractive alternative to iodinated contrast material in certain other patients. Wider adoption of US contrast agents will depend on whether they can improve accuracy or efficiency in more routine cases. Studies of accuracy, patient outcomes, and costs, with larger numbers of patients, will further clarify the role of these contrast agents.

For contrast agents to be widely adopted in radiologic practice, several obstacles must be overcome. US is perceived to be completely noninvasive. This changes with an intravenous injection, but the invasiveness may be acceptable if the test is more accurate, the cost is modest, and the administration is not burdensome. Even with an added cost, contrast agents may be effective if they can eliminate the negative consequences of inadequate or inaccurate US or obviate the use of alternative, more expensive, and sometimes riskier tests.

Further uses of microbubble US agents are actively being investigated. Agents with specialized applications, such as organ- or disease-seeking materials, are being evaluated. Some agents are removed by the reticuloendothelial system and can enhance normal liver but not tumors, which lack these cells. It is hoped that this will improve the sensitivity of hepatic US. Agents that attach to pathologic tissues are also being developed. For instance, some agents have been shown to attach to thrombi. This approach may have therapeutic implications. Microbubbles of a disease-seeking agent can contain gas and a chemotherapeutic agent. After the bubble attaches to the abnormality, a higher energy ultrasound beam can break the bubble and release the medicine locally for a potentially greater response than with traditional administration. US equipment also is being changed to use contrast material more effectively. One promising approach is harmonic imaging. Since bubbles resonate nonlinearly, they emit harmonic frequencies, in which case the instrument receives echoes at a different frequency than is transmitted. Contrast effects may be seen better or for a longer time with use of harmonic rather than fundamental frequencies. Other properties of bubbles are being investigated to exploit their unique properties. Bubbles behave differently at different pressures, which may allow noninvasive determination of blood pressure. It can thus be seen that microbubble agents have a vast potential role in improving US imaging.

Intraoperative and Endoscopic Applications

US has been keeping pace with the radical changes in surgery and continued growth of endoscopic procedures. Intraoperative US is an established accurate tool for surgical decision making. US imaging using specially designed laparoscopic US probes is another effective tool for providing important information. Laparoscopy

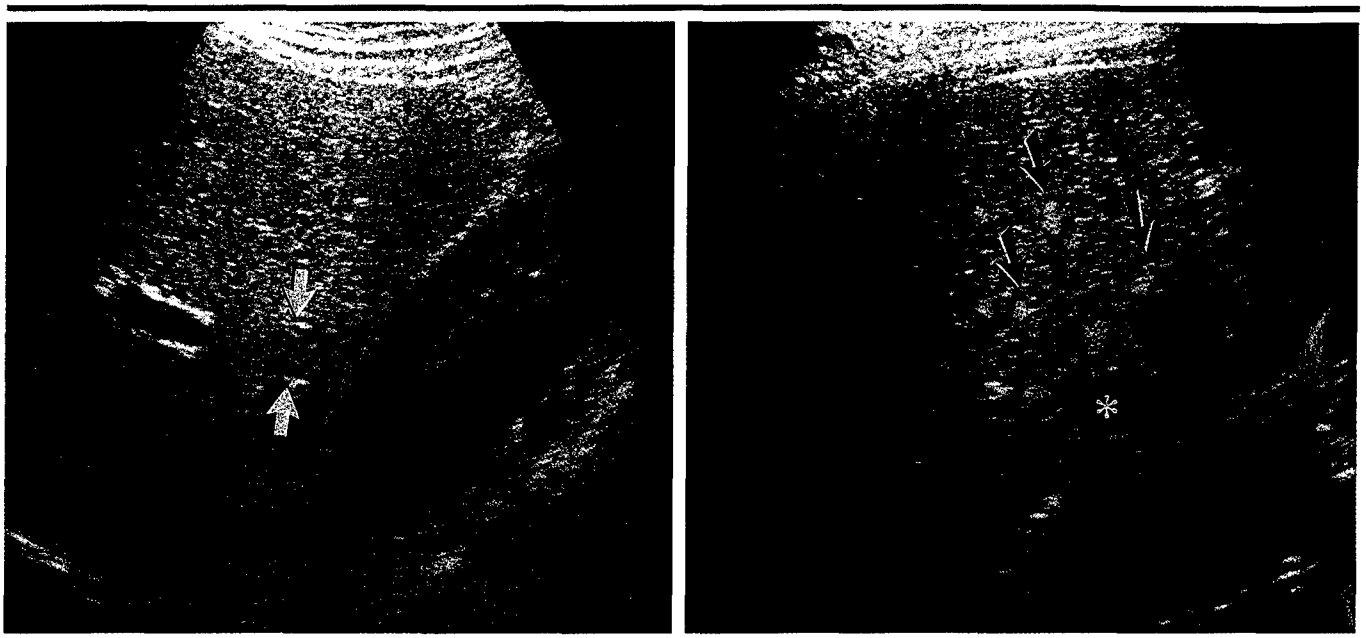

a. b.

Figure 2. Liver metastasis. (a) Baseline US image shows a nearly isoechoic liver lesion (arrows) that is difficult to distinguish from adjacent normal liver. (b) After intravenous administration of contrast material, there is gray-scale enhancement of the liver, and the lesion stands out as hypoechoic (*) against the more echogenic liver. The blood has markedly increased echogenicity, and the portal veins are markedly echogenic (arrows). Some portal veins shadow from the amount of contrast agent within them.

can eliminate needless surgery and can decrease the need for hospitalization. Cryoablation can now be performed laparoscopically in some patients. Endoscopic US is another growing technique that can help to stage gastrointestinal tumors and guide biopsies and other interventions. Smaller laparoscopic and more flexible endoscopic designs will allow these procedures to become even easier and more routine. The role of miniature transducers, initially designed for intravascular US, is being expanded to image many structures such as the ureter, esophagus, and anal canal. Design changes will allow better imaging through these tiny probes as well. The surgeon and endoscopist need an imaging test to show them what is below the surface and to guide therapy. Radiologists should be prepared to be part of the team providing diagnostic US during these procedures or be left behind as this revolution sweeps across medicine.

Three-dimensional US

Three-dimensional US is a new, exciting technology that allows physicians to use US to view anatomy and pathologic conditions as a volume, thereby enhancing comprehension of patient anatomy (9–11). Ongoing developments in computers and technology now permit acquisition, analysis, and display of volume data in seconds, facilitating many opportunities for rapid diagnosis and interventional techniques. Both commercial and academic interest in three-dimensional US is mounting, and continued advancements and understanding are expected in the near future.

Thus far, three-dimensional US has demonstrated several advantages compared with two-dimensional US. First, volume data can be viewed by using a standard anatomic orientation with planar images to obtain simultaneous display of coronal, sagittal, and axial planes in addition to orientations that are difficult or impossible to obtain with conventional two-dimensional US due to anatomic constraints (eg, coronal plane of the uterus). Second, rendering of the entire volume allows the continuity of curved structures such as liver vessels, the fetal spine, or fetal face to be viewed in a single image. Additionally, by rotating the volume interactively, it is possible to view the structure from multiple orientations or perspectives that enhance understanding of patient anatomy. Third, more accurate measurement of organ volume and irregularly shaped objects may be readily obtained (12). Fourth, volume data may be used to guide interventional procedures providing accurate identification of needle or catheter placement. Fifth, volume data may be archived and subsequently reviewed for further critical review or teaching purposes on site or via the Internet after the patient has left the clinic.

Ongoing clinical research is evaluating clinical applications likely to have the greatest effect on diagnosis and patient care. To date, fetal (13,14), cardiac (15–17), and gynecologic (18) areas have received the most attention with other clinical areas receiving increasing interest, including imaging of vascular anatomy, prostate volume measurement and assessment of seed placement, guidance of interventional needles and catheters, neonatal head evaluation, and evaluation of breast mass vascularity (19). In the fetus, improved visualization of fetal features, including the face (Fig 3), spine, and limbs, has improved identification of anomalies and has been immediately appealing for clearly sharing developmental information with the family and colleagues. Cardiac applications have provided a "surgeon's-eye view" with use of transesophageal and transthoracic techniques to assess valve geometry and motion and plan operative procedures.

Gynecologic applications include evaluating congenital anomalies of the uterus, endometrial cancer, adnexal masses, intrauterine device position, and follicular cysts. Applications in other specialties

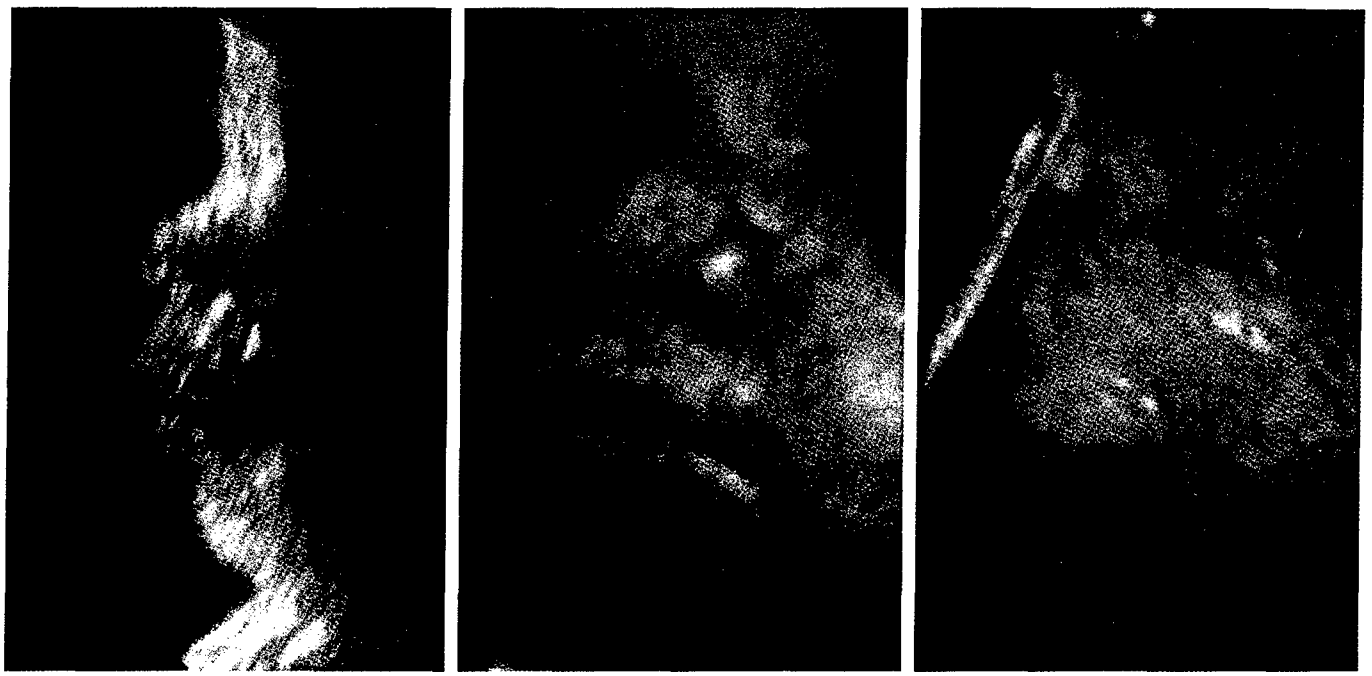

a. b. c.

Figure 3. (a) Sagittal section through a three-dimensional US volume data set of a 35-week-old fetus is similar to a conventional two-dimensional US image of the facial profile. (b) Rendered view of the face from the same volume provides a more recognizable picture of the face. (c) Rendered view of another 35-week-old fetus with cleft lip/palate and hypotelorism. The rendered images clearly demonstrate both normal and abnormal anatomy in a readily comprehended fashion.

such as urology, gastroenterology, dermatology, and ophthalmology are expanding the range of applications for three-dimensional US methods.

Coming soon will be further developments that will broaden the adoption of three-dimensional US imaging worldwide, including (*a*) improved overall scanning system performance and smaller scanners and transducers, (*b*) improved user interfaces making it easier to evaluate volume data and understand patient anatomy, (*c*) physiologic gating with both the cardiac and respiratory cycles eliminating motion artifacts and opening a window to dynamic processes, (*d*) combination of volume imaging and US contrast agents to enhance visualization of vascular anatomy (Fig 4), (*e*) faster volume acquisition, analysis, and interactive displays, ultimately leading to (*f*) real-time volume imaging in the near future.

Ultimately, three-dimensional US technology will provide a central integrating focus in US imaging. Three-dimensional US equipment will provide more conventional two-dimensional US imaging capability but seamlessly expand imaging to include volume acquisition and display as necessary to obtain the diagnosis. Focused application of three-dimensional US methods will expand the areas in which US is the predominant imaging modality beyond those areas in which US currently is the method of choice. Through rapid transmission of volume data to specialists at distant locations, patient care will benefit from improved diagnosis and treatment.

Aisotropic Imaging

Anisotropy, directional dependency, of the amplitude of a backscattered wave is a well-known property of US (20–24). Tissues in which backscatter anisotropy has been recognized include the renal cortex, myocardium, cerebral periventricular areas, and, most prominently, muscles and tendons. Anisotropy has mostly been a curiosity whose clinical importance rested only in recognizing its existence and accounting for its effects on images. It has never seriously been employed as a method of diagnosis or enhancement of echo contrast. Yet, the effects of anisotropy on backscatter can be huge, with angle-dependent backscattered differences having been measured that can vary by orders of magnitude (25,26). One could employ these very large dynamic ranges in differentiating normal anisotropic tissue from isotropic abnormalities such as tendon tears or in measuring surface-roughening effects of diseases as in osteoarthritis. Preliminary studies have shown remarkable angle-dependent sensitivities for backscattered ultrasound. Roughnesses as small as 5 μm (root-mean squared), easily small enough to detect the earliest structural changes in osteoarthritis, can be detected even with the use of standard diagnostic frequency (5-MHz) transducers (26,27). Even though cartilage surface may be difficult to visualize in vivo, it and other areas of demonstrable anisotropy such as myocardium, renal cortex, and tendons are waiting to be exploited.

Perfusion Imaging

An ultimate goal of vascular imaging is blood flow perfusion. In US, perfusion-like estimates (pixel counting) using spectral or color Doppler abound in the literature, but actual estimates of true perfusion are rare. Perfusion represents the volume of blood per mass of tissue (fractional blood volume) divided by the mean transit time of the blood through the tissue. Recent developments in blood flow quantitation appear to make such true perfusion estimates tractable. New techniques for estimating mean transit time include Doppler-based techniques (28), speckle

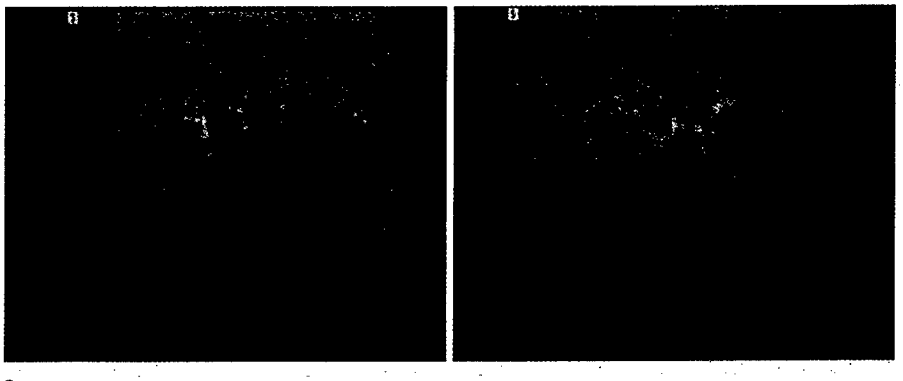

a.

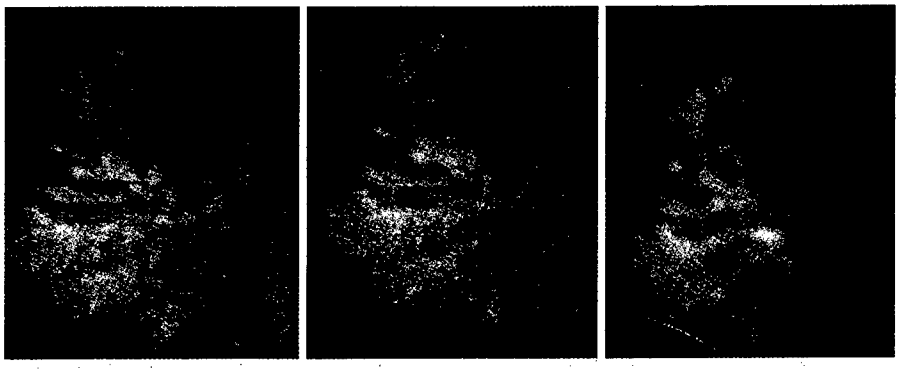

b.

Figure 4. Three-dimensional US study of a canine kidney after administration of a contrast agent (Imagent; Alliance Pharmaceutical, San Diego, Calif) and wide-band harmonic imaging (Siemens, Erlangen, Germany). **(a)** Two-dimensional US images of the kidney obtained during data acquisition. **(b)** Three volume-rendered images of the kidney from different projections. The continuity of the renal vasculature is clearly visible. Three-dimensional US combined with harmonic imaging and contrast agents provides superior spatial and temporal resolution compared with those of conventional Doppler imaging methods for the evaluation of vascular anatomy.

decorrelation techniques (29), both of which can be done with or without contrast agents, and methods requiring US contrast agents (30–32). US bubble contrast agents have particular advantages in this regard since they are totally intravascular, can exploit harmonic imaging to remove soft-tissue flash artifact (33), and can be manipulated externally by the ultrasound beam to actually alter the bubble distribution in vivo (30–32). In fact, extremely short boluses have been generated by using strongly focused exogenous ultrasound sources without injection of contrast material (34). Such manipulations can potentially remove the previously confounding effects of separating bolus shape from the tissue response making mean transit time estimates tractable. Finally, fractional blood volume estimates can now be made either with use of power Doppler with or without contrast agents or gray-scale imaging with contrast agents (35,36). Early imaging with these techniques has produced perfusion images in vivo that portend a whole new class of US-based diagnostic capabilities.

Co-registration of Sequential Images

Co-registration of US data sets from examinations at different times offers the exciting possibility of much more consistent and sensitive detection of changes in tissues between studies and better image quality. This could open new possibilities for screening and assessment of growth of suspicious regions or of masses during treatment. The three-dimensional image registration software, MiamiFuse (University of Michigan, Ann Arbor), was originally developed for fusion of data sets from multiple modalities (37). Its initial application to US images (38) has required very little preprocessing or specific image features, as the software is based on a statistical maximization of a measure aptly referred to as mutual information. The technique appears to work even in the presence of substantial tissue shear, warping, and limited overlap of scan regions.

There are other reasons why US examinations might benefit from registration of several image sets or examinations. For example, images from different transducer positions are partially uncorrelated, and summing them, in compound scanning, can improve the contrast-to-(speckle) noise ratio (39). Also, multiple viewing directions may depict and better represent flow than can a single view. This technique of co-registration by mutual information might be combined with beam reformation (40,41) for aberration correction to realize the high detail resolution of large apertures. Co-registration of images might also be combined with image-based location of images (42) in a freehand, three-dimensional scan to provide improved image quality and spatial fidelity. This is particularly appealing in the presence of respiratory motion during slow scanning required for sensitive three-dimensional imaging of vascularity.

Limitations on Image Improvement by Safety Considerations

In 1992, the U.S. Food and Drug Administration increased the limiting-guideline spatial-peak, time–average intensity levels for all applications to the levels previously allowed only for peripheral vascular studies (43). For general and obstetric examinations, these intensities were allowed to increase by a factor of almost 8. Since that time, the clear improvement in frame rate and quality of color flow images and of multiple-focal-zone gray-scale images has been made possible largely, and at little increased system cost, by the change in allowed output. The U.S. Food and Drug Administration acted (*a*) because professional organizations cooperated with industry to provide users with an indication of the relative output in the most biophysically relevant terms available—the thermal index, TI, and the mechanical index, MI (44); and (*b*) on the assumption that users would pay attention to those convenient indicators on the displays of systems capable of exceeding the former allowable output levels.

These indices are the best, usually conservative, estimates currently available in real time of the possible peak temperature rise (TI) and $p/f^{½}$ (the peak negative pressure divided by the square root of the frequency, or MI). When users increase their awareness of these indicators and employ them in mental risk-benefit analyses whenever the levels are high, it will be less likely that serious damage will occur. It would also be possible then that the limiting guidelines would be raised or

removed to allow additional, relatively low-cost improvements in diagnostic information for specific examination conditions in which unusual performance is seriously needed or actual risk is lower than would be assumed from the simplest interpretation of the displayed indices.

The threshold temperature rise for teratogenicity in animals is still assumed to be near 1.5°C (45), while TI_B, the TI calculated for bone surfaces, at the maximum outputs on current systems is as high as 10. Regarding nonthermal effects, small areas of hemorrhage have been observed at tissue-air boundaries in animals (lungs and intestines), and hemolysis has been observed with bubble contrast agents in mice (46) and in whole human blood in vitro (47). With the lowest available diagnostic frequencies, around 2 MHz, the in vivo effects have occurred at $p/f^{1/2}$ near the maximum allowed and employed MI value of 1.9. There are no known adverse nonthermal effects in vivo from US exposures in which the in situ value of $p/f^{1/2}$ is less than 0.5 MPa · $MHz^{-0.5}$. For reasons too extensive to list here, these large ratios of maximum employed values to bioeffects thresholds are possible without known effects in humans. The most important include the generally conservative design of the TI and MI calculations and probable rarity of use of maximum outputs and long, continuous exposure to key tissues in the most sensitive situations. However, there are situations in which the TI and MI are probably underestimates of the exposures and tests for effects have not been exhaustive. For the highest practical US performance and safety, there is no substitute for informed decisions by the user.

Other Areas of Development

There are several other areas of current development and future promise. These include harmonic imaging, elastography, image fusion, telesonography, virtual examination, and therapeutic US.

Harmonic imaging, mentioned previously in this article, was initially applied with contrast agents to increase the contrast between the blood and agent combination in a vessel and the surrounding tissue. However, it has been observed that second harmonic echoes, emanating from soft tissues from well-known nonlinear processes, can be imaged successfully. Recent experience has shown that, at least in some cases currently described as "the difficult patient," second harmonic imaging can improve the result. The images appear to be freer from artifactual components, and structural visualization is improved. The mechanisms for the improvement are not fully understood, but the technique could be expected to discriminate against multiple-scattering reverberations that are generated before the focus and thus at lower, more linear pressure amplitudes. The same applies to low-amplitude side lobes and general clutter lateral to the main lobe of the beam. The extent to which this approach will be applicable in diagnosis is also not known. However, it appears that there will be a role for this technique in imaging improvement, at least in some situations.

Elastography is a method for imaging the elastic or hardness properties of tissues (48). It is an imaging analogy to a physical examination searching for lumps by touch. With use of cross-correlation techniques to determine differences in motion of adjacent tissues that have different compressibilities, echo data are compared before and after a slight compression with the transducer. The differences in mechanical properties of adjacent tissues can be imaged in a conventional two-dimensional, cross-sectional, gray-scale manner. This method provides a new way of imaging the mechanical properties of tissues and holds promise for imaging differences between normal and abnormal tissues in situations where conventional gray-scale US does not.

Image fusion seeks to combine images from the same modality (as discussed above) and also from different modalities (37). These combinations may provide diagnostic information of greater confidence and/or convenience enhancing the value of the individual modalities involved.

As with other imaging modalities, US information transfer between scanning and interpretation sites will allow for more timely and efficient usage of facilities. Image transfer is being accomplished with dedicated lines, phone lines, and the Internet. If image acquisition becomes automated (possibly with increased feasibility of three-dimensional image acquisition with two-dimensional transducer arrays) it may even become possible for "home scanning" by the patient with communication of the information electronically to the interpreting physician. This "virtual examination" is the most speculative suggestion in this article, but it is an intriguing possible future direction for US.

Although the primary medical uses of US are in diagnosis, the future promises an increased role for US in intervention and therapy. In addition to the current use of US for biopsy guidance, US is a promising method for the guidance of gene therapy in solid organs. Ultrasound energy is also being investigated as a potential method for activation or release of therapeutic agents in target tissues, taking advantage of mechanical forces to release pharmaceuticals. Highly focused ultrasound beams are capable of delivering large amounts of thermal energy to small targets within the body with no damage to intervening structures. High-intensity focused ultrasound is capable of highly localized tissue destruction by means of thermal coagulation. High-intensity focused ultrasound tumor destruction in the prostate and liver may lead to relatively noninvasive percutaneous methods for definitive or palliative treatment of primary and metastatic tumors.

Conclusion

It is clear that US will remain a dynamic imaging technology in the foreseeable future, with expanded opportunities for improving patient care in a noninvasive and cost-effective fashion. At present, it appears that only a fraction of the potential of US for diagnosis and therapy has been realized. Support for basic and applied research is critical for this potential to be fully realized. Organizations such as the American Institute of Ultrasound and the Society of Radiologists in Ultrasound have been increasingly involved in recent years in identifying and encouraging research initiatives in US. Because of the opportunity this research provides for practical and useful clinical effect, federal and other sources of funding should be provided to facilitate the needed research.

Exciting progress in US technology has tended to place emphasis on the performance of the scanning equipment rather than the user. It is, however, essential to recognize the fact that the skill and experience of the sonographer or physician performing the examination and the physician supervising the examination and interpreting the images, regardless of the equipment used, ultimately determine the benefit of US in patient care. To realize the promise of research and new technology, and to transfer the capability of new instrumentation, contrast agents, and image processing to radiologists practicing US, the greatest challenge will be to provide effective education and training. It is in this role that the American Institute of Ultrasound in Medicine and the Society

of Radiologists in Ultrasound have a great opportunity to contribute to the success of translating the research of today into effective clinical practice of tomorrow.

References

1. Liu JB, Goldberg BB. Endoluminal ultrasound: vascular and nonvascular applications. London, England: Dunitz, 1998.
2. Feld R, Liu JB, Nazarian LN, et al. Laparoscopic liver sonography: preliminary experience in liver metastases compared with CT portography. J Ultrasound Med 1996; 15:289–295.
3. Needleman L, Forsberg F. Contrast agents in ultrasound. Ultrasound Q 1996; 13:121–138.
4. Cosgrove D. Ultrasound contrast enhancement of tumours. Clin Radiol 1996; 51(suppl):44–49.
5. Otis S, Rush M, Boyajian R. Contrast-enhanced transcranial imaging: results of an American phase-two study. Stroke 1995; 26:203–209.
6. Tachibana K, Tachibana S. Albumin microbubble echo-contrast material as an enhancer for ultrasound accelerated thrombolysis. Circulation 1995; 92:1148–1150.
7. Fritzsch T, Schlief R. Future prospects for echo-enhancing agents. Clin Radiol 1996; 51(suppl):56–58.
8. Melany ML, Grant EG, Duerinckx AJ, Watts TM, Levine BS. Ability of a phase shift US contrast agent to improve imaging of the main renal arteries. Radiology 1997; 205:147–152.
9. Fenster A, Downey DB. Three-dimensional ultrasound imaging: a review. IEEE Eng Med Biol Mag 1996; 15:41–51.
10. Nelson TR, Pretorius DH. Interactive acquisition, analysis, and visualization of sonographic volume data. Int J Imaging Sys Technol 1997; 8:26–37.
11. Pretorius DH, Nelson TR. Three-dimensional ultrasound. Ultrasound Obstet Gynecol 1995; 5:219–221.
12. Riccabona M, Nelson TR, Pretorius DH, Davidson TE. Three-dimensional sonographic measurement of bladder volume. J Ultrasound Med 1996; 15:627–632.
13. Merz E, Weber G, Bahlmann F, et al. Application of transvaginal and abdominal three-dimensional ultrasound for the detection or exclusion of malformations of the fetal face. Ultrasound Obstet Gynecol 1997; 9:237–243.
14. Pretorius DH, Nelson TR. Fetal face visualization using three-dimensional ultrasonography. J Ultrasound Med 1995; 14: 349–356.
15. Greenleaf JF, Belohlavek M, Gerber TC, Foley DA, Seward JB. Multidimensional visualization in echocardiography: an introduction. Mayo Clin Proc 1993; 68:213–219.
16. Belohlavek M, Foley DA, Gerber TC, et al. Three- and four-dimensional cardiovascular ultrasound imaging: a new era for echocardiography. Mayo Clin Proc 1993; 68:221–240.
17. Nelson TR, Pretorius DH, Sklansky M, Hagen-Ansert S. Three-dimensional echocardiographic evaluation of fetal heart anatomy and function: acquisition, analysis, and display. J Ultrasound Med 1996; 15:1–9.
18. Jurkovic D, Geipel A, Gruboeck K, et al. Three-dimensional ultrasound for the assessment of uterine anatomy and detection of congenital anomalies: a comparison with hysterosalpingography and two-dimensional sonography. Ultrasound Obstet Gynecol 1995; 5:233–237.
19. Carson PL, Moskalik AP, Govil A, et al. The 3D and 2D color flow display of breast masses. Ultrasound Med Biol 1997; 23:837–849.
20. Insana MF, Hall TJ, Fishback JL. Identifying acoustic scattering sources in normal renal parenchyma from the anisotropy in acoustic properties. Ultrasound Med Biol 1991; 17:613–626.
21. Insana MF. Modeling acoustic backscatter from kidney microstructure using an anisotropic correlation function. J Acoust Soc Am 1995; 97:649–655.
22. Miller JG, Perez JE, Mottley JC, et al. Myocardial tissue characterization: an approach based on quantitative backscatter and attenuation. Proc IEEE Ultrason Symp 1983; 1947:782–793.
23. Bowerman RA, DiPietro MA. Erroneous sonographic identification of lateral ventricles: relationship to the echogenic periventricular "blush." Am J Neuroradiol 1987; 8:661–667.
24. Rubin JM, Carson PL, Meyer CR. Anisotropic ultrasonic backscatter from the renal cortex. Ultrasound Med Biol 1988; 14:507–511.
25. Hoffmeister BK, Wong AK, Verdonk ED, Wickline SA, Miller JG. Comparison of the anisotropy of apparent integrated ultrasonic backscatter from fixed human tendon and fixed human myocardium. J Acoust Soc Am 1995; 97:1307–1313.
26. Chiang EH, Laing TJ, Meyer CR, Boes JL, Rubin JM, Adler RS. Ultrasonic characterization of in vitro osteoarthritis articular cartilage with validation by confocal microscopy. Ultrasound Med Biol 1997; 23: 205–213.
27. Adler RS, Dedrick DK, Laing TJ, et al. Quantitative assessment of cartilage surface roughness in osteoarthritis using high-frequency ultrasound. Ultrasound Med Biol 1992; 18:51–58.
28. Dymling SO, Persson HW, Hertz CH. Measurement of blood perfusion in tissue using Doppler ultrasound. Ultrasound Med Biol 1991; 17:433–444.
29. Adler RS, Rubin JM, Fowlkes JB, Carson PL, Pallister JE. Ultrasonic estimation of tissue perfusion: a stochastic approach. Ultrasound Med Biol 1995; 21:493–500.
30. Fowlkes JB, Sirkin DW, Rhee R, Rubin JM, Carson PL. In vivo interruption of contrast agents for temporally short arterial bolus production. J Ultrasound Med 1997; 16:S36.
31. Matsumura T, Moriyasu F, Nada T, et al. Efficacy of continuous infusion and flash echo mode on contrast-enhanced power Doppler imaging of the liver (abstr). Radiology 1997; 205(P):279.
32. Kamiyama N, Mine Y, Kono Y, Goto Y, Shiki E, Moriyasu F. Dual window method of harmonic imaging and flash echo imaging associated with an US contrast agent (abstr). Radiology 1997; 205(P):279.
33. Burns PN, Powers JE, Hope-Simpson D, Uhlendorf V, Fritzsch T. Power Doppler imaging combined with contrast-enhancing harmonic Doppler: new method for small-vessel imaging (abstr). Radiology 1994; 193(P):366.
34. Ivey JA, Gardner EA, Fowlkes JB, Rubin JM, Carson PL. Acoustic generation of intra-arterial contrast boluses. Ultrasound Med Biol 1995; 1:757–767.
35. Rubin JM, Adler RS, Fowlkes JB, et al. Fractional moving blood volume: estimation with power Doppler US. Radiology 1995; 197:183–190.
36. Rubin JM, Bude RO, Fowlkes JB, Spratt RS, Carson PL, Adler RS. Normalizing fractional moving blood volume estimates with power Doppler US: defining a stable intravascular point with the cumulative power distribution function. Radiology 1997; 20:757–765.
37. Meyer CR, Boes JL, Kim B, Bland PH, et al. Demonstration of accuracy and clinical versatility of mutual information for automatic multimodality image fusion using affine and thin plate spline warped geometric deformations. Med Image Anal 1997; 1:195–206.
38. LeCarpentier GL, Moskalik AP, Meyer CR, et al. Breast and prostate 3D color flow ultrasound quantification and image fusion (abstr). Radiology 1997; 205(P):740.
39. Moskalik A, Carson PL, Meyer CR, et al. Registration of three-dimensional compound ultrasound scans of the breast for refraction and motion correction. Ultrasound Med Biol 1995; 21:769–778.
40. Mast TD, Nachman AI, Waag, RC. Focusing and imaging using eigenfunctions of the scattering operator. J Acoust Soc Am 1997; 102:715–725.
41. rishnan S, Li PC, O'Donnell M. Adaptive compensation of phase and magnitude aberrations. IEEE Trans Ultrasonics Fer Freq Control 1996; 43:44–55.
42. Chen JF, Fowlkes JB, Carson PL, Rubin JM. Determination of scan-plane motion using speckle decorrelation: theoretical consideration and initial test. Int J Imaging Sys Technol 1997; 8:38–44.
43. Food and Drug Administration. 510(k) guide for measuring and reporting output of diagnostic ultrasound medical devices. Rockville, Md: Center for Devices and Radiological Health, 1992.
44. American Institute of Ultrasound in Medicine and National Electrical Manufacturer's Association. Standard for real-time display of thermal and mechanical acoustic output indices on diagnostic ultrasound equipment (revision 1). Laurel, Md: American Institute of Ultrasound in Medicine and National Electrical Manufacturer's Association, 1998.
45. Edwards MJ. Hyperthermia as a teratogen: a review of experimental studies and their clinical significance. Teratog Carcinog Mutagen 1986; 6:563–582.
46. Dalecki D, Child SZ, Raeman CH, et al. Age dependence of ultrasonically induced lung hemorrhage in mice. Ultrasound Med Biol 1997; 23:767–776.
47. Brayman AA, Strickler PL, Luan H, et al. Hemolysis of 40% hematocrit, Albunex®-supplemented human erythrocytes by pulsed ultrasound: frequency, acoustic pressure and pulse length dependence. Ultrasound Med Biol 1997; 23:1237–1250.
48. Ophir J, Cespedes I, Garra B, et al. Elastography: ultrasonic imaging of tissue strain and elastic modulus in vivo. Eur J Ultrasound 1996; 3:49–70.

A HAND-CONTROLLED, 3D ULTRASOUND GUIDE AND MEASUREMENT SYSTEM

Ralph C. Fenn, J. Brian Fowlkes, Aaron P. Moskalik
Yong Zhang, Marilyn A. Roubidoux, Paul L. Carson

Department of Radiology
University of Michigan Medical Center
Ann Arbor, Michigan 48109-0553

INTRODUCTION

Summary

Three dimensional (3D) ultrasound images provide superior visualization of anatomical features than two dimensional (2D) power mode or frequency shift color Doppler B-scan ultrasound images. However, 3D data sets require transducer position measurements that can be problematic. One previously investigated approach completely automates transducer positioning and measurements with one dimensional motorized stages. Other system types permit full six degree-of-freedom (DOF) manual transducer manipulation while measuring all six axes. In contrast this work explores the middle ground of measuring the two degrees of freedom most important for free-hand scanning while fixing the remaining axes for minimized complexity.

The device designed, fabricated, and tested allows linear motion perpendicular to the scan plane and along the beam axis, as well as rotation about an axis parallel to the array. The measurement system is designed to minimize size, weight, and cost while maximizing accuracy and ease of operator use. The resulting design weighs 500g in its heaviest configuration and is 150 mm long, 64 mm high, and 70 mm wide. It is capable of 0.1 mm accuracy in the focal plane. Three dimensional data with continually varying translational and rotary speeds was interpolated in 3D by image processing software to minimize distortion in standard Cartesian coordinates. Phantom images show little distortion due to the measuring system or data processing algorithm. This inexpensive, compact, and lightweight system interferes minimally with clinician free-hand scanning and enhances 3D image collection and generation capabilities in the clinical setting.

Three Dimensional Data Acquisition

The goal of three dimensional ultrasound imaging has been pursued by a number of research laboratories. Conventional 2D ultrasound images are inherently limited in their ability to display 3D human anatomy and their diagnostic usefulness is thus reduced. A number of laboratories have investigated various methods of attaining the critical transducer position measurements to create 3D data sets. A common feature of many of these imaging systems is

Acoustical Imaging, Vol. 23
Edited by Lees and Ferrari, Plenum Press, New York, 1997

computer controlled, motor-driven linear ultrasound transducer motion (Pretorius et al., 1992, Picot et al., 1993, Moskalik et al., 1995, Tong et al., 1996, and Hernandez et al., 1996). These designs give precise control of the ultrasound transducer position, usually with one degree-of-freedom. However these motorized systems frustrate the clinician's desire for the flexibility of conventional hand-controlled ultrasound examinations. Free-hand control facilitates localizing a specific region of interest (ROI), especially when examining organs of convex or concave external shape such as the shoulder, the uterus, and the liver near the ribs.

In contrast, other studies have provided complete freedom of motion for manual examinations while measuring the positions of each of the 6 axes of motion, both translation and rotation (Detmer et al., 1994, Kelly et al., 1994, Nelson and Pretorius, 1995, and Hughes et al., 1996). Such systems are often less accurate and may be complex, large, and more costly. The approach of the present work uses an intermediate approach with manual transducer control only in the degrees-of-freedom that are most helpful, while avoiding complete 6 DOF freedom of motion that increases complexity and cost. The current design measures 2 DOF and can be easily retrofitted for measurement of the third axis, which is a second translation axis.

METHODS

Instrumentation System Overview

The 3D ultrasound data acquisition system is comprised of three major parts. First is the ultrasound imaging system. The scanning data presented was gathered by a General Electric Logiq 700 MR machine with a 739L transducer but the design is equally applicable to other machine types. Second is the personal computer which handles data acquisition and storage. The current experiments collect position data at the same fixed, 4 Hz rate as the production of ultrasound B-scan images. In future experiments, the personal computer will store B-scans at desired spatial increments through signals to the cardiac gating feature of the ultrasound machine. For color flow studies of maximum sensitivity, cardiac signals will trigger ultrasound image storage and simultaneous position measurements by the personal computer. The third major component, and the focus here, is the mechanical transducer guiding system and its translation and rotation sensors. Postprocessing for 3D image construction is performed on a Digital Equipment Corporation Alpha workstation.

System Design of the Guide and Measurement System

The overall goal of allowing natural, free-hand transducer motion in 2 DOF while measuring translation and rotation drove the design of the measurement system. This goal requires a compact device that allows natural grasp of the transducer grip. The device must not provide too much friction or require movement of significant mass. It should provide range of motion greater than required for screening examinations. The device must have low overall mass to maximize patient comfort. The accuracy and linearity must be high so that these factors contribute little additional distortion to the 3D image. Finally it should be inexpensive. These factors all influenced the design described below.

Figure 1 shows the design developed by this program that provides transducer guidance and measurement. The design uses a "series" design where multiple DOF are created by selecting a base motion type and installing the other DOF on the now moving base stage. In the device described here the base stage provides translation. This is advantageous because of the large stroke required. The alternative of mounting the translation stage on the rotary axis would be very clumsy because of the large radius of the resulting rotating mass. For this reason the rotation stage is mounted on the translation carriage. Finally a second translation stage is mounted on the rotating shaft to provide the third DOF. The first two DOF are measured however the third is not but could be instrumented using straightforward methods. This third DOF can be locked, or left free when positional accuracy is not critical, e.g. while following rough surface contours.

The major components shown in Figure 1 are described below beginning with those components nearest the patient. At the base is a stabilizing platform made of acrylic sheet with a window for transducer array access to the skin. The material is clear for ease of positioning, has low thermal conductivity for patient comfort, and is easily cleanable.

Mounted horizontally on the base plate is a Thompson Series 10 miniature linear

UNIVERSITY OF MICHIGAN LIBRARIES

bearing. This bearing provides motion of the transducer in the z axis which is defined to be perpendicular to the long dimension of the ultrasound array (x axis).

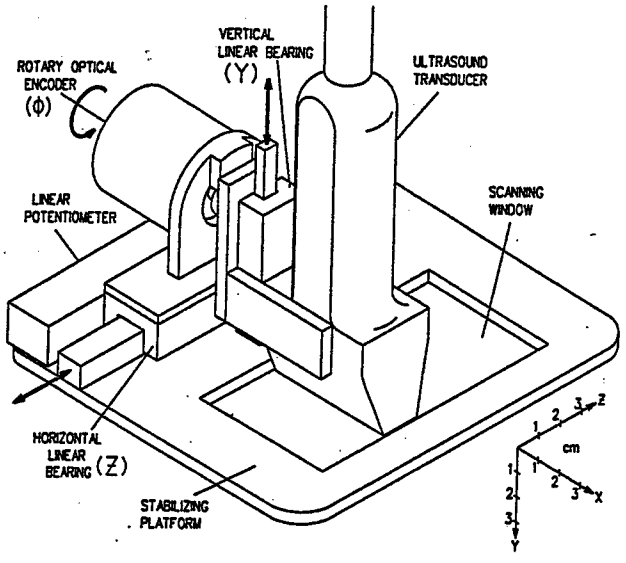

Figure 1. The ultrasound transducer guide and measurement system (drawing by Ben Moskalik).

Low friction is provided by the light rather than heavy preload on the bearings, and by the use of low friction bearing seals. Preload is required to minimize backlash, particularly in the roll axis. Waterproof grease such as petroleum jelly excludes gel and cleaning water from the bearing interior while being nontoxic to the patient.

Parallel to the linear bearing and also mounted on the base plate is a precision linear potentiometer. This off-the-shelf Duncan Electronics 400 Series potentiometer uses a high linearity conductive plastic film and has dual, parallel wipers to reduce noise. This potentiometer measures the translation of the ultrasound array by providing a voltage output when a reference voltage is applied to the resistive element. The friction and damping of the wiper is adjustable by removal of plastic inserts. The wiper access slot has rubber seals that face the side to avoid gel and water intrusion. This sensor has the advantage of providing an analog output which simplifies development of interfaces to various laboratory instruments during system development and experiments. Minimal distortion of the interpolated three dimension model of the tissues requires low position noise and high accuracy. These important potentiometer parameters were measured with results presented at the end of this section.

The capacity to rotate the transducer array around an axis parallel to the array (x axis) is provided by a rotary optical encoder mounted onto the linear bearing carriage. This optical encoder integrates the functions of a rotary bearing and rotary sensor. If separate components were used instead and connected by a belt, for example, backlash and calibration errors would be much larger. The RIS15 encoder from BEI Encoder Systems Division is used and has 2,000 lines on the disk, thus supplying 8,000 counts per turn using quadrature electronics. This disk resolution supplies angle precision of 0.045 degrees or linear precision of 0.075 mm at 50 mm below the skin. The internal encoder bearings provide 22N (5 lbf) load capability which is sufficient to support the transducer and normal operator hand forces. An analog output is provided for simplicity of interface thus avoiding software intensive serial communication.

A major goal of this effort is miniaturization of the measurement system. The resulting design weighs 650g including the ultrasound transducer. This mass is divided into stationary parts weighing 190 g, which includes the base plate, potentiometer, and linear bearing rail. The moving parts weigh 460 g which includes a typical 140 g ultrasound transducer, an optical encoder weighing 170 g, a vertical linear bearing weighing 30 g, and various brackets.

The length of the package along the translation (z) axis is 153 mm, and the width (x

axis) is 142 mm parallel to the transducer array. The height (y axis) without a ultrasound transducer installed is 64 mm to the top of the optical encoder body. The device fits into a rectangular prism of 1400 cc. In the configuration illustrated the translational range is 70 mm which is easily expandable.

Translation Sensor Linearity and Noise Measurements

Poor linearity and contact noise are traditional weaknesses of potentiometers. The potentiometer was selected for the final design because of the advantages of size and weight over competing linear optical encoders, but only after complete testing of linearity and noise.

Linearity was measured by translating the potentiometer wiper with a lead screw and measuring the potentiometer wiper voltage with a constant voltage applied to the resistive element. The voltage was read by a 12 bit analog-to-digital-converter (ADC) board that was also used for the phantom and clinical data presented in the Results Section. This experimental protocol tests the linearity of the ADC as well as the potentiometer. The error of the digital position measurement was calculated from the best linear model of the data using a least mean square algorithm. The worst cumulative error is 0.47 mm or 0.68 percent. By avoiding the first 2 mm of the 69 mm stroke the nonlinear error can be limited to 0.35 percent. It is important to note that the maximum nonlinear error between successive 0.5 mm slices is limited to 0.16 mm or 32 percent of the slice spacing. This implies that the greatest distortion using this potentiometer would be one third of a space between scan planes. Further improvement in linearity is available in high linearity (0.1%) potentiometers available from the manufacturer.

The electrical noise of the translational sensing system was also measured during a typical slew maneuver of 1 mm per second. Resistance changes as the wipers slid across the conductive film were determined as well as noise from the cabling and ADC circuitry. Figure 2 shows the calculated position during slewing. The primary feature of the plot is the series of steps due to the quantization size of the 12 bit ADC circuit. The resistor output voltage is 10 V for a 100 mm range. This is processed by a 12 bit ADC having 4096 steps and an input range which is also 10 V. The result is quantization steps of 2.4 mV, or 0.024 mm, for the stated position and voltage ranges. Figure 2 shows that this quantization noise dominates the calculated transducer position. Potentiometer noise is small relative to the ADC quantization error and is insignificant for this application.

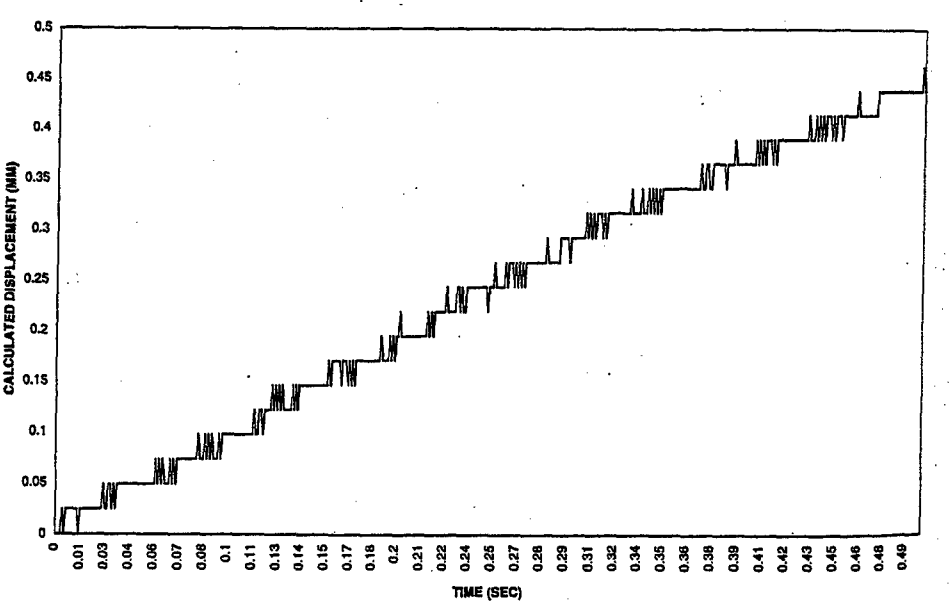

Figure 2. Electrical noise during slewing of the plastic film linear sensor.

UNIVERSITY OF MICHIGAN LIBRARIES

RESULTS

The goal of the program is construction of a measurement system that provides linear and rotary position of the ultrasound transducer. The ultimate goal for this data is the construction of 3D data sets where any 2D image section can be presented to the viewer without significant distortion. Real-time measurements avoid the need for evenly spaced B-scans because the 3D image processing software can accomodate the varying slice spacing. Trilinear interpolation is used to assign weighted fractions of the raw image data into the desired 3 D grid. A raw 3D data set was created from scans of a filament phantom. A single B-scan was used as a reference image and a similar section of the interpolated 3D data was evaluated for distortion.

The first step in this evaluation was creation of a reference 2D B-scan image of the phantom. The B-scan was taken perpendicular to the phantom filaments for finest detail and minimal sensitivity to precise transducer alignment. This 2D image is shown in Figure 3.

A 3D data set was created from a set of B-scans taken *parallel* to the phantom filaments, i.e.. perpendicular to the reference 2D scan. Motion was allowed in both translation and

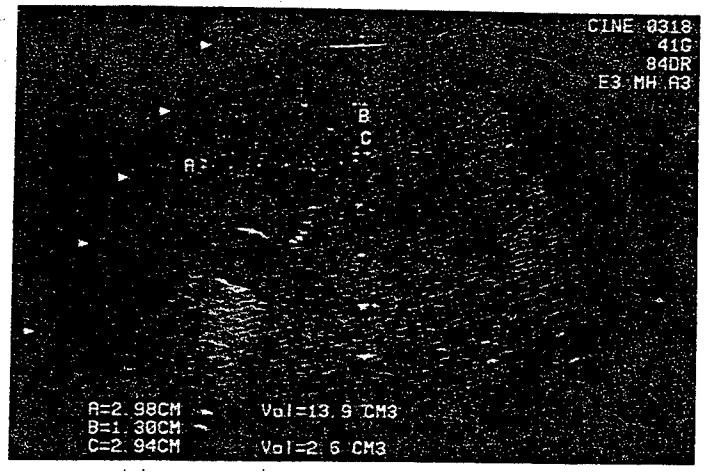

Figure 3. Reference B-scan perpendicular to the phantom filaments.

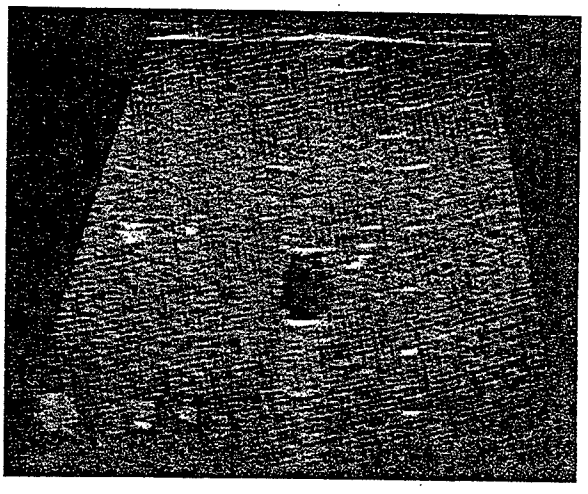

Figure 4. An image from the 3D data set after interpolation for rotation and uneven spacing.

rotation. Figure 4 shows an image reconstructed from the 3D data set after interpolation based on the measurement system. Data from each scan plane was placed into the nearest Cartesian-grid vertices using trilinear interpolation. The figure shows how the features from Figure 3 are presented with an acceptable level of distortion. Note that the lateral boundaries the image are not parallel and thus accurately reflect the degree of rotation employed during the 3D data collection.

Figure 4 shows some degradation in image quality due to reduced resolution. This effect results from the different precision of beam focusing between the in-plane and out-of-plane directions. Electronic focusing within the B-scan plane provides better focusing, and also high depth of field through changes in focus depth. In the elevational, or out-of-plane direction used by the 3D software to reconstruct objects perpendicular to the constituent B-scans, single array elements provide poorer focusing. The resulting 3D image is smeared in the translation direction because of the large elevational beam width. The 3D image shown is provides the most severe conditions for comparison of B-scan and 3D data.

CONCLUSIONS

This work has developed a small, low cost ultrasound transducer position measuring system that minimally affects the clinician's preferred technique during ultrasound examinations. Manual examination is facilitated by permitting varying speeds of translation while still producing low distortion 3D image sets. Patient comfort is maximized by the device's light weight while its small size permits access to a range of body regions comparable to the ultrasound transducer alone. Measurement of the two axes critical to image acquisition flexibility is provided while motion in other axes is prohibited, thus simplifying measurement, data acquisition, and image processing.

ACKNOWLEDGMENTS

General Electric Medical Systems and Corporate Research Laboratory were particularly helpful with development of rapid acquisition and transfer of digital image data. This work was supported in part by PHS grant R01 CA55076 from the National Cancer Institute and contract No. DAMD 17-96-C-6061 from the Army Medical Research and Development Command.

REFERENCES

Detmer, P.R., Bashein, G., Hodges, T., Beach, K.W., Filer, E.P., Burns, D.H., and Strandness, D.E., 1994, 3D ultrasonic image feature localization based on magnetic scanhead tracking: In vitro calibration and validation, *Ultrasound Med. and Bio.* 20:923.

Hernandez, A., Basset, O., Dautraix, I., and Magnin, I., 1996, Acquisition and stereoscopic visualization of three-dimensional ultrasonic breast data, *IEEE Trans. Ultrasonics,Ferro. and Freq. Ctl.* 43:576.

Hughes, S.W., D'Arcy, T.J., Maxwell, D.J., Chiu, W., Milner, A., Saunders, J.E., and Sheppard, R.J., 1996, Volume estimation from multiplanar 2D ultrasound images using a remote electromagnetic position and orientation sensor, *Ultrasound in Medicine.* 22:561.

Kelly, I.A.G., Gardener, J.E., Brett, A.D., Richards, R., and Lees, W.R., 1994, Three dimensional US of the fetus, *Radiology* 192:253.

Moskalik, P.L., Carson, P.L., Meyer, C.R., Fowlkes, J.B., Rubin, J.M., and Roubidoux, M.A., 1995, Registration of three-dimensional compound ultrasound scans of the breast for refraction and motion correction, *Ultrasound in Med. And Biol.* 21:769.

Nelson, T.R. and Pretorius, D.H., 1995, Visualization of the fetal thoracic skeleton with three-dimensional sonography, *AJR.* 164:1485.

Picot, P.A., Rickey, D.W., Mitchell, R., Rankin, R., and Fenster, A., 1993, Three dimensional colour doppler imaging, *Ultrasound in Med. and Bio.* 19:95.

Pretorius, D.H., Nelson, T.R., and Jaffe, J.S., 1992, 3-dimensional sonographic analysis based on color flow doppler and gray scale image data, *Ultrasound Med.* 11:225.

UNIVERSITY OF MICHIGAN LIBRARIES

Utility of 3D Ultrasound in the Discrimination and Detection of Breast Cancer

Gerald L. LeCarpentier, Ph.D., Pamela B. Tridandapani, M.S., J. Brian Fowlkes, Ph.D., Marilyn A. Roubidoux, M.D., Aaron P. Moskalik, M.S., Paul L. Carson, Ph.D.

Department of Radiology
University of Michigan Medical Center
Ann Arbor, MI, USA

Correspondence:
Gerald L. LeCarpentier, Ph.D.
University of Michigan Medical Center
Department of Radiology
Kresge III Room 3315
200 Zina Pitcher Place
Ann Arbor, MI 48109-0553
Vox: (734) 647-9326
Fax: (734) 764-8541

Acknowledgement: This work was supported in part by PHS Grant # R01CA53076 from the National Cancer Institute and by the U.S. Army Medical and Material Command under DAMD17-96-C-6061.

Table of Contents

- Abstract
- Introduction
- Data Acquisition and Processing
  - Image Acquisition
  - Scanning Apparatus
  - Post-Acquisition
  - Regions of Interest
- Examples of Volume Renderings
  - 3D Rendering of Infiltrating Ductal Carcinoma
  - Various 2D Reconstructions
- Clinical Discrimination Results
  - Speed Weighted Pixel Density
  - Comparison With Gray Scale
- Conclusions

Utility of 3D Ultrasound in the Discrimination and Detection of Breast Cancer

Gerald L. LeCarpentier, Ph.D., Pamela B. Tridandapani, M.S., J. Brian Fowlkes, Ph.D.,
Marilyn A. Roubidoux, M.D., Aaron P. Moskalik, M.S., Paul L. Carson, Ph.D.

Abstract

The purpose of this article is to demonstrate evaluation techniques of 3D ultrasound imaging and their growing utility in the discrimination and assessment of breast cancer. Our ongoing studies include women with mammographically observed breast masses scheduled for biopsy. During ultrasound imaging of suspicious breast lesions, transducer position is encoded for each power mode and frequency shift color Doppler image (p-CDI and f-CDI) as well as each standard B-mode image, typically 90 images in each mode. Vessels are then displayed as reconstructed color volumes in 3D, superimposed on gray scale slices. Radiologists identify suspicious masses and rate their appearance for conventional gray scale and new vascular criteria. In an initial patient population, ultrasound discrimination of malignant masses in 3D volumes demonstated superiority over its 2D counterpart. In the related patient group presented in this article, one particular vascularity measure, **S**peed **W**eighted Pixel **D**ensity (SWD), shows statistically different ($p<0.001$) values for benign ($n=13$) versus malignant ($n=15$) cases. Given our modest success in discriminating breast cancer in an initial patient pool with other vascularity measures, results of this second patient population continue to suggest vascularity as a potential cancer discriminator.

[Previous: Title Page] [Next: Introduction]

[Title Page | **Abstract** | Introduction | Data Acquisition and Processing]
[Examples of Volume Renderings | Clinical Discrimination Results | Conclusions | References]

Utility of 3D Ultrasound in the Discrimination and Detection of Breast Cancer

Gerald L. LeCarpentier, Ph.D., Pamela B. Tridandapani, M.S., J. Brian Fowlkes, Ph.D.,
Marilyn A. Roubidoux, M.D., Aaron P. Moskalik, M.S., Paul L. Carson, Ph.D.

Introduction

Subjective assessment of ultrasound Doppler imaging may be enhanced by more quantitative analyses. Displaying vascularity in 3D is relatively simple, as the image segmentation is performed by the color flow imaging system, and sparse vascular patterns are easily appreciated in 3D. A number of investigators (**1-4**) have done a good job of semiquantitative evaluation of color flow image characteristics of the breast; however, it may be difficult to objectively sample the sparse breast vasculature throughout the tumor volume in totally free hand 2-D sampling. Stavros, et al. have achieved very promising results in the evaluation of breast cancer using a multivariable gray-scale assessment of 2D imaging (**5,6**). Cosgrove and Lees also indicated that the addition of color flow Doppler to B-mode improved the diagnostic accuracy by an amount approximately equal to the benefit of adding ultrasound to mammography. They quote that the chance of malignancy after workup must be <2% to consistently avoid biopsy (**7**).

Based on the potential benefits of combining 3D sampling and quantitative assessments, a preliminary study was performed to evaluate which Doppler signals might provide discrimination of breast cancer from benign masses and to compare 2D and 3D ultrasound display modes. The amount of blood flowing as indicated by power mode color Doppler imaging (p-CDI) (**8**) and velocity indicated by mean frequency color Doppler imaging (f-CDI) both lend themselves to quantitative measures (**9**). To evaluate information provided in these measures and to aid visual assessment, we undertook a visual and digital analysis of information in a study including 3D ultrasound examinations of 20 breast patients scheduled for breast biopsy and have subsequently analyzed examinations on 28 patients obtained with a different scanner. 3D breast lesion image volume acquisition techniques and visualization schemes are presented here in general, and a particular vascularity measure (Speed Weighted Pixel Density) measured in each of 4 regions of interest in and around the mass is compared to standard gray scale criteria for this current patient pool.

[Previous: Abstract] [Next: Data Acquisition and Processing]

[Title Page | Abstract | **Introduction** | Data Acquisition and Processing]
[Examples of Volume Renderings | Clinical Discrimination Results | Conclusions | References]

Data Acquisition and Processing

In an early study, quantitative measures were calculated for 20 different subjects (10). Nine masses were malignant, four were fibroadenomas, and seven were other benign masses. Each exam consisted of one or more power mode 3D scans and a frequency shift 3D scan of the mass and the surrounding tissue. The 3D scans in these clinical trials analyzed were acquired using the system described in (9) . This system consisted of a conventional ultrasound scanner (Spectra VST, Diasonics, Inc., Milpitas, CA), a modified mammography unit which applied mild compression to stabilize the breast and a motorized transducer positioner mounted to the mammography unit. At the 6 MHz Doppler frequency of our 6-10 MHz linear array, signals produced in the two color flow modes were measured to quantitatively estimate vascularity features in various 3D regions of interest (ROIs) in and around the suspicious masses. Click here to see an early example of a dynamic display technique we employed (11). Observers in the earlier study judged the 3D displays to be superior to recorded 2D images, particularly for assessment of amount and morphology of vascularity (11). Based on these prior experiences, we continued 3D ultrasound scanning with the modifications noted below.

Image Acquisition

The examples shown in subsequent sections were obtained with a new hand held scanner (12) and a 7.5 MHz linear or 12 MHz array scanhead (Logiq 700, GE Medical Systems, Milwaukee, WI). Acquisition of 3D ultrasound volumes is achieved with a step size between scan planes typically 0.5 mm for the 50-120 images per scan, covering a volume typically 35 x 45 x 45 mm^3. Power mode images (p-CDI) are set to maximize sensitivity to small vessel flow, while frequency shift (f-CDI) settings are a compromise between slow flow detectability and aliasing. Each Doppler image acquired is software triggered externally by a cardiac gated computer interface, which also records transducer position and provides operator scan speed feedback.

The Scanning Apparatus

The hand-controlled transducer fixture device is designed to provide guided trajectory of the transducer while measuring the two spatial variables, linear position and rotation angle as shown in **Figure 1**. Mounted on the base platform is a miniature linear bearing which enables motion of transducer in the x-axis, perpendicular to the ultrasound array. Behind the linear bearing and also mounted onto the base plate is a precision linear potentiometer. The translation of the transducer linearly changes the resistance of the potentiometer, ultimately providing an output potential to our computer interface proportional to scan head position. Resolution of the linear encoder is dictated by A/D quantization, in this case corresponding to a distance of 18 microns. A light weight rotary optical encoder provides angular measurement, via a quadurature decoder (designed and built in-house) and software interface, providing an angular resolution of 0.04 degrees. A window in the base plate allows scan head contact with the patient.

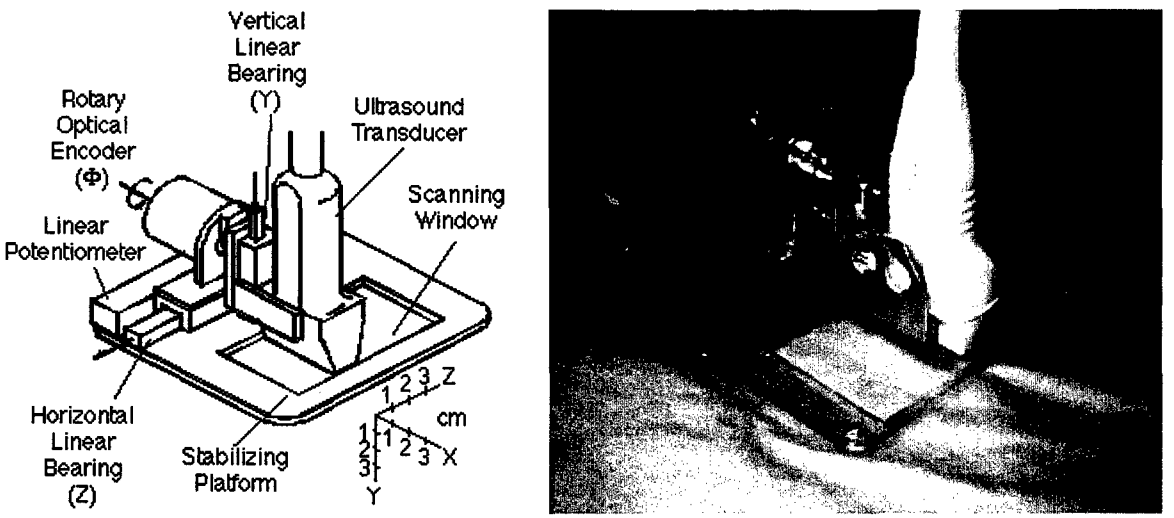

Figure 1. (a) Schematic representation of the hand scan apparatus. (b) The actual mechanism.

Post-Acquisition

Data is transferred from the GE ultrasound scanner to a DEC Alpha workstation, where individual slice planes are cropped and "stacked" together to form a 3D volume. From the 3D image volume set, vessels from ultrasound scans are displayed as color volumes in 3D, superimposed on gray scale slices, for the identification of suspicious masses. Our visualization software and related processing modules facilitate 3D viewing. Presently, the clinician is able to position, tilt, scale and adjust all axes of a

"dynamic" ellipsoid which is selected based on the gray scale borders of the suspicious mass. This radiologist defined ellipsoid (RDE) serves as the point of reference for all other regions of interest, as described below. Most of the other regions of interest are actually defined by the clinician's selection. For the quantitative analysis of vascularity, the methods described in (9,10) are employed. Quantities such as those described in (9,10) are presented in **Table 1** and are calculated for each of the four regions of interest (ROIs) defined in **Table 2**. Also, visual gray scale features are evaluated on a 5 point scale, averaged, and used for comparison with vascularity.

PD	Power Weighted Pixel Density	$PD = \sum_{i=1}^{N_b} P_i / N_t$
NMPCP	Normalized Mean Power In Colored Pixels	$NMPCP = \sum_{i=1}^{N_b} \frac{P_i}{P_b} / N_b$
NPD	Normalized Power Weighted Pixel Density	$NPD = \sum_{i=1}^{N_b} \frac{P_i}{P_b} / N_t$
SWD	Speed Weighted Pixel Density	$SWD = \sum_{i=1}^{N_b} V_i / N_t$
$\overline{V}$	Mean Speed in Colored Pixels	$\overline{V} = \sum_{i=1}^{N_b} V_i / N_b$
SNPD	Speed and Power Weighted Normalized Pixel Density	$SNPD = \sum_{i=1}^{N_b} \frac{V_i \cdot P_i}{P_b} / N_t$

Table 1. Ultrasound vascularity measures and their formulas. Nb is the number of pixels with flow in them and Nt is the total pixels in the region of interest. Pi is the power Doppler value of the ith pixel and Vi is the Doppler speed value of the ith pixel. This measurement of speed is calculated from the mean frequency shift value assuming an isotropic distribution of vessels, because no directional information is obtained. Pb is the estimated power value in 100% blood at the depth of the ith pixel.

1. Lesion: normally from the outer gray scale border up to 1 cm inside.
2. Lesion, proximal side only: (hemi-ellipsoidal version of region 1).
3. External periphery: mass gray scale boundary up to 1 mm outside.
4. External periphery, proximal side only: (hemi-ellipsoidal version of region 3).
Table 2. List of the four 3D regions of interest (ROIs) associated with the mass and used in the quantitative analysis of vascularity.

[Previous: Introduction] [Next: Examples of Volume Renderings]

[Title Page | Abstract | Introduction | **Data Acquisition and Processing**]
[Examples of Volume Renderings | Clinical Discrimination Results | Conclusions | References]

Clinical Trials and Vascularity Measures

Analysis of Clinical Results

Scatter plots of NPDmax and [(vm)(NPDmax)] vs. Average Visual Gray Scale Rating (1=normal to 5=highly suspicious) were evaluated for each subject in the previous study (**10**). All the points for malignant masses formed a cluster with higher values of quantitative vascular measures and gray scale rating as hypothesized. Discriminant analysis on cancer versus all benign masses provided a classification with sensitivities of 100% and specificities of 82% and 90%, for NPDmax and [(v m)(NPDmax)], respectively, when combined with gray scale ratings. These specificities were higher than for gray scale rating alone, but the statistical uncertainty in these numbers is large. Our second patient pool is aimed at adding greater statistical significance to these values and explore possible other quantitative measures. **Figure 4** demonstrates one such measure, Speed Weighted Pixel Density (SWD as described in **Table 2**). It is mathematically equivalent to pixel density times the average velocity, and thus similar to [(v m)(NPDmax)] without the power weighting. SWDmax refers to the the maximum or peak SWD value calculated in the 4 regions described in **Table 1**. As shown in the figure, the mean value of log(SWDmax) is significantly different for the benign versus malignant groupings ($p<0.001$ that the means are equal).

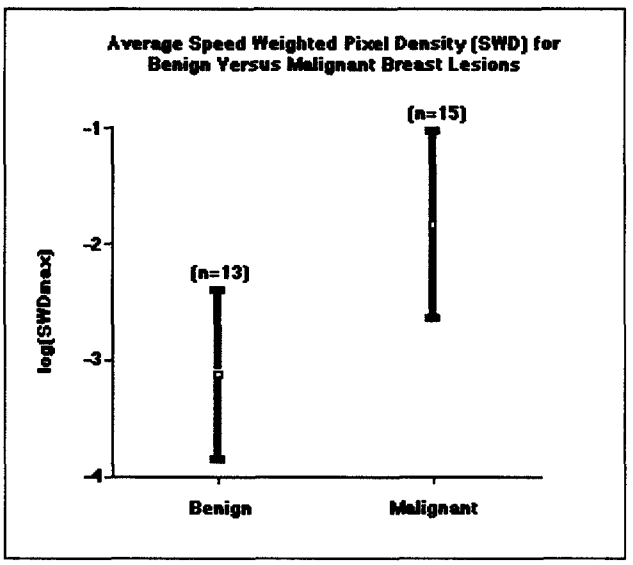

Figure 4. Plot of the mean peak log(SWD) for benign versus malignant breast lesions. The probability that the means of these sub-groups are different showed statistical significance ($p>0.999$).

Comparative Results

ROC analysis was performed on the SWD measure and average gray scale rating using ROCKIT software provided by the University of Chicago Department of Radiology (from the current versions of an ROC software package developed by Professor Charles Metz and his colleagues). **Figure 5** demonstrates the predictive similarity between the SWD measure and the average gray scale rating (GS). The graph on the left shows the raw data and ROC curve fit for both measures. On the right, the 95% confindence intervals for these measures, give a subject pool of 28 patients. The Az values calculated for SWD and GS were comparable, 0.88 and 0.84, respectively.

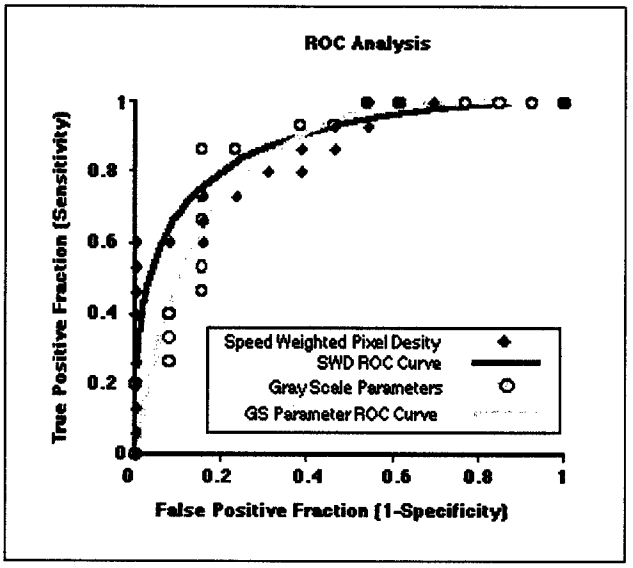

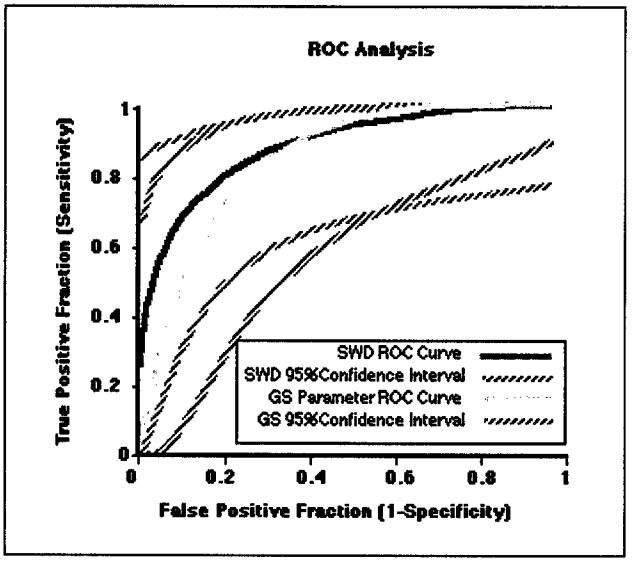

Figure 5. (Top) Calculated true positive fractions (TPF) versus false positive fractions (FPF) of log(SWDmax) and average gray scale ratings (GS) for our 28 patient population. Overlayed are smooth calculated ROC curves. (Bottom) Calculated ROC curves with their respective 95% confidence intervals for the same measures as on the left.

[Previous: Examples of Volume Renderings] [Next: Conclusions]

[Title Page | Abstract | Introduction | Data Acquisition and Processing]
[Examples of Volume Renderings | **Clinical Discrimination Results** | Conclusions | References]

Conclusions

Our data transfer, processing, and visualization tools have been developed to the point where full 3D volumes and vascularity isosurface mappings can be reviewed within an hour of the ultrasound exam itself. These developments have facilitated the visualization of vascular morphology as well as an ease in scanning through entire ultrasound volume sets from different perspectives. In addition, we have provided the radiologist with a straightforward method for defining reproducible ROI ellipsoids within a given ultrasound volume which facilitates a variety of quantitative measures. As demonstrated by ROC analyses, these objective measures of vascularity (most recently SWD) in and of themselves have been shown to be as effective as subjective gray scale measures for our current patient population.

Given these observations, we believe that vascularity should improve the discrimination of benign and malignant solid masses by ultrasound and that the results are probably generalizable to different scanners. Larger numbers of subjects and improved ease of performance of good vascularity exams are now needed to allow good judgements of the achievable diagnostic accuracy and cost effectiveness of adding vascularity to clinical ultrasound assessments of breast masses. Ease of performance is well on its way, with advances occurring rapidly in 3D scanning, image analysis and display. If p-CDI data (e.g. NPDmax) and f-CDI measures (e.g. SWDmax) each, separately, continue to perform comparable to gray scale measures and almost as well as the power and color flow mode combination required for log[(Vm)*(NPDmax)] as demonstrated in our earlier report (**9**), then one of the two color flow 3D scans can be eliminated to speed the entire process. Alternatively, the ultrasound system manufacturer could supply the p-CDI and f-CDI signals simultaneously with sufficient signal dynamic range for accurate assessments of the perfusion-like log[(Vm)*(NPDmax)] on a pixel by pixel basis. For imaging vessel patterns, little would be lost by requiring the same system settings for both f-CDI and p-CDI modes in a single image.

The possible utility of vascularity measures is strengthened by the success (**Figures 4** and **5**) of the f-CDI measure SWD in discriminating malignant from benign masses with the most recent data from the GE M12, 8-11 MHz, 1.5D matrix array. SWD was not the most successful measure in the original Diasonics data, but possible utility was shown with SWD. If that trend observed in the matrix array data continues, there may not be a need to perform the more difficult, multiregion, NPDmax and log[(Vm)*(NPDmax)] examinations and measurements.

Gray scale readings were performed by a radiologist, highly experienced in breast imaging and ultrasound. If vascularity measures on simple regions of interest can perform at least as well as gray scale with the experienced reader, then the potential for use of vascularity in improving routine diagnosis is high.

In summary, our modest success in discriminating breast cancer in an initial patient pool with other vascularity measures and the results of this second patient population continue to suggest vascularity as a potential cancer discriminator. Our visualization and quantization tools should continue to facilitate this process.

[Previous: Clinical Discrimination Results] [Next: References]

[Title Page | Abstract | Introduction | Data Acquisition and Processing]
[Examples of Volume Renderings | Clinical Discrimination Results | **Conclusions** | References]

References

1. Carson PL, Adler DD, Fowlkes JB, Harnist K, Rubin J (1992). *Enhanced Color Flow Imaging of Breast Cancer Vasculature: Continuous Wave Doppler and 3-D Display* , J. Ultras. Med., **11**, 377-385.

2. Bamber J, Eckersley R, Cosgrove D, Bell D, RP K (1993), *3-D Reconstruction of Combined Colour Doppler and Grey Scale Images of Breast Tumours, Breast Ultrasound Update* , Madjar H, Teubner J, Basel, Karger.

3. Cosgrove DO, Kedar RP, Bamber JC, al-Murrani B, Davey JB, Fisher C, McKinna JA, Svensson WE, Tohno E, Vagios E, et al. (1993). *Breast disease: color Doppler US in differential diagnosis.* Radiol. **189**: 99-104.

4. Cosgrove DO, Bamber JC, Davey JB, McKinna JA, Sinnett HD (1990), *Color Doppler signals from breast tumors, Work in progress,* Radiol. **176**, 175-180.

5. Stavros AT, Parker SH, Dennis MA, Johnson KK, Thickman DI, Rapp CL (1993), Radiol. (Procs, 79th RSNA) 189(P), 406.

6. Stavros AT, Thickman D, Rapp CL, Dennis MA, Parker SH, Sisney GA (1995), *Solid breast nodules: use of sonography to distinguish between benign and malignant lesions.* , Radiol **196**, 123-134.

7. Cosgrove DO, Lees WR (1994), Abdominal Ultrasound Workshop, Eurodop, European Doppler Ultrasound Symposium, Oxford.

8. Rubin JM, Adler RA, Fowlkes JB, et al. *Fractional moving blood volume: estimation with power Doppler US.* Radiology 1995; **197**:183-190.

9. Carson, P.L., Fowlkes, J.B., Roubidoux, M.A., Moskalik, A.P., Govil, A., Normolle, D. LeCarpentier, G., Nattakom, S., Rubin, J.M., *3D doppler image signal quantification of breast masses.* Ultrasound Med. Biol., 1998. **24**(6).

10. Carson, P.L., X. Li, J. Pallister, A. Moskalik, J.M. Rubin, and J.B. Fowlkes. *Approximate Quantification of Detected Fractional Blood Volume in the Breast by 3D Color Flow and Doppler Signal Amplitude Imaging.* in 1993 Ultrasonics Symposium proceedings. 1993. Piscataway: IEEE : p. 1023-1026.

11. Carson PL, Moskalik AP, Govil A, Roubidoux MA, Fowlkes JB, Normolle D, Adler DD, Rubin JM, Helvie M. *The 3D and 2D color flow display of breast masses.* Ultrasound Med. Biol. 1997; **23**:837-849.

12. Fenn, R.C., J.B. Fowlkes, A.P. Moskalik, Y. Zhang, M.A. Roubidoux, and P.L. Carson. *A hand- controlled, 3-D ultrasound guide and measurement system.* in Acoustical Imaging. 1997. New York: Plenum Press **23**, p. 237-242.

Read 10/29/2001

DEPARTMENT OF THE ARMY
US ARMY MEDICAL RESEARCH AND MATERIEL COMMAND AND FORT DETRICK
810 SCHRIEDER STREET, SUITE 218
FORT DETRICK, MARYLAND 21702-5000

REPLY TO
ATTENTION OF:

MCMR-RMI-S (70-1y) 17 Oct 01

MEMORANDUM FOR Administrator, Defense Technical Information Center (DTIC-OCA), 8725 John J. Kingman Road, Fort Belvoir, VA 22060-6218

SUBJECT: Request Change in Distribution Statement

1. The U.S. Army Medical Research and Materiel Command has reexamined the need for the limitation assigned to technical reports written for grants. Request the limited distribution statements for the Accession Document Numbers listed at enclosure be changed to "Approved for public release; distribution unlimited." These reports should be released to the National Technical Information Service.

2. Point of contact for this request is Ms. Judy Pawlus at DSN 343-7322 or by e-mail at judy.pawlus@det.amedd.army.mil.

FOR THE COMMANDER:

PHYLIS M. RINEHART
Deputy Chief of Staff for
Information Management

Enclosure